An Acoustic Modelling Study of Seismic Airgun Noise in Queen Charlotte Basin

by

Alexander Orion MacGillivray
B.Sc. University of Victoria 2000

A Thesis Submitted in Partial Fullfillment of the
Requirements for the Degree of

MASTER OF SCIENCE

in the School of Earth and Ocean Science

An Acoustic Modelling Study of Seismic Airgun Noise
in Queen Charlotte Basin

by

Alexander Orion MacGillivray
B.Sc. University of Victoria 2000

Supervisory Committee

Dr. N. Ross Chapman (School of Earth and Ocean Science)
Supervisor

Dr. Stan E. Dosso (School of Earth and Ocean Science)
Department Member

Dr. George D. Spence (School of Earth and Ocean Science)
Department Member

Dr. Svein Vagle (School of Earth and Ocean Science)
Department Member

Dr. Roberto G. Racca (JASCO Research Ltd.)
Additional Member

Supervisory Committee

Dr. N. Ross Chapman (School of Earth and Ocean Science)

Supervisor

Dr. Stan E. Dosso (School of Earth and Ocean Science)

Department Member

Dr. George D. Spence (School of Earth and Ocean Science)

Department Member

Dr. Svein Vagle (School of Earth and Ocean Science)

Department Member

Dr. Roberto G. Racca (JASCO Research Ltd.)

Additional Member

Abstract

This thesis presents a methodology for modelling underwater sound propagation from seismic airgun surveys. Subsequently, the method is applied to the case of predicting noise levels from offshore oil and gas exploration in the Queen Charlotte Basin region of the British Columbia offshore. Underwater noise levels are predicted using an integrated modelling approach that incorporates (i) an airgun array source model, (ii) a broadband 3-D transmission loss model, and (iii) environmental databases of high resolution bathymetry, historical CTD casts and geoacoustic properties of the seabed. As part of this thesis, an airgun array source signature model is developed and then used for predicting the acoustic source level of a seismic airgun array. The airgun model, based on the physics of the oscillation and radiation of airgun bubbles, is validated against real airgun data. Underwater sound propagation is modelled in three dimensions using a parabolic-equation (PE) based, "$N\times$2-D" transmission loss model. Broadband sound propagation is approximated by modelling acoustic transmission loss at third-octave band centre frequencies; noise levels are computed by subtracting transmission loss from the respective third-octave band airgun array source levels. High resolution bathymetry and geoacoustic data for Queen

Charlotte Basin are extracted along centrolineal radial transects for input to the propagation model. Additionally, principal component analysis is applied to a large collection of historical CTD data to extract seasonal sound speed profile variations. Transmission loss is modelled using both winter and summer sound speed profiles to bracket seasonal variations in acoustic propagation conditions. Noise level estimates from the acoustic modelling may be used to determine impact zones around the survey vessel where marine mammals are expected to exhibit disturbance reactions to airgun noise. Results from this study will aid in evaluating the potential environmental impacts of seismic exploration activity on marine ecosystems in British Columbia's offshore region.

Table of Contents

List of Tables

List of Figures

Acknowledgements

I would like to thank my graduate supervisor, Ross Chapman: the time I spent studying with you has been a great joy to me. Your guidance and encouragement were invaluable while we tackled the research challenges of this thesis project.

I would also like to extend my gratitude to my JASCO supervisors, Roberto Racca and David Hannay for the leadership, understanding, financial means and friendship you both gave me for the duration of my thesis work.

As well, I would like to thank my JASCO coworkers and my fellow students in the Ocean Acoustics laboratory for humour and friendship given to me during this time.

Special thanks go to Dr. Ron Smyth of the BC Offshore Oil and Gas Team for providing an impetus and partial funding for this thesis project.

Finally, I would like to acknowledge the support of my wife, Natalie: without your encouragement, your blackberry pies and your companionship, I would never have finished writing this thesis dissertation.

Chapter 1

Introduction

The scientific community in recent years has become increasingly interested in the effects of anthropogenic (*i.e.*, man-made) noise on marine mammals and fish. Particular attention has focused on marine seismic surveys with airgun arrays, which are among the loudest anthropogenic noise sources in the ocean (NRC, 2003, Tab. 2-1b). Despite the attention this subject has received, very little is currently known about the effects of seismic airgun noise on marine mammals and fish, and whether these effects are "biologically significant" (see, *e.g.*, NRC, 2004). Among the most basic questions that require answers are: "How loud is an airgun array?" and "What sound levels are generated by an airgun survey at location X?"

This thesis dissertation presents a general method for estimating the loudness (*i.e.*, the source level) of an airgun array and for modelling underwater sound levels generated by that array in a particular marine environment. The method developed in this thesis combines an airgun array source signature model with a broadband acoustic propagation model to estimate received sound levels in the vicinity of an airgun array. This method is applied to the problem of modelling underwater noise generated by a seismic airgun survey in the Queen Charlotte Basin, in the British Columbia offshore region.

1.1 Background: marine seismic airgun surveys

Modern marine seismic airgun surveys are capable of high-resolution three-dimensional imaging of the Earth's crust, down to tens of kilometres depth, and have thus become an es-

sential tool both for the oil and gas industry and for research scientists studying the Earth's structure and associated geological hazards (*e.g.*, earthquakes). Seismic airgun surveys may be divided into two types, 2-D and 3-D, according to the type of data that they acquire. 2-D surveys are so-called because they only provide a two-dimensional cross-sectional image of the earth structure and are characterized by large spacing between survey lines, on the order of a kilometre or more. 3-D surveys, on the other hand, employ denser line spacing, on the order of a few hundred metres, to provide a three-dimensional volumetric image of the earth structure.

A typical airgun survey, either 2-D or 3-D, is operated from a single survey ship that tows both the seismic source and receiver apparatus. The seismic source is an airgun array consisting of many individual airguns that are fired simultaneously in order to generate a seismic pulse. In some cases, large surveys will employ more than one airgun array in order to optimize the survey resolution; in this case the arrays will have nearly identical layouts and are fired in alternation. The detector apparatus for a seismic airgun survey consists of one or more streamer cables, several kilometres in length, that contain hundreds of sensitive hydrophones for detecting echoes of the seismic pulse reflected from sub-bottom features.

Airgun arrays are broadband acoustic sources that project energy over a wide range of frequencies, from under 10 Hz to over 5 kHz (Richardson et al., 1995, Fig. 6.20). However, airgun arrays are designed to produce most of their energy below 300 Hz at frequencies useful for seismic profiling (NRC, 2003, p. 60). The arrays consist of many airguns that are configured in such a way as to project the maximum amount of seismic energy vertically into the earth. However, much of the sound energy still leaks off to the sides of an array and into the surrounding environment; sound levels may be 10–20 dB less in the horizontal direction for a typical airgun array, depending on the number of guns.

The volumes and positioning of individual guns in an array are selected in such a way as to generate as clean a seismic pulse as possible — that is, sharply peaked with very little ringing in the vertical direction (Parkes and Hatton, 1986, p. 25). Since the configuration of airgun arrays can be quite variable, they are often described in terms of the number of guns and their total volume (*i.e.*, the sum of the volumes of the guns comprising the array). A typical airgun array for an oil and gas survey will consist of several tens of guns and have a a total volume of several thousand cubic inches; as a rule of thumb, the loudness of an array is generally proportional to the number of guns (NRC, 2003, p. 59).

Quoted (peak) source levels for airgun arrays are often as high as 260 dB re μPa at 1 m (Richardson et al., 1995, Tab. 6.6). However, this apparently high value for the source level can lead to erroneous conclusions about the impact on marine mammals and fish for the following reasons:

1. Peak source levels for seismic survey sources are quoted relative to the vertical direction; however, due to the intrinsic directivity of the radiated sound field, source levels off to the sides of the array are generally much lower.

2. Far field source levels do not apply in the near field of the array where the individual airguns do not add coherently; sound levels in the near field are, in fact, lower than would be expected from far field estimates.

The source level of a seismic airgun array varies considerably in both the horizontal and vertical directions, due to the complex configuration of guns comprising the array. Thus, one must account for this variability in order to correctly predict the sound field generated by an airgun array. In practice it is extremely difficult, and often impractical, to measure the source level of a large airgun array *in situ*. However, if the source signatures of the individual airguns are known, then it is possible to accurately compute the source level of an array by summing up the contributions of the array elements with the appropriate phase delays corresponding to their relative positions. This latter approach has been shown to be quite accurate for determining the source level of an airgun array (Ziolkowski et al., 1982).

1.2 Motivation: the Queen Charlotte Basin

In recent years there has been renewed interest in opening the British Columbia offshore region to oil and gas exploration and development. This interest comes in light of new scientific research indicating that there may be significant oil and gas deposits, larger than previously expected, in the sedimentary basins located off the coast of British Columbia. Particular attention has focused on the Queen Charlotte Basin where the largest oil and gas deposits are believed likely to be located (Hannigan et al., 2001). However, a recent expert panel report by the Royal Society of Canada has advised that many science gaps exist on the potential impact of hydrocarbon exploration and development in the British Columbia offshore region (RSC, 2004).

One consequence of opening the Queen Charlotte Basin to oil and gas exploration is that marine mammals and fish will be exposed to heightened levels of underwater noise, in particular from sporadic seismic airgun activity. The Queen Charlotte Basin is an important habitat for several threatened and endangered species of marine mammals and fish (RSC, 2004, Tab. 5.1). The potential effects of airgun noise on marine mammals and fish are both physiological and behavioural: within a few hundred metres of an array, airgun noise may induce a temporary shift in hearing threshold; at longer ranges airgun noise may displace individual animals or mask calls from conspecifics (Richardson et al., 1995, p. 325). A necessary first step in assessing the potential of seismic exploration impact on marine mammals and fish in Queen Charlotte Basin is to estimate the extent to which seismic oil and gas survey activities are likely to the ensonify the waters of this coastal region. It is expected that noise level predictions from this thesis dissertation will facilitate an accurate and objective assessment of the potential impacts of seismic survey noise on marine mammals and fish in the Queen Charlotte Basin.

1.3 Thesis outline

The following paragraphs provide an outline of the concepts developed and ideas presented in the subsequent chapters of this dissertation.

Chapter 2 develops a numerical model for the acoustic source signature of an array of airguns. This model is based on a physical simulation of the oscillation and radiation of a collection of airgun bubbles, as first described by Ziolkowski (1970). In addition to the basic bubble physics, the source model also accounts for non-linear pressure interactions between airguns, port throttling, and heat transfer across the bubble wall, as described by investigators such as Ziolkowski et al. (1982), Dragoset (1984), Landrø (1992) and Laws et al. (1990). The values of several free physical parameters in the model are constrained by matching the output of the model to measured airgun source signatures using a simulated annealing optimization algorithm. A method is also presented for computing the far-field source level of an airgun array so that it may be combined with transmission loss estimates from standard acoustic propagation models (*i.e.*, which solve the Helmholtz equation for a point-like sound source).

Chapter 3 provides an overview of the parabolic-equation (PE) based acoustic propaga-

tion model, RAM, which is used for modelling acoustic transmission loss (Collins, 1993). RAM is modified to incorporate the complex density fluid approximation of Zhang and Tindle (1995) in the sub-bottom to simulate propagation over an elastic seabed. The modified propagation model is benchmarked against an analytic reference solution for an elastic bottom waveguide to demonstrate the correct implementation of the approximation.

Chapter 4 presents the bathymetry, sound speed profile and geoacoustic data that are employed for modelling sound propagation in Queen Charlotte Basin. Representative sound speed profiles for winter and summer are derived from a principal component analysis of historical temperature/salinity data in the basin. As well, a geoacoustic map for the basin is developed based on published accounts of the bottom geology in Queen Charlotte Basin. Geoacoustic profiles for the different geological "provinces" are estimated based on the geoacoustic modelling methodology of Hamilton (1980).

Chapter 5 describes the setup and execution of the airgun noise model, including details of the seismic survey array configuration and also the nine source locations in Queen Charlotte Basin. Convergence testing of the numerical propagation model is discussed and the spatial resolution of the modelling grids is provided. Details of the third-octave band, $N\times$2-D modelling are summarized, showing how azimuthally varying source levels for the airgun array are combined with transmission loss from RAM to generate received sound level predictions.

Chapter 6 presents the results of the airgun array noise modelling in Queen Charlotte Basin. Received level contour maps for the entire basin are presented for all nine modelling locations for both winter and summer sound speed profiles. The noise level contours are analyzed to determine the area and mean radius for each noise level isopleth from 180 dB re μPa to 90 dB re μPa broadband level.

Chapter 7 discusses the results of the noise modelling in Queen Charlotte Basin, with regards to the effects of seismic noise on marine mammals as well as sources of error in the received level predictions. Finally, the conclusions of the noise modelling study are presented and the modelling methodology developed in this thesis dissertation is summarized.

Chapter 2

Airgun array source model

Predicting waterborne noise levels from a seismic airgun survey requires an accurate model for the acoustic signature of an airgun array. Currently, arrays of airguns are the most commonly used sources for marine geophysical surveying: airgun arrays are excellent seismic sources, since they produce sharply peaked seismic wavelets (in the vertical direction) with relatively weak secondary oscillations. However, the large, distributed nature of airgun arrays makes them particularly complex acoustic sources to model since the source level of an array varies considerably with direction from the source. Furthermore, the directionality of an airgun array is seldom measured *in situ* since arrays are very large and operate at low frequencies. Instead, the source signature of an airgun array is most often predicted from physical models of airgun radiation.

This chapter discusses the development of a realistic source signature model for an array of airguns, based on the physics of large bubble oscillations. In addition to the basic bubble physics, the model includes the effects of nonlinear pressure interactions between airguns, port throttling and heat transfer across the bubble wall. The final model, which contains four free parameters, is tuned to match real airgun signature data using simulated annealing optimization. The output of the model is a set of pressure signatures representing the contribution of individual guns to the far-field source signature of the array.

2.1 Airgun operation principles

An airgun is an underwater acoustic source that generates an acoustic pulse by the rapid release of very highly compressed air. A functional diagram of a typical airgun is shown in Figure 2.1; the airgun operates as follows:

1. Two hollow chambers, sealed by a piston and connected by a narrow tube, are charged with compressed air.

2. A magnetic solenoid, triggered by an electrical current, opens a valve which breaks the piston's pressure seal.

3. The resulting force differential moves the piston, releasing a bubble of compressed air through the gun ports.

4. The sudden release of compressed air results in a sharply peaked acoustic pulse, useful as a seismic source.

Several different designs of airguns are now in widespread use, including so-called "sleeve guns" in which the release mechanism is an outer sheath rather than a piston. However, the principles of operation remain essentially the same for all classes of airgun.

An example source signature for a single airgun is shown in Figure 2.2(a)[1]. Examining the figure, one can see that the sharp initial peak is followed by a series of long-period "bubble pulses" which repeat at regular intervals with steadily decaying amplitude. For the seismologist, the bubble pulses are an undesirable feature of the airgun signature, since they smear out reflections on a seismogram. It is difficult to eliminate the bubble pulses from an airgun's source signature, though devices such as wave-shape kits and generator-injector (GI) guns exist for this purpose. Instead, the seismic wavelet may be most easily

[1]Note that, in the geophysics community, it is customary to show the source signature of an airgun with the negative surface ghost (*i.e.*, the image source) superimposed. Strictly speaking, the surface ghost is *not* part of the source signature of an airgun: it is actually the time-delayed reflection of the source signature from the sea surface. Geophysicists include the surface ghost in the "signature" of an airgun because reflections on a seismic trace are almost always near vertical incidence. Airgun "source signatures" presented in this section adhere to this practice of superimposing the surface ghost in order to facilitate comparisons with data. However, the reader should be aware that the actual source signatures computed by the airgun array model do not include the image source; nor is the contribution of the image source included when computing the source level in third-octave bands, as is done in the last section of this chapter.

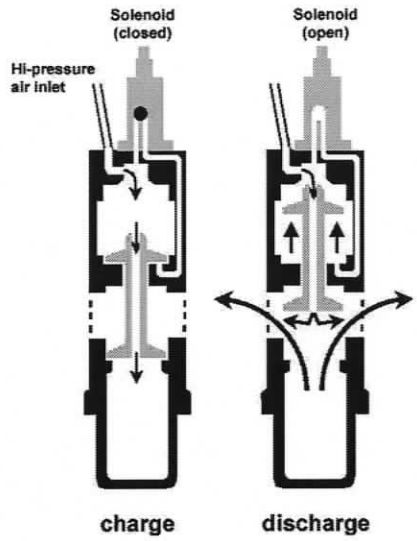

Figure 2.1: Functional diagram of an airgun, showing a cross-section of the gun during charging (left) and firing (right); arrows indicate the direction of airflow. Image is courtesy Veritas DGC Inc. and is reproduced with permission from Fontana (2002).

and effectively improved upon by simply adding together the signatures of many different airguns in an array. When multiple airguns of several different volumes are fired simultaneously, the initial peaks add constructively, whereas the bubble pulses tend to add out of phase, as shown in Figure 2.2(b). The resulting seismic wavelet has an initial peak that is larger in relation to the bubble pulse and is thus better for seismic profiling.

2.2 Airgun bubble oscillation and radiation

The sound generated by an airgun is caused by the expansion and contraction of the bubble of air that is released when the airgun is fired. Since the introduction of the airgun as a seismic source, several investigators have attempted to develop a model of the acoustic radiation from an airgun bubble. The first investigator to publish a physical model of airgun radiation was Ziolkowski (1970). Though Ziolkowski's original airgun model did not account for important effects such as bubble damping, port throttling and pressure interactions (which are discussed presently), all subsequent treatments of the subject have been based on his formulation of the bubble physics.

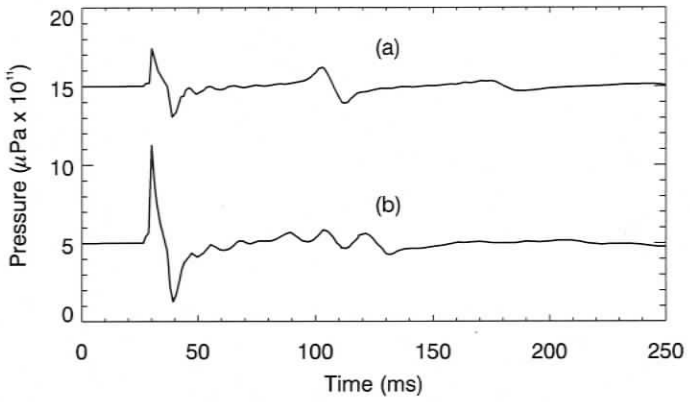

Figure 2.2: (a) Example source signature for a single 80 in^3 airgun at 6 m depth. (b) Example source signature for a three airgun array — 40 in^3, 80 in^3 and 185 in^3— at 6 m depth. Data are reproduced from Racca and Scrimger (1986).

Ziolkowski's model for a single airgun is based on Gilmore's equation of motion for a large[2] bubble of air oscillating in an infinite, compressible, inviscid liquid (Gilmore, 1952):

$$\frac{du}{dt} = \frac{\left(1+\frac{u}{c}\right)H + \frac{a}{c}\left(1-\frac{u}{c}\right)\frac{dH}{dt} - \frac{3}{2}u^2\left(1-\frac{u}{3c}\right)}{a\left(1-\frac{u}{c}\right)} \tag{2.1}$$

The terms in Gilmore's equation are as follows:

$$\begin{aligned} a &: \text{ bubble radius} \\ u &: \text{ bubble wall velocity } \left(u = \tfrac{da}{dt}\right) \\ c &: \text{ speed of sound in liquid} \\ H &: \text{ enthalpy at bubble wall} \end{aligned} \tag{2.2}$$

The derivation of Gilmore's equation is very involved and, for brevity, it will not be repeated here; a detailed derivation may be found in Hickling and Plesset (1964). The assumption of inviscid flow ($\nabla \times \mathbf{u} = 0$) and the absence of boundaries in Gilmore's formulation of the bubble dynamics result in a spherically symmetric solution. Therefore, the

[2]The airgun bubble is assumed to be large enough that we may ignore the effects of surface tension and gas diffusion at the bubble wall.

shape of the bubble is implicitly assumed to be spherical and the volume of the bubble, V, is proportional to the cube of the radius:

$$V(a) = \frac{4}{3}\pi a^3 \tag{2.3}$$

The thermodynamic properties of the gas bubble (*i.e.*, pressure, volume and temperature) are encapsulated in the enthalpy term:

$$H = \int_{P_a}^{P_\infty} \frac{dP}{\rho_w} \tag{2.4}$$

where P_a is the pressure at the bubble wall, P_∞ is the hydrostatic water pressure and ρ_w is the water density. Note that the hydrostatic pressure is given by the formula:

$$P_\infty = P_{\text{atm}} + \rho_w g z_g \tag{2.5}$$

where P_{atm} is the atmospheric pressure, g is the acceleration due to gravity and z_g is the firing depth of the airgun. Though Gilmore's equation (Eq. 2.1) was derived for compressible liquids, satisfactory results are obtained assuming the water density ρ_w is independent of pressure:

$$H = \frac{P_\infty - P_a}{\rho_w} \tag{2.6}$$

The airgun bubble is assumed large enough that we may neglect surface tension at the bubble wall, which is small compared to the internal pressure; thus, P_a is equal to the gas pressure inside the bubble. Ziolkowski assumes that the bubble is filled with a fixed volume of ideal gas that obeys an equation-of-state of the form:

$$P_a = P_0 \left(\frac{V(a_0)}{V(a)} \right)^\gamma = P_0 \left(\frac{a_0}{a} \right)^{3\gamma} \tag{2.7}$$

where P_0 and a_0 are the initial pressure and radius of the bubble, and $1.0 \leq \gamma \leq 1.4$. Note that $\gamma = 1$ for isothermal expansion and $\gamma = 1.4$ for adiabatic expansion. In practice, the gas inside the bubble expands neither isothermally nor adiabatically, but somewhere in between, as was shown experimentally by Ziolkowski (1970, Fig. 6) who obtained a value

of $\gamma = 1.13$ for real airguns[3].

Equations 2.1–2.7 describe a system of ordinary differential equations that can be solved, using standard numerical methods, to yield the bubble radius, velocity and pressure as functions of time. The solutions to these differential equations only depend on the initial conditions: a_0, u_0 and P_0. In Ziolkowski's original formulation, the following initial conditions are assumed:

1. The initial pressure of the bubble, P_0, is that of the charged airgun $P_0 = P_g$.

2. The initial bubble volume, V_0, is equal to that of the charged airgun, V_g. Thus, the initial bubble radius is $a_0 = \sqrt[3]{3V_g/(4\pi)}$.

3. The initial velocity of the bubble wall is computed from 2.1, assuming that du/dt and dH/dt are much larger than the other terms at the first instant; this gives $u_0 = (P_\infty - P_g)/(\rho_w c)$ (Ziolkowski, 1970, Eq. 56).

Once solutions to the bubble motion equations have been obtained, the radiated overpressure, $p = P(r) - P_\infty$, at distance r from the bubble is given by:

$$p(r,t') = \frac{\rho_w a(t')}{r}\left(H(t') + \frac{u(t')^2}{2}\right) \tag{2.8}$$

where the retarded time is $t' = (t - r/c)$ (Landrø, 1992, Eq. 4). The acoustic source signature of the airgun is given by equation 2.8 when $r = 1$ m.

Figure 2.3 shows an airgun signature computed using Ziolkowski's basic model compared with experimental data. One can see that the general shape of the airgun signature predicted by Ziolkowski's model is correct and that the period of the bubble oscillations is in good agreement with the experimental data. However, the initial pulse amplitude in Figure 2.3 is far too high because Ziolkowski's initial conditions assume that all the air is released from the gun chamber instantaneously (note the different scales on the left and right hand plots in Figure 2.3). This assumption is not realistic because the gun ports throttle the air flow from the gun chamber. As well, the decay of the bubble oscillations in Figure 2.3 is much too slow because Equation 2.1 only accounts for damping via acoustic

[3]Ziolkowski actually used the parameter $b = 3\gamma$ and obtained a value of $b = 3.4$; this is equivalent to $\gamma = 1.13$.

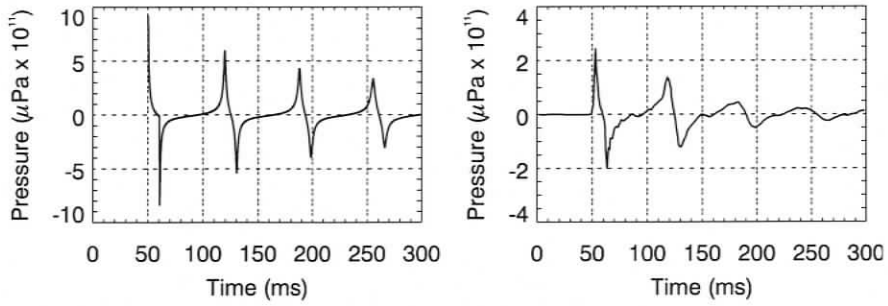

Figure 2.3: Comparison of Ziolkowski's basic model (left) and experimental data (right) for the far-field signature below a single 80 in^3 airgun fired at 8 m depth. Note the different pressure scales on the two plots. Data are reproduced from Racca and Scrimger (1986).

radiation. In reality, significantly more energy is lost from the airgun bubble due to heat transfer to the surrounding water. Thus additional physics must be incorporated into the basic model in order to correctly simulate real airgun behaviour.

2.3 Bubble damping, port throttling and bubble motion

In Ziolkowski's original model, the neglect of air flow and heat transfer is implicit in the air-bubble thermodynamics encapsulated in Equation 2.7: this form of state-equation is only appropriate for a fixed volume of gas in a closed thermodynamic system. However, the airgun bubble is clearly an open thermodynamic system, with air-mass injected from the gun chamber and heat lost to the surrounding water at the bubble wall. Starting from the conservation of energy for an open, quasi-static thermodynamic system, the investigator Landrø (1992, Appendix B) showed that the energy gained by the airgun bubble, due to mass transfer and conductive heat loss, must be balanced by the change in internal energy of the air bubble according to the following relation:

$$c_P T\frac{dm}{dt} + \frac{dQ}{dt} = \frac{dU}{dt} + P\frac{dV}{dt} \tag{2.9}$$

where T is the temperature of the air bubble, m is the mass of air in the bubble, $U = c_V mT$ is the internal energy of the bubble, c_P and c_V are the heat capacity of the air at constant

pressure and volume, respectively, and dQ/dt is the rate of heat transfer into the air bubble. If the air inside the bubble is assumed to obey the ideal gas law then this equation can be re-written in terms of the gas constant $R_g = c_P - c_V$:

$$\frac{dT}{dt} = \frac{R_g T \frac{dm}{dt} - \frac{dQ}{dt} - P\frac{dV}{dt}}{mc_V} \tag{2.10}$$

When combined with Gilmore's formulation of the bubble dynamics, Equation 2.10 completely determines the state of air inside the airgun bubble, provided that the rates of mass-injection from the airgun chamber (dm/dt) and heat-loss to the water (dQ/dt) can be constrained.

The heat loss term in Equation 2.10 controls the damping of the airgun bubble and also influences the period of bubble oscillation. In applying Equation 2.10 to the problem of modelling GI-injector guns, Landrø (1992, Eq. 3) neglects heat transfer between the air bubble and the water (*i.e.*, he sets $dQ/dt = 0$) and instead replaces the heat capacity, c_V, in Equation 2.10 with an effective heat capacity $c_V^{\text{eff}} > c_V$. Though Landrø's approach permits the bubble period to be matched to experimental data, it does not account for damping of the bubble oscillation due to heat loss. Thus, we take a different approach here and retain the heat transfer term in the bubble model, in a manner similar to that of Laws et al. (1990). It has been found that retaining heat transfer across the bubble wall completely accounts for the damping of the bubble oscillation without introducing *ad hoc* viscous-like damping terms into Equation 2.1.

If we assume that the water behaves as a temperature reservoir (a reasonable assumption, since the heat capacity of water is much higher than that of air) then we expect the rate of heat loss from the air bubble to be proportional to the temperature difference between the bubble and the water and the area of the water-bubble interface. Assuming a spherical bubble and introducing a heat transfer coefficient κ, we obtain the following expression for the rate of heat loss from the air bubble:

$$\frac{dQ}{dt} = \kappa\left(4\pi a^2 \Delta T\right) \tag{2.11}$$

where $\Delta T = T - T_w$ is the temperature difference between the bubble and the surrounding water and the value of κ remains to be determined by fitting the model to experimental

data. It may seem that we have violated the the quasi-static assumption in Equation 2.10 by assuming a temperature difference at the air-water interface: clearly the gas at the bubble wall is not in equilibrium with the water. However, this apparent difficulty is resolved by Laws et al. (1990), who postulate that the heat transfer takes place in very thin, laminar boundary layers (approximately 100 microns thick) at the interface. The system is assumed to be infinitesimally close to equilibrium everywhere except in the very thin boundary layers and thus we can apply the thermodynamic relations for a quasi-static process to the bubble oscillation.

The rate of air-flow from the airgun chamber controls the amplitude of the sharp initial peak of the airgun pulse; the shape of the initial peak, in turn, has a strong influence on the oscillation period of the airgun bubble. When the airgun is initially fired, air is injected from the pressurized gun chamber into the air bubble via a throttled flow through the airgun ports. In general, the rate of air-flow depends on the specific design of the airgun in question; however we expect the rate of air-flow from the gun chamber to increase with the total area of the gun ports, A, the pressure differential across the gun ports, ΔP, and the density of air in the gun chamber, ρ_g. Based on a dimensional analysis, we expect the rate of mass injection from the gun chamber to be proportional to these quantities according to a relationship of the following form (*c.f.* Laws et al., 1990, Eq. A-6):

$$\frac{dm}{dt} \propto A\sqrt{\rho_g \Delta P} \tag{2.12}$$

To derive a mass-transfer equation, we introduce a constant of proportionality, τ, which specifies the rate of flow through the airgun ports:

$$\frac{dm}{dt} = \tau\sqrt{(P_g - P_a)m_g/V_g} \tag{2.13}$$

where $\Delta P = P_g - P_a$ is the pressure difference between the gun chamber and the air bubble, m_g is the mass of air inside the gun chamber and V_g is the volume of the gun chamber. Note that we have absorbed the port area, A, into the throttling constant, τ, since the the area of the gun ports is fixed — we assume that only the chamber size varies between different volumes of guns.

The initial mass of air in the gun chamber is calculated from the airgun volume, V_g, fir-

ing pressure, P_0, and firing temperature, $T_g|_{t=0}$ (set equal to the water temperature). However, the extremely high pressure of air in the gun chamber (typically from 10–14 MPa) causes the air to depart from the ideal gas law and so a modified state-equation must be used instead. Laws et al. (1990, Eq. A-8) suggest a modified ideal gas law of the form:

$$P_g V_g = m R_g T_g' \tag{2.14}$$

where T_g' is an effective temperature that depends on the pressure of the gun chamber:

$$T_g' = T_g (1 + P_g/P_c) \tag{2.15}$$

where P_g is the gun chamber pressure and the constant $P_c = 139$ MPa for air.

An additional physical effect, which is observed in real airgun bubbles, but was neglected in Ziokowski's original model, is the vertical rise of the airgun bubble. The buoyancy of the air bubble causes it to rise to the surface as it oscillates and the resulting change in hydrostatic pressure affects the bubble period. The expression for the vertical velocity of a gas globe underwater was derived by Herring (1941):

$$\frac{dz_b}{dt} = \frac{2g}{a^3} \int_0^t a^3 dt \tag{2.16}$$

where z_b is the depth of the air bubble and g is the acceleration due to gravity. The vertical rise of the air bubble introduces a time-dependence to the expression for the hydrostatic pressure in the airgun model (*i.e.*, in Equation 2.5).

2.4 Additional model parameters

The airgun model developed thus far contains two empirical parameters, which must be constrained using experimental data: κ the heat transfer constant and τ the port throttling constant. In practice, two additional empirical parameters were required for the model to agree with real airgun behaviour: the mass-release efficiency of the gun chamber, η and a port-throttling power law exponent, β.

In a real airgun, the firing mechanism of the airgun is not 100% efficient and so, after the airgun is fired, some air remains in the gun chamber after the gun ports close. This

results in a smaller effective mass being transferred from the gun chamber to the bubble, thus reducing the bubble pulse period. In the model, this effect has been encapsulated in the efficiency parameter η, which is the fraction of the total air-mass released from the gun chamber:

$$\eta = \frac{m_{t=\infty}}{m_{\text{gun}}} \tag{2.17}$$

where $m|_{t\infty}$ is the air-mass released into the bubble and m_{gun} is the total air-mass in the gun chamber.

In comparing predictions of the model to source signature data for multiple airguns, an additional dependence of the port-throttling constant, τ, on the airgun volume was inferred: the rate of mass injection was found to be greater for larger guns. This dependence of the throttling rate on the airgun volume is not accounted for by Equation 2.13 and so an additional empirical parameter was introduced to account for this effect. It was postulated that the rate of mass injection in Equation 2.13 depends on the airgun volume according to some power law:

$$\tau = \tau_0 (V_g)^{\beta} \tag{2.18}$$

where τ_0 is the volume-independent port-throttling constant and the β is a power law exponent that must be determined by comparison with data. Introducing this power law dependence of the mass injection rate on the airgun volume substantially improved the agreement between the model and observed airgun behaviour. Thus the final model has four empirical parameters that must be fit to airgun data.

2.5 Airgun bubble interactions

The additional effect of near-field pressure interactions between closely spaced airguns must be taken into account to correctly model the far-field signatures of airguns in an array. The investigators Giles and Johnston (1973) showed experimentally that the bubble pulse period of an airgun is altered when it is fired in close proximity to other guns. This is because, at short range, the pressure field from an airgun is significant compared to the hydrostatic pressure. Since the bubble pulse period of an airgun depends on the ambient pressure, guns fired close together influence each others' pressure signatures; this effect is called airgun interaction.

Ziolkowski et al. (1982) demonstrated that the effect of near-field pressure interactions on the signatures of airguns in an array can be accounted for by adding a time-varying interaction term to the hydrostatic pressure at each gun. The effective hydrostatic pressure at gun i is given by the hydrostatic pressure at depth, P_∞, plus the sum of the pressure contributions of all the other guns in the array:

$$P_i^{\text{eff}}(t) = P_\infty + \sum_{k \neq i} \Delta p_{ik}(t) \tag{2.19}$$

where $\Delta P_{ik}(t)$ is the perturbation of the hydrostatic pressure at gun i due to gun k. The pressure perturbation, $\Delta P_{ik}(t)$, is the time-delayed and distance-scaled pressure signature at gun i from gun k, which is given by Equation 2.8:

$$\Delta P_{ik}(t) = \frac{\rho_w a_k(t')}{D_{ik}} \left(H_k(t') + \frac{u_k(t')}{2} \right) \tag{2.20}$$

where D_{ik} is the inter-bubble distance between gun i and gun k, t' is the retarded time and a_k, u_k and H_k are the radius, velocity and enthalpy of bubble k. Note that the contribution of surface-reflected image sources to the interaction pressure is significant and must be included in the summation of Equation 2.19.

2.6 Initial conditions

The addition of new model physics requires a different set of initial conditions for the airgun bubble from those of Ziolkowski's original model:

1. The initial pressure inside the bubble, $P_a|_{t=0}$ is set to the hydrostatic pressure, P_∞.
2. The initial velocity of the bubble wall, u_0, is set to zero. Conditions 1 and 2 ensure that the initial overpressure at $t = 0$ is zero (*c.f.* Equation 2.8).
3. The initial bubble volume is set equal to the airgun chamber volume so that $a_0 = \sqrt[3]{3V_g/(4\pi)}$. It is necessary to choose a small initial radius for the bubble to ensure that the denominator of Equation 2.1 (the equation of motion for the air bubble) is non-zero. In practice, the volume of the airgun is much smaller than the equilibrium radius of the bubble.

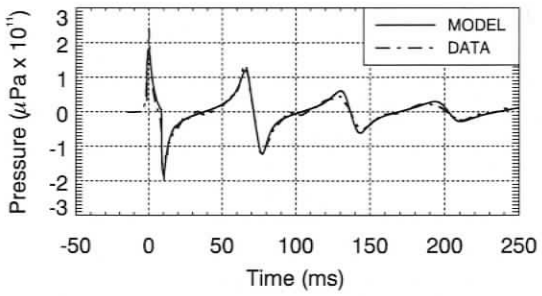

Figure 2.4: Comparison of improved airgun model with the far-field signature from a single 80 in^3 airgun fired at 8 m depth.

4. The bubble is filled with an initial mass consistent with conditions 1 and 3 so that $m_0 = P_\infty V_g / R_g / T_g|_{t=0}$. At ambient pressure, the initial mass of air in the bubble is less than 1% of the total air mass inside the gun.

Figure 2.4 shows a comparison of an airgun signature computed using the improved model with actual airgun data. Note that the model parameters τ, κ and η have been adjusted for optimal agreement between the model and experimental data. It is apparent from the figure that, with the addition of the new physics to the model, the agreement between modelled and measured airgun signatures is much improved.

2.7 Model implementation

The equations presented in the preceding sections, along with their initial conditions, form a system of ordinary differential equations that describe the oscillation and radiation of one or more airgun bubbles. These differential equations must be solved in parallel, using a numerical integration scheme, in order to compute the overpressure signature from an airgun array. Thus, a Fortran program, `AASM` (Airgun Array Source Model), was written to solve the equations of motion for a collection of airgun bubbles and to compute the far-field signature of an array.

`AASM` integrates the ODE's using the adaptive embedded fourth order Runge-Kutta numerical integration method described in Press et al. (1990, §16.3). The adaptive solver au-

tomatically adjusts the numerical integration step-size in order to achieve an arbitrary level of accuracy while solving the equations of motion. The extra accuracy achieved using the adaptive step size solver is important in computing signatures for large arrays of airguns, where the influence of many simultaneous pressure interactions on the bubble motions are significant.

The inputs to the AASM computer model are as follows:

1. The array firing pressure, P_g.
2. The 3-D position of each gun (x_i, y_i, z_i).
3. The volume of each gun V_i.
4. The heat conduction constant, κ.
5. The port-throttling constant, τ_0.
6. The mass-release efficiency η.
7. The port-throttling power law exponent, β.
8. The fractional tolerance for the adaptive Runge-Kutta integrator, ε. This value is chosen to be sufficiently small so that the model converges. A value of $\varepsilon = 10^{-6}$ has been found to be adequate for most applications.

Optimal values for the parameters κ, τ_0, η and β were determined by fitting the model to a collection of real airgun signature data, as discussed in the next section. Given the input parameters, AASM solves the parallel dynamical equations for a collection of oscillating airgun bubbles, taking into account interactions between the guns. For each airgun bubble, the model computes the radius, $a_i(t)$, velocity, $u_i(t)$, bubble pressure, $P_{ai}(t)$ and enthalpy, $H_i(t)$, as functions of time. The output of the computer model is the collection of far-field signatures of all the airguns in the array, computed using Equation 2.8.

2.8 Model optimization

In general, the empirical model parameters may be adjusted to replicate individual airgun signatures to a high degree of accuracy (*c.f.* Figure 2.4). However, in order to make the

airgun model generally applicable, a set of model parameters is required that gives the best agreement between model and data for a wide range of different airgun signatures. Thus, a global-optimization scheme was used to fit the output of the airgun model to a large library of airgun source signature data.

A collection of high-quality source signatures, for single airguns, were obtained from a Defence Research Establishment Pacific (DREP) technical report by Racca and Scrimger (1986). These data were collected as part of a seismic source signature study conducted in Jervis Inlet aboard the CNAV Endeavour — the senior scientist of this study was N. Ross Chapman, formerly of DREP. Unfortunately, the original digital waveform data from the study were lost; however, the source signature plots from the technical report were of sufficient quality to permit re-digitization of the data, using electronic digitization software. The dataset contains a collection of 38 back-propagated source signatures for five different Bolt 600/B airguns. The signatures in the dataset were measured at 100 metres depth, directly beneath the airguns, and corrected for spherical spreading. The volumes of the airguns in the dataset are 5 in^3, 10 in^3, 40 in^3, 80 $in^3$and 185 in^3 and the firing depths of the airguns range from 0.5 m to 10 m.

Best-fit values for the four model parameters were obtained using a simulated annealing global optimization algorithm to fit the airgun model to the experimental source signature data. The simulated annealing algorithm, as described by Kirkpatrick et al. (1983), is a general method for finding the global minimum of some cost function $E(\mathbf{x})$ of an n-dimensional parameter space $\mathbf{x} = (x_1, x_2 \ldots x_n)$. Simulated annealing is useful for finding the global minimum of functions with many local minima because, unlike downhill optimization methods, simulated annealing avoids getting trapped in local minima by accepting trial models in both the uphill (greater cost) and downhill (lower cost) directions. The reader is referred to the article by Kirkpatrick et al. (1983) for specific details regarding the algorithm implementation. Final quenching was performed using a simplex-method local optimization algorithm (Press et al., 1990, §10.4) to refine the five best-fit models.

In this case, the parameter space was the range of possible values for the four model parameters:

$$\mathbf{x} = (\kappa, \tau_0, \eta, \beta) \tag{2.21}$$

where

$$\begin{aligned} 0 &< \kappa < \infty \\ 0 &< \tau_0 < \infty \\ 0 &< \eta < \infty \\ 0 &< \beta < \infty \end{aligned}$$

The cost function, $E(\mathbf{x})$, which is the mismatch between the model and data, was chosen to be the total mean-square difference between the modelled and measured airgun signatures:

$$E(\kappa, \tau_0, \eta, \beta) = \frac{1}{M} \sum_{i=1}^{M} \frac{1}{N} \sum_{k=0}^{N-1} \left(s_d^{(i)}(k\Delta t) - s_m^{(i)}(k\Delta t) \right)^2 \tag{2.22}$$

where $s_d^{(i)}$ and $s_m^{(i)}$ are the data and model overpressure signatures for airgun i respectively. Model and data signatures were tabulated on a fixed time step Δt and the total number of airgun signatures was $M = 38$.

The results of the simulated annealing optimization are shown in Figures 2.5 and 2.6. The first figure shows scatter plots of the model/data mismatch for each of the four model parameters from the simulated annealing optimization; the best-fit parameter values, as determined from the optimization are as follows:

$$\begin{aligned} \kappa &= 22230 \quad \mathrm{J/m^2/s} \\ \tau_0 &= 0.09115 \quad \mathrm{m^{3/2}\sqrt{mol/Pa}} \ \text{(at 1 m}^3\text{)} \\ \eta &= 0.8317 \\ \beta &= 0.520 \end{aligned} \tag{2.23}$$

Figure 2.6 shows 38 plots comparing the optimized airgun model output with reference signatures from the DREP airgun signature library. From the figure, one can see that the overall match between the model and data signatures is quite good and that the model accurately predicts source signatures for many different airgun volumes and firing depths.

2.9 Far-field summation

After the airgun array source model is executed, the resulting airgun signatures must be summed together with the appropriate phase delays to obtain the far-field source signature

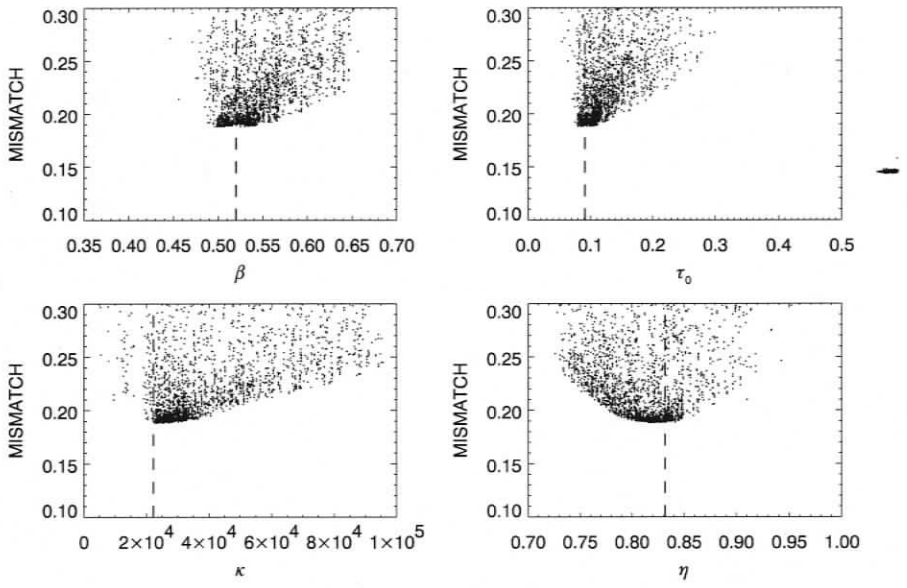

Figure 2.5: Scatter plots of model mismatch versus parameter values for heat-conduction constant, κ, port-throttling constant, τ_0, mass-release efficiency, η, and power law exponent, β. Optimal parameter values determined by simulated annealing optimization are indicated by dashed vertical lines.

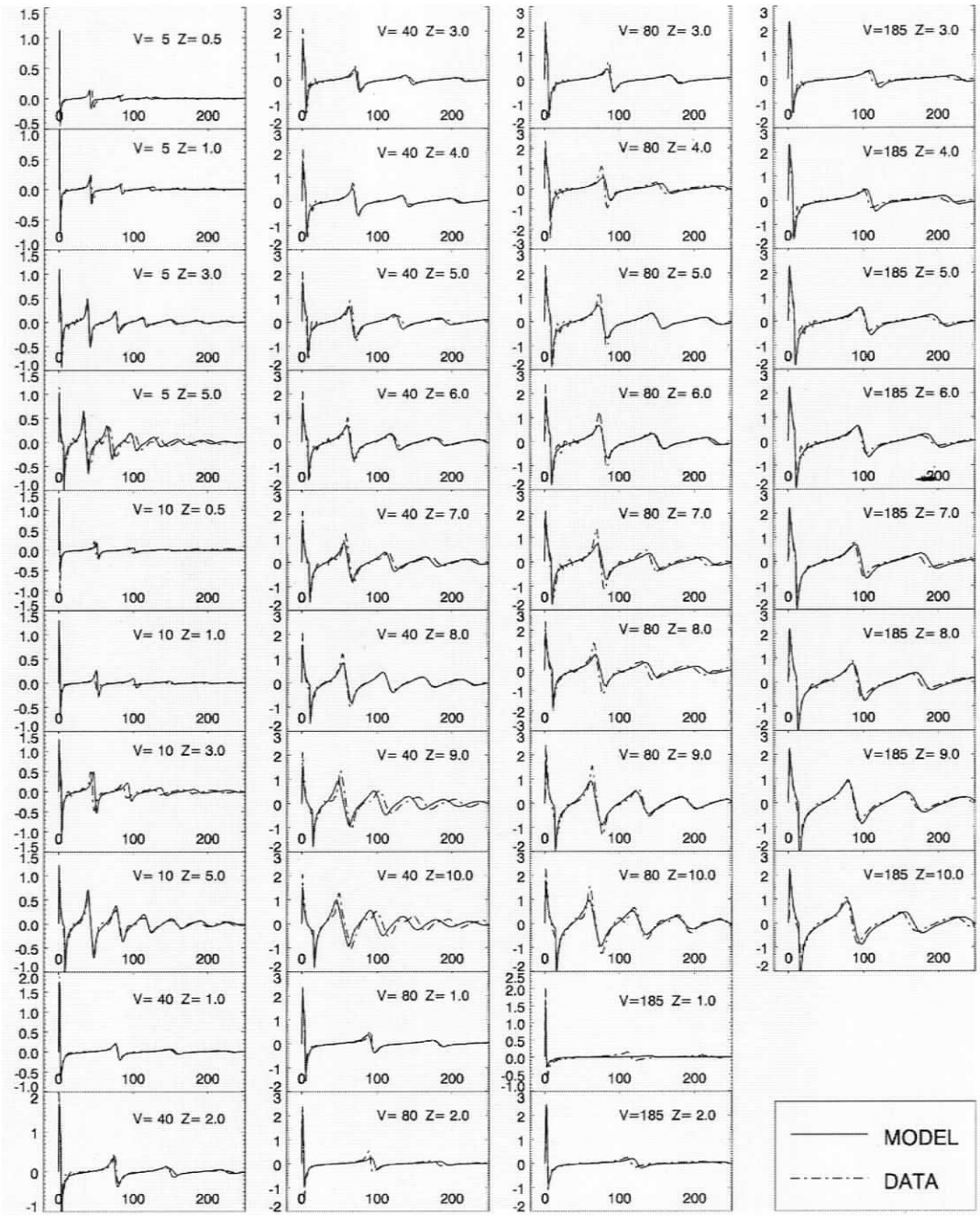

Figure 2.6: Plots comparing source signature waveform data with output of optimized airgun model. Time units are milliseconds and pressure units are bars. Airgun volumes (in cubic inches) and depths (in metres) are indicated in plot annotations.

of the array. The far-field signature of an array, $p_{\mathrm{ff}}(t)$ is the sum of the pressure signatures of the individual guns, $p_i(t)$, time delayed according to their relative position and the propagation angle:

$$p_{\mathrm{ff}}(t) = \sum_{i=1}^{N} p_i(t - \tau_i(\theta, \phi)) \tag{2.24}$$

where τ_i is the time-delay of the ith gun, θ is the horizontal (or azimuthal) angle of propagation and ϕ is the vertical angle of propagation.

The propagation model RAM, discussed in the next chapter, calculates transmission loss for a non-directional, point-like acoustic source. However, an airgun array is clearly a directional source, with prominent signature variations in both the θ and ϕ directions. One can account for the horizontal directionality of an airgun array (*i.e.*, in the θ plane) by using different source levels for different azimuth angles but RAM does not directly account for the vertical directionality of the airgun array (*i.e.*, in the ϕ plane). Thus, in order to couple the output of the airgun model with the acoustic field computed using RAM we need to pick a single source level for the airgun array for each θ. We know that, beyond several water depths from the array, the acoustic field is dominated by energy propagating at shallow grazing angles less than the critical angle in the bottom (see page 35). Thus we assume here that the source level "seen" horizontally away from the array is the horizontally propagating signature in the $\phi = 0$ direction. This assumption underestimates the source level at steep propagation angles and is invalid directly below and above the array and at very short ranges where steep propagation angles are important. However the energy propagating at steep angles is quickly absorbed into the bottom as the range increases and does not contribute significantly to the field at ranges greater than a few water depths.

For horizontal sound propagation the time delay is only a function of the azimuthal angle, θ:

$$\tau_i = -\left(x_i \cos\theta + y_i \sin\theta\right)/c \tag{2.25}$$

where (x_i, y_i) is the position of gun i in the plane of the array and c is the speed of sound. A diagram illustrating the geometry of the far-field summation is shown in Figure 2.7. It is often more convenient to perform this calculation in the frequency domain by utilizing the Fourier transform shift theorem, which states that a time delay of τ corresponds to a phase

delay of $2\pi f\tau$, so that:

$$\mathscr{P}_{\mathrm{ff}}(f,\theta) = \sum_{i=1}^{N} \mathscr{P}_i(f) \exp\left(\frac{j2\pi f}{c}(x_i\cos\theta + y_i\sin\theta)\right) \tag{2.26}$$

where f is frequency, $j = \sqrt{-1}$ and $\mathscr{P}(f)$ denotes the Fourier transform of $p(t)$.

We can use the frequency domain representation of the source signature to compute third-octave band source levels:

$$SL(f_c,\theta) = 10\log_{10}\left[\int_{f_l}^{f_u} |\mathscr{P}_{\mathrm{ff}}(f,\theta)|^2\, df\right] \tag{2.27}$$

where $SL(f_c,\theta)$ is the source level (in dB units) in a third-octave band with centre frequency f_c, in the azimuthal direction θ. Note that the limits of integration in this equation, f_l and f_u, are the lower and upper frequency bounds of the third-octave band such that

$$f_u = 2^{1/3} f_l \qquad \text{and} \qquad f_c = \sqrt{f_l f_u}$$

The resulting source levels may be combined with transmission loss computed by a propagation model to yield received sound levels in third-octave bands.

An airgun array consists of many sources and so the point-source assumption is not valid in the near field, where the array elements do not add coherently. The distance to the near field of an array is given by the expression:

$$R_{\mathrm{nf}} < \frac{L^2}{4\lambda} \tag{2.28}$$

where λ is the sound wavelength and L is the longest dimension of the array (Lurton, 2002, §5.2.4). Beyond this range it is assumed that an array radiates like a point source and can be treated as such for the purpose of propagation modelling. For example, if an airgun array has a diagonal dimension $L = 30$ m then the nearfield range at 200 Hz ($\lambda = 7.5$ m) is

$$R_{\mathrm{nf}} < 30 \text{ m}$$

assuming a sound speed in water of 1500 m/s.

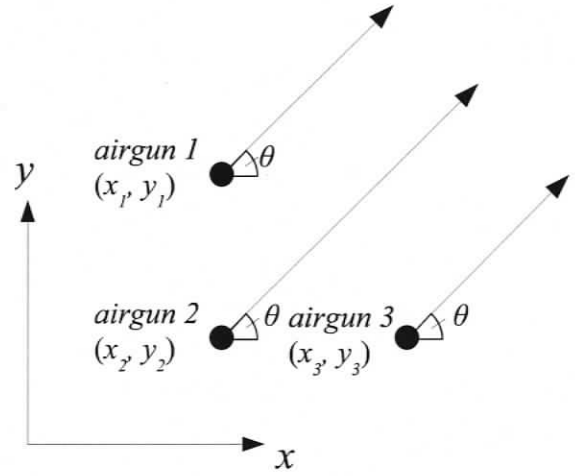

Figure 2.7: Diagram of airgun array source signature summation geometry (plan-view). Airgun array elements are denoted by filled circles. The arrows indicate the direction of sound propagation, θ.

Chapter 3

Acoustic propagation model

Ocean acoustic propagation models may be divided into four classes, based on the technique that is used to solve the wave equation: ray theory, normal modes, wave-number integration and parabolic equation. Each class of model employs a different set of approximations to render the solution of the wave equation tractable. Thus, each class of model is applicable under different circumstances. The current study has employed the acoustic propagation model RAM[1], which is based on the parabolic equation solution to the acoustic wave equation (Collins, 1993).

Parabolic equation (PE) models solve an approximate "one-way" wave equation that neglects back-scattered sound energy; this is the most efficient class of acoustic model for computing transmission loss at low frequencies in range-dependent environments. RAM solves range-dependent ocean acoustics problems with arbitrary bottom layering and correctly accounts for steep propagation angles by using a wide-angle, Padé series expansion of the PE operator. To account for losses due to shear wave conversion in elastic media, which can be an important sound absorption mechanism in shallow water environments, RAM has been modified to use a complex density equivalent fluid bottom approximation[2] of Zhang and Tindle (1995). The complex density seabed approximation, which was added

[1]RAM is the Range-dependent Acoustic Model, developed by Michael Collins at the Naval Research Laboratory.

[2]The complex density approximation has previously been incorporated into other ocean acoustic models, including the PE-based PECan model (Brooke et al., 2001); however, PECan was unavailable for the current study and so RAM was modified to include this capability instead.

to RAM as part of this thesis project, is a useful improvement to the capabilities of the RAM propagation code.

This chapter discusses the parabolic equation approximation and RAM's implementation of the split-step Padé PE operator. The complex density equivalent-fluid approximation is described and its implementation into RAM is discussed. Finally, a comparison of the modified complex density RAM against a benchmark elastic solution is presented.

3.1 Parabolic equation approximation

In this section, a brief derivation is presented of the split-step Padé expansion form of the parabolic equation approximation as it is implemented in RAM. The derivation given here closely follows that of Collins (1993). We begin with the inhomogeneous form of the Helmholtz equation (*i.e.*, the harmonic wave equation), which describes acoustic wave propagation in a medium with variable sound speed, $c = c(\mathbf{r})$, and density, $\rho = \rho(\mathbf{r})$ (Frisk, 1994, §1.3):

$$\rho \nabla \left(\frac{1}{\rho} \nabla p \right) + k^2 p = 0 \tag{3.1}$$

where p is the acoustic pressure, and $k = \omega / c$ is the wavenumber. In order to derive the parabolic equation approximation, we invoke the following two conditions:

1. The medium must vary weakly with azimuth so we can express the wave equation in cylindrically symmetric coordinates $\mathbf{r} = (r, z)$.

2. The density of the medium must vary weakly with range so that we can assume $\frac{\partial \rho}{\partial r} = 0$.

Given these two conditions we can express the Helmholtz equation in terms of the range and depth derivatives as follows:

$$\frac{1}{r} \frac{\partial}{\partial r} \left(r \frac{\partial p}{\partial r} \right) + \rho \frac{\partial}{\partial z} \left(\frac{1}{\rho} \frac{\partial p}{\partial z} \right) + k^2 p = 0 \tag{3.2}$$

We can simplify the form of the Helmholtz equation by factoring out a cylindrical spreading term of $\sqrt{r}$ from the pressure via the following transformation:

$$p \rightarrow \frac{p'}{\sqrt{r}} \tag{3.3}$$

$$\frac{1}{r}\frac{\partial}{\partial r}\left(r\frac{\partial p}{\partial r}\right) \rightarrow \frac{1}{\sqrt{r}}\frac{\partial^2 p'}{\partial r^2} + \frac{1}{4r^{\frac{5}{2}}}p' \tag{3.4}$$

$$\frac{\partial p}{\partial z} \rightarrow \frac{1}{\sqrt{r}}\frac{\partial p'}{\partial z} \tag{3.5}$$

Changing variables, we write the Helmholtz equation in terms of the new range-reduced pressure:

$$\frac{\partial^2 p'}{\partial r^2} + \rho\frac{\partial}{\partial z}\left(\frac{1}{\rho}\frac{\partial p'}{\partial z}\right) + \left(k^2 + \frac{1}{4r^3}\right)p' = 0 \tag{3.6}$$

If we invoke the further condition that we are in the far-field then $k^2 \gg 1/4r^3$ and we can neglect the second term in the last parenthesis. This puts the Helmholtz equation in the correct form for application of the parabolic approximation. Using operator notation, we write the Helmholtz equation as follows:

$$\left[\frac{\partial^2}{\partial r^2} + \rho\frac{\partial}{\partial z}\left(\frac{1}{\rho}\frac{\partial}{\partial z}\right) + k^2\right]p = 0 \tag{3.7}$$

Note that we have dropped the prime from the range-reduced pressure for the sake of succinctness. With the Helmholtz equation given in this form we can factor the bracketed term $[\cdots]$, which is quadratic in the range operator $\partial/\partial r$:

$$\left(\frac{\partial}{\partial r} + ik_0\sqrt{1+X}\right)\left(\frac{\partial}{\partial r} - ik_0\sqrt{1+X}\right)p = 0 \tag{3.8}$$

where the depth operator X is given by the following expression:

$$X = \frac{1}{k_0^2}\left(\rho\frac{\partial}{\partial z}\left(\frac{1}{\rho}\frac{\partial}{\partial z}\right) + k^2 - k_0^2\right) \tag{3.9}$$

and $k_0 = \omega/c_0$ is the reference wavenumber. In the homogeneous, range-independent case, the left and right parentheses in Equation 3.8 physically correspond to acoustic waves trav-

elling in the inward ($-r$) and outward ($+r$) directions, respectively. If we neglect acoustic energy travelling in the inward direction (*i.e.*, by neglecting back-scattered energy) we obtain the parabolic or "one-way" wave equation:

$$\frac{\partial p(r,z)}{\partial r} = ik_0\sqrt{1+X}\,p(r,z) \tag{3.10}$$

Thus, using the parabolic approximation we have converted Equation 3.1, which is a second-order, partial-differential, boundary value problem, into Equation 3.10, which is a first-order, partial-differential, initial-value problem; this latter kind of partial-differential equation is much easier to solve than the former. All that remains is to find a suitable series expansion for the depth operator $\sqrt{1+X}$. Several numerical methods exist for this purpose; one of the most-powerful for underwater acoustics problems is the split-step Padé method introduced by Collins (1993).

The parabolic equation is a one-way wave equation so we can express the pressure field at $r+\Delta r$ in terms of the pressure field at r by integrating Equation 3.10 over range:

$$p(r+\Delta r,z) = \exp\left(ik_0\Delta r\sqrt{1+X}\right)p(r,z) \tag{3.11}$$

The factor $\exp(\sqrt{1+X})$ can then be expressed in terms of a Padé series expansion:

$$p(r+\Delta r,z) = \exp(ik_0\Delta r)\prod_{j=1}^{n}\frac{1+\alpha_{j,n}X}{1+\beta_{j,n}X}p(r,z) \tag{3.12}$$

where $\alpha_{j,n}$ and $\beta_{j,n}$ are coefficients of an n-term product representation[3] of the Padé series expansion. The number of terms in the expansion determines the angular extent over which the series approximation of the depth operator is valid; higher order expansions yield better accuracy at steeper propagation angles[4] with greater computational cost.

Collins (1993) obtains a numerical solution for Equation 3.12 by expressing the depth operator in terms of implicit finite differences and solving the resulting system of tridiag-

[3]Note that an alternative sum representation of the Padé series expansion can also be used to approximate the operator in Equation 3.12. This form is better suited to parallel processing applications and is utilized in the multi-processor "RAMP" version of RAM, as discussed in the RAM User's Guide (Collins, 1995).

[4]Phase errors associated with various orders of PE operators are discussed in detail in Jensen et al. (1994, §6.2.4).

onal matrices at each range step, Δr. The expression for the field at $r+\Delta r$ in terms of the field at r is solved recursively, as follows:

$$(1+\beta_{j,n}X)\ldots\left[(1+\beta_{2,n}X)\left[(1+\beta_{1,n}X)p(r+\Delta r,z)\right]\right] = \exp(ik_0\Delta r)(1+\alpha_{j,n}X)\ldots\left[(1+\alpha_{2,n}X)\left[(1+\alpha_{1,n}X)p(r,z)\right]\right] \quad (3.13)$$

where the implicit finite difference solution for the innermost pair of brackets is solved iteratively for each of the n terms in the Padé series exansion. This computational method — the so-called "split-step Padé" solution — is implemented in Collins' propagation modelling code RAM.

3.2 RAM transmission loss model

The current study uses the RAM acoustic propagation modelling code for computing acoustic transmission loss in the Queen Charlotte Basin. RAM, which is implemented in Fortran, is widely used in the ocean acoustics community because it accurately solves range-dependent problems with arbitrary bottom layering. RAM employs the split-step Padé form of the PE operator to solve the one-way wave equation, as discussed in the previous section. Note that the marching solution given by Equation 3.12 requires an initial realization of the acoustic field at the first range step, $r=\Delta r$. The starting field implemented in RAM is Collins' PE self-starter (Collins, 1999), which uses the parabolic equation approximation to derive a starting field from a point-like acoustic source.

RAM is also an "energy-conserving" model, which means that the PE operator correctly accounts for conservation of energy in the acoustic field at each range step. Porter et al. (1991) showed that the problem of energy conservation in traditional PE models is due to the "stair-step" representation of range-dependent environments that incorrectly handles boundary conditions at vertical interfaces. Non energy-conserving models can accumulate errors of several dB over sloping bottoms, so energy conservation is important for computing transmission loss in range-dependent environments. To correct for this problem, RAM uses a modified form of the PE operator that matches the acoustic impedance across horizontal and vertical interfaces; Collins and Westwood (1991) showed that this technique correctly accounts for energy conservation in most cases.

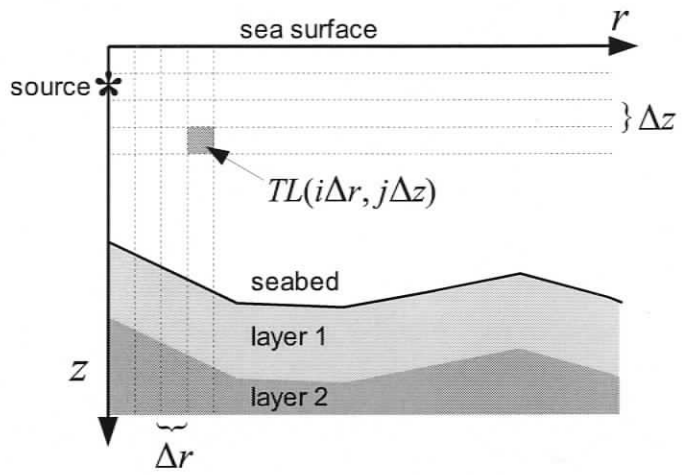

Figure 3.1: Diagram of the discrete range/depth grid on which RAM computes acoustic transmission loss.

RAM computes the pressure field generated by an omnidirectional harmonic point source of unit power. Converted to decibel units, this is equivalent to transmission loss, *TL*:

$$TL(r,z) = -20\log_{10}|p(r,z)| \tag{3.14}$$

which is the reduction of sound intensity caused by spreading and absorption of sound as it propagates through the acoustic environment. The advantage of this approach is that the received sound level *RL* may be computed by simply subtracting the transmission loss *TL* from the acoustic source level *SL*:

$$RL = SL - TL \tag{3.15}$$

Note that these quantities are expressed in decibel units, and are functions of position, frequency and beam angle. In this way, the acoustic transmission loss may be modelled separately from the source, since the transmission loss and source level are assumed to be independent.

RAM computes acoustic transmission loss on a two-dimensional discrete range/depth grid that extends radially outward from the source position, as shown in Figure 3.1. At each range step along the grid, the bathymetry, sound speed profile and geoacoustic profile

of the physical environment are specified. Since RAM uses a finite-difference solver, the numerical convergence of the solution depends on the range and depth resolution of the computation grid, Δr and Δz.

As shown in the previous section, RAM's PE operator was derived under the condition that the azimuthal variation of the environment was small so that out-of-plane refraction could be neglected. Thus RAM is an inherently 2-D propagation code. However, to model the acoustic field in three dimensions, RAM can be run along many closely spaced radials to yield transmission loss as a function of range, depth and azimuth:

$$TL = TL(r, z, \theta) \tag{3.16}$$

This technique, known as N×2-D modelling, neglects the coupling of acoustic energy between radials. A fully three-dimensional acoustic model would be capable of accounting for acoustic coupling between radials but is more than an order of magnitude slower than an equivalent N×2-D model. Given the available time and computing resources, a fully three-dimensional acoustic model could not be applied for the current study. However, the N×2-D result is expected to be sufficiently accurate for most ocean acoustic problems, since the transversely scattered component of the acoustic field is usually quite small.

The particular variant of the RAM code employed in the current study is `RAMGEO`, derived from version 1.5 of the RAM source code. `RAMGEO`, implements a stratified geoacoustic model of the seabed in which multiple bottom layers run parallel to the bathymetry, as shown in Figure 3.1. In addition, the `RAMGEO` code has been modified to use a complex density equivalent fluid bottom for modelling energy loss due to shear conversion at the seabed, as discussed in the next section.

3.3 Complex density approximation

RAM is based upon the PE formulation described in Section 3.1, which is derived from the acoustic (pressure-only) wave-equation. This means that RAM only models propagation of compressional waves (P-waves) in the bottom and thus treats the seabed as a fluid. However, in the real ocean the seabed is composed of multiple layers of elastic (*i.e.*, solid) media which also support shear wave (S-wave) propagation. At the boundary between the

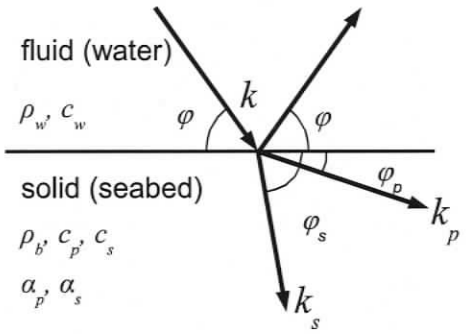

Figure 3.2: Diagram of reflection and transmission at the fluid-solid boundary between the ocean and the seabed.

water and the seabed, acoustic P-waves in the water are converted to both P-waves and S-waves in the bottom, as shown in Figure 3.2. Thus, the reflection coefficient for a solid bottom is different than that for a purely fluid bottom because additional energy is lost to shear wave conversion.

The reflection coefficient for an acoustic plane-wave in water incident upon a homogeneous fluid bottom is (Jensen et al., 1994, §1.6.1)

$$R = \frac{Z_b - Z_w}{Z_b + Z_w} \tag{3.17}$$

where Z_w is the acoustic impedance of water and Z_b is the acoustic impedance of the bottom. The impedances depend on the grazing angle, ϕ, of the acoustic plane wave and are given by the expressions

$$Z_w = \frac{\rho_w c_w}{\sin\phi} \tag{3.18}$$

$$Z_b = \frac{\rho_b c_p}{(1+i\delta_p)\sin\phi_p} \tag{3.19}$$

where c_w and ρ_w are the sound speed and density in water, c_p and ρ_b are the P-wave speed and density in the bottom and the P-wave loss tangent is δ_p. The grazing angles of the incident and transmitted waves, ϕ and ϕ_p, are related by Snell's law:

$$k\cos\phi = k_p\cos\phi_p \tag{3.20}$$

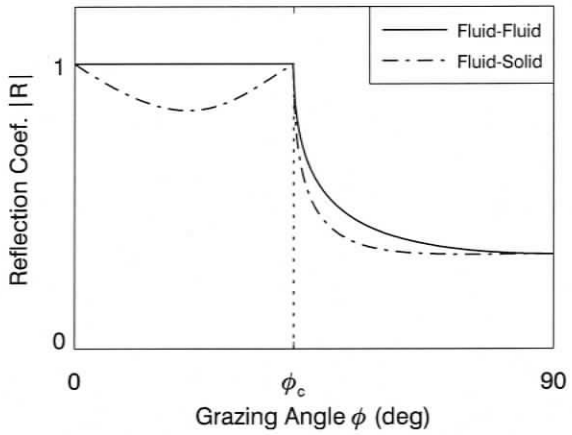

Figure 3.3: Plot of reflection coefficient magnitude $|R|$ versus grazing angle ϕ for a homogeneous fluid bottom (solid line) and a homogeneous solid bottom (dashed line). The critical angle ϕ_c is indicated by the vertical dotted line. Note that the reflection coefficient is shown for a non-attenuating bottom.

The wavenumber in the water is given by $k = \omega/c_w$ and the wavenumber in the bottom is given by $k_p = \omega/c_p(1 + i\delta_p)$. The loss tangent, δ_p, is related to the P-wave attenuation coefficient in the bottom, α_p, by the relationship

$$\delta_p = \alpha_p c_p/\omega \tag{3.21}$$

For a fluid bottom with $c_b > c_w$ (the hard-bottom case in ocean acoustics) there exists a critical angle $\phi_c = \cos^{-1}\phi_w/\phi_p$ beyond which the magnitude of the reflection coefficient is unity:

$$|R|_{\phi \leq \phi_c} = 1 \tag{3.22}$$

as shown by the solid line in Figure 3.3. Thus at shallow propagation angles acoustic energy incident upon a hard fluid bottom is totally internally reflected.

The reflection coefficient for an elastic (*i.e.*, solid) bottom is also given by Equation 3.17 but with the acoustic impedance in the bottom instead given by the expression (Jensen et al.,

1994, §1.6.2)

$$Z_b = \frac{\rho_b c_p}{(1+i\delta_p)\sin\phi_p}\cos^2 2\phi_s + \frac{\rho_b c_s}{(1+i\delta_s)\sin\phi_s}\sin^2 2\phi_s \tag{3.23}$$

where c_s is the S-wave speed in the bottom, δ_s is the S-wave loss tangent and ϕ_s is also given by Snell's law:

$$k\cos\phi = k_s\cos\phi_s \tag{3.24}$$

Note that the acoustic impedance of the solid bottom reduces to Equation 3.19 when $c_s = \phi_s = 0$. In the case of the solid bottom where $c_s < c_w < c_b$, which is usually the case for the ocean waveguide, the reflection coefficient is less than unity at angles beyond the critical angle:

$$|R|_{\phi<\phi_c} < 1 \tag{3.25}$$

as shown by the dashed line in Figure 3.3. Thus acoustic energy incident upon the solid bottom is no longer subject to total internal reflection beyond the critical angle because some energy is converted to transmitted shear waves at small grazing angles.

In shallow water, shear conversion is an important loss mechanism at long range since it strips horizontally propagating acoustic energy ($\phi \to 0$) from the waveguide that would otherwise be trapped by total internal reflection. Thus, in order to accurately model acoustic propagation in shallow water, the elastic properties of the seabed should be taken into account. However, using a fully elastic propagation model requires solving a three-component vector wave equation, which is considerably more complex than using a fluid model. In addition, the computational speed of solving the elastic wave equation is roughly an order of magnitude slower than solving the fluid wave equation.

An alternative approach is to use an "equivalent fluid" seabed model that simulates the reflection coefficient of a true solid seabed. Zhang and Tindle (1995) derived a complex density equivalent fluid model for an solid seabed, which is applicable for low shear-speed bottoms ($c_s < 1000$ m/s). In this approximation, the real-valued density of the fluid bottom in Equation 3.19 is replaced by a complex-valued density:

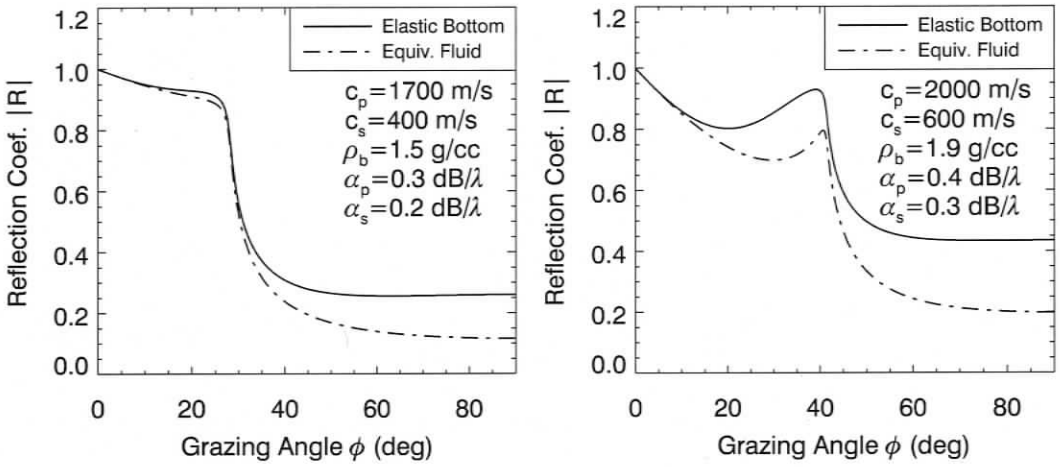

Figure 3.4: Plot of solid bottom reflection coefficient (solid line) compared with complex density equivalent fluid reflection coefficient (dashed line) for two different seabed models.

$$\rho_b' = \rho_b \left[\left(1 - \frac{2}{c_w^2/c_s^2(1+i\delta_s)^2} \right)^2 + \frac{i4\sqrt{1-c_w^2/c_p^2(1+i\delta_p)^2}\sqrt{c_w^2/c_s^2(1+i\delta_s)^2-1}}{c_w^4/c_s^4(1+i\delta_s)^4} \right] \tag{3.26}$$

Zhang and Tindle (1995) obtained this complex density equivalent fluid approximation by equating the fluid and elastic reflection coefficients for small grazing angles $\phi \to 0$; the derivation of ρ' is discussed in their article. Figure 3.4 shows comparisons plots of the reflection coefficient for a solid bottom and the equivalent complex density fluid, for two different sets of bottom parameters. One can see from the plots that the complex density fluid better approximates the solid bottom reflection coefficient at lower shear speeds and that the agreement is best for small grazing angles ($\phi < 10°$).

The complex density equivalent fluid approximation is incorporated into RAM simply by replacing the real-valued density in the bottom, ρ, by the complex density given by Equation 3.26 in the depth operator, X (*c.f.* Equation 3.9). The additional computational overhead is negligible since the fields computed by RAM are already complex-valued. This approach accounts for energy lost from the waveguide due to shear conversion but

does not actually model the propagation of S-waves in the sub-bottom. Thus it presents a considerable computation speed advantage over a full elastic wave propagation model at the cost of sacrificing some accuracy.

A subtle point involved in applying the complex density equivalent fluid approximation is that the value of ρ' depends on the sound speed in water, c_w. The equivalent fluid approximation was derived for the reflection coefficient at the boundary between homogeneous halfspace layers; however, the speed of sound in water in RAM may have a depth dependence, $c_w = c_w(z)$. In order to accommodate an inhomogeneous water column, the sound speed in water in Equation 3.26 is replaced by the mean sound speed over depth, weighted by distance from the seabed:

$$\overline{c_w} = \frac{1}{W}\int_0^{z_b} c_w(z)e^{-(z_b-z)/\lambda}dz \tag{3.27}$$

where z_b is the bottom depth, W is a normalization factor, and the decay coefficient of the exponential weighting function is chosen to be $\lambda = 2\pi/k_0$, the wavelength of sound in the water.

3.4 Model versus benchmark solution

For this thesis project, the RAMGEO version 1.5 code was modified to incorporate the complex density equivalent fluid approximation, as discussed in the previous section; this new variant of the RAM code was designated CRAM (Complex-density RAM). In order to test the validity of the complex density implementation, the output of the CRAM model was compared with a reference solution for a fully elastic problem. The elastic Pekeris waveguide, shown in Figure 3.5, was chosen as the benchmark scenario for testing CRAM, since the analytic solution to this problem is well established.

The k-space Green's function for a homogeneous fluid layer, bounded above by a free surface and below by an arbitrarily layered bottom, is given by Frisk (1994, Eq. 6.18):

$$g(k_r,z) = \frac{i\left[e^{ik_z|z-z_s|} - e^{ik_z(z+z_s)} + R(k_r)e^{2ik_z z_b}\left(e^{-ik_z(z+z_s)} - e^{ik_z|z-z_s|}\right)\right]}{k_z\left(1+R(k_r)e^{2ik_z z_b}\right)} \tag{3.28}$$

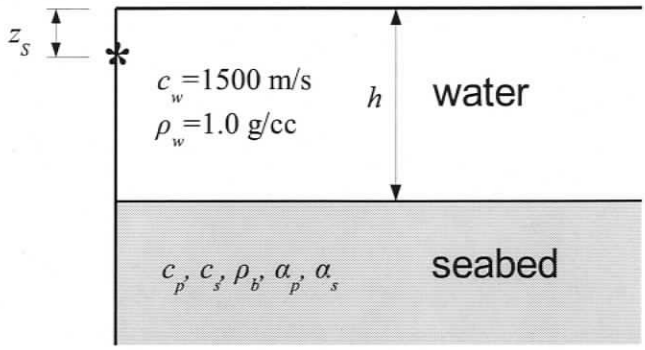

Figure 3.5: Diagram of the elastic Pekeris waveguide benchmark problem. Parameters are the waveguide depth, h, the source and receiver depths, z_s and z_r, and the bottom parameters, c_p, c_s, ρ_b, α_p and α_s.

where k_r and k_z are the horizontal and vertical components of the wavenumber in the fluid layer such that $k^2 = k_r^2 + k_z^2$. Equation 3.28 is equally valid for both fluid and solid bottoms, provided the reflection coefficient of the bottom halfspace, $R(k_r)$, can be determined. For a homogeneous solid bottom, the reflection coefficient is given by Equations 3.17, 3.18 and 3.23 where $k_r = k\sin\phi$ and $k_z = k\cos\phi$. Thus we have a basic analytic reference solution, which we can compare against the output of the `CRAM` model.

The pressure field in the fluid layer is obtained from the Green's function of Equation 3.28 via the inverse Hankel transform (Frisk, 1994, Eq. 4.108):

$$p(r,z) = \int_0^\infty g(k_r,z) J_0(k_r r) k_r dk_r \tag{3.29}$$

where J_0 is the zeroth order Bessel function. The inverse Hankel transform can be computed numerically using FFT's when the Bessel function is replaced by its asymptotic form (Jensen et al., 1994, §4.5.2):

$$p(r,z) \approx \frac{e^{-i\pi/4}}{\sqrt{2\pi r}} \int_0^\infty g(k_r) \sqrt{k_r} e^{ik_r r} dk_r \tag{3.30}$$

This approximate Hankel transform, which is valid in the far-field of the source, is the so-called "fast field approximation". A simple fast field program, implementing Equation 3.30, was written in IDL to integrate the k-space Green's function of Equation 3.28

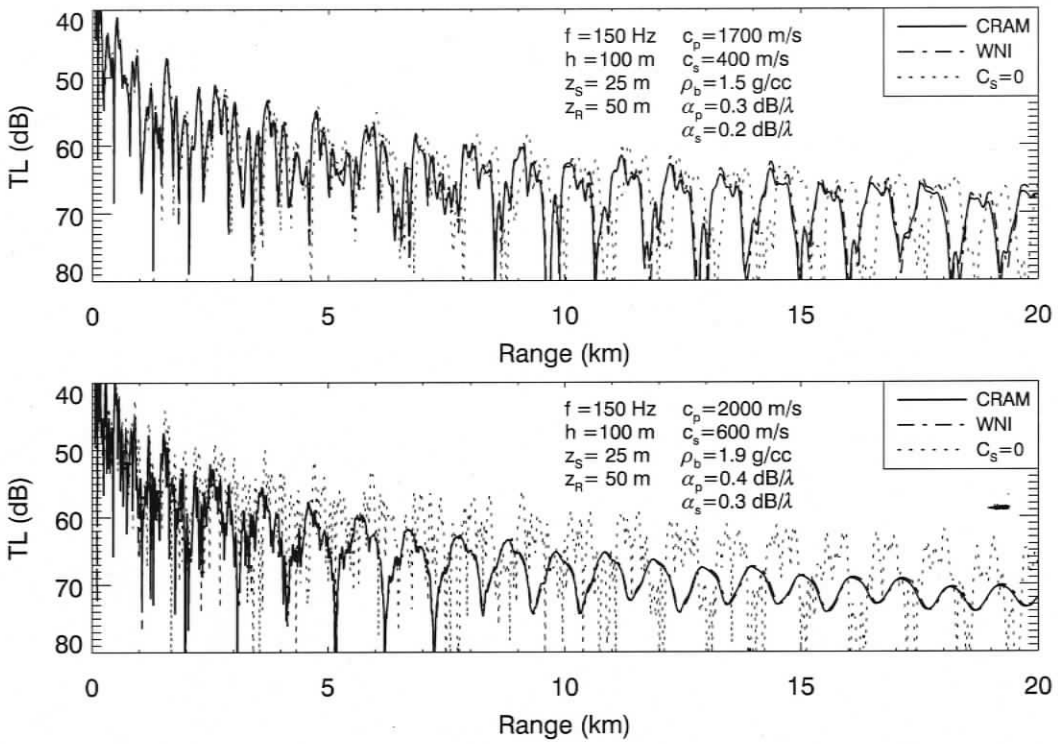

Figure 3.6: Plots of transmission loss showing comparison of the fully elastic benchmark solution (dashed line) to the equivalent fluid complex density approximation (solid line) for two different bottom models. The zero shear, fluid bottom solution (dotted line) is also shown for reference. Benchmark solution was computed using wavenumber integration and approximate solution was computed using CRAM. Frequency is 150 Hz, source depth is 25 m and receiver depth is 50 m.

and thus generate benchmark results for comparison with the output of the CRAM model.

The fast-field program was used to generate reference solutions for two benchmark scenarios with different bottom parameters (*c.f.*, Figure 3.4) at 150 Hz frequency. Figure 3.6 shows a comparison of transmission loss computed using CRAM with the reference solutions. The plots, which show excellent agreement between the exact, solid-bottom reference solutions and the approximate, equivalent-fluid-bottom solutions, demonstrate that the equivalent fluid complex density approximation has been correctly implemented in CRAM and that this approximation is accurate for low shear speed bottoms. This complex density seabed approximation adds new and useful capabilities to the RAM code.

Chapter 4

Physical environment databases

The accuracy of the sound field predicted by an acoustic propagation model is limited by the quality and resolution of the available environmental data. There are three basic kinds of environmental parameters that affect sound propagation in the ocean, and are required as input into an acoustic propagation model:

1. bathymetry data of the ocean depth;
2. sound speed profiles in the ocean;
3. geoacoustic profiles of the sub-bottom.

Accurate bathymetry data are especially important in shallow water, where acoustic propagation is strongly influenced by interaction of sound with the sea bottom. Variations in the depth and slope of the bottom cause sound energy to be scattered and absorbed by the seabed. The ability of a propagation model to accurately reproduce features of the sound field in shallow water depends on the resolution of the available bathymetry data. Digital bathymetry data for the current study were obtained from digital charts provided by the Canadian Hydrographic Service.

The sound speed profile in the ocean can strongly influence long-range acoustic propagation by refracting and trapping sound energy in the water column. The speed of sound in seawater is a function of temperature, salinity and depth. However, temperature and salinity are not static, and changes occur on diurnal and seasonal time scales due to oceanographic mixing and transport processes. These changes in temperature and salinity affect the sound

speed profile. For the current study, representative sound speed profiles for the Queen Charlotte Basin were determined by analyzing historical temperature/salinity profiles, collected by Fisheries and Oceans Canada, and deriving "limiting case" profile shapes.

The geoacoustic properties of the ocean bottom materials govern the degree to which sound is reflected and absorbed at the seabed. However, these environmental data are often the most difficult to obtain. Profiles of geoacoustic parameters versus depth below the seabed may be measured directly from sediment cores but cores are costly to obtain and to analyze and so the availability of this kind of data is limited. Most often, geoacoustic profiles must be inferred from a combination of historical seismic data and knowledge of the local geology. For the current study, geoacoustic profiles for the seabed were estimated from surficial geology charts and interpreted seismic cross-sections for the Queen Charlotte Basin, published by the Geological Survey of Canada.

4.1 Bathymetry database

For this study, high-resolution digital point bathymetry data were obtained from the Canadian Hydrographical Service for Dixon Entrance, Hecate Strait and Queen Charlotte Sound. The original bathymetry data were provided in geographic (*i.e.*, spherical) coordinates, giving ocean depth versus latitude and longitude. However, acoustic modelling transects, which are geodesic arcs, cannot be easily represented in geographic coordinates. For acoustic modelling on relatively small scales (maximum range $\sim$ 300 km for the current study) it is much more convenient to employ a planar "x/y" coordinate system. Using a locally flat coordinate system does not introduce significant error into the transmission loss calculations, on such small scales, provided an appropriate coordinate projection is selected.

For the current study, the point bathymetry data were reprojected onto a Universal Transverse Mercator (UTM) coordinate system[1] and resampled onto a regular grid. The UTM projection expresses geographic location in terms of an x/y Cartesian coordinate pair, referenced to a particular central meridian (*i.e.*, a line of constant longitude bisecting the globe). The scale distortion of the UTM projection is less than 0.1% within 300 km of

[1]The Transverse Mercator projection and its associated coordinate transformations are discussed in detail in the text by Snyder (1984).

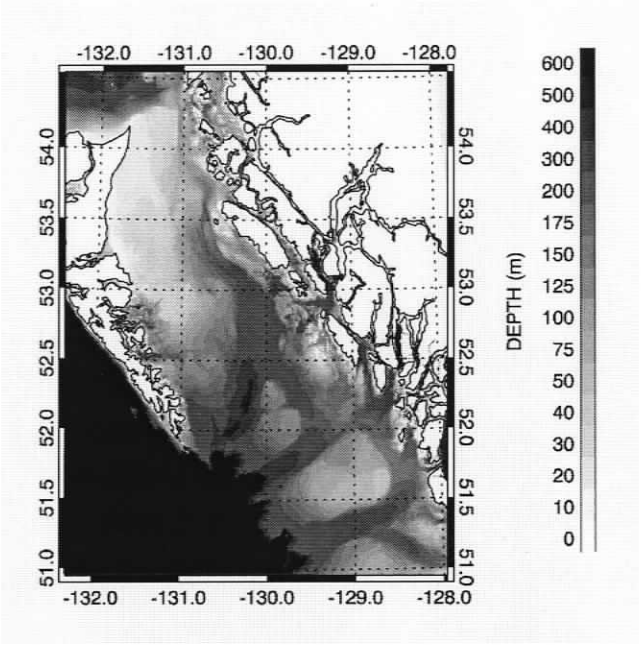

Figure 4.1: Grayscale contour map of Queen Charlotte Basin bathymetry grid.

the central meridian (Snyder, 1984, p. 58). For the current study, a custom UTM projection, with a central meridian of 130° W, was used for reprojecting the bathymetry data. To generate the bathymetry database, the bathymetry data were resampled onto onto a constant 100×100 metre UTM grid. Figure 4.1 shows a contour plot of the bathymetry grid for the Queen Charlotte Basin. Range/depth points for the acoustic modelling transects were sampled from the gridded bathymetry database.

4.2 Sound speed profiles and absorption

Representative sound speed profiles for the Queen Charlotte Basin were derived from a set of over 1300 CTD (Conductivity-Temperature-Depth) casts from Fisheries and Oceans Canada research cruises during 1982–1995. The extensive collection of temperature and salinity data was obtained from a CD-ROM report on the oceanography of the Queen Charlotte region published by Fisheries and Oceans Canada (Crawford, 2001). Temperature and salinity profiles were sorted by time of year and converted to sound speed using Coppens'

equation for the speed of sound in seawater (1981):

$$\begin{aligned} c(z,T,S) &= 1449.05+45.7t-5.21t^2-0.23t^3 \\ &\quad +(1.333-0.126t+0.009t^2)(S-35)+\Delta \qquad (4.1) \\ \Delta &= 16.3Z+0.18Z^2 \qquad (4.2) \\ Z &= z/1000\,(1-0.0026\cos 2\phi) \qquad (4.3) \\ t &= T/10 \qquad (4.4) \end{aligned}$$

where z is depth in metres, T is temperature in degrees Celcius, S is salinity in psu and ϕ is latitude.

Absorption of sound in seawater was computed according to the equation of Thorp (1967), which is appropriate for frequencies between 100 Hz and 3 kHz:

$$\beta = \frac{0.11f^2}{1+f^2} + \frac{44f^2}{4100+f^2} \qquad (4.5)$$

where f is in kHz and β has units of dB/km. Note that this expression for sound absorption in seawater depends only on frequency and is independent of temperature and salinity.

4.2.1 Principal component analysis

The large set of sound speed profile data exhibited substantial seasonal and diurnal variability. Thus, a statistical technique known as principal component analysis was used to extract representative profile shapes from the large collection of data. Briefly, principal component analysis is used to derive orthogonal modes of variability, called "empirical orthogonal functions" (EOF's), from a set of correlated data; decomposing the data in terms of the EOF's yields a set of derived variables, called "principal components". This technique is powerful because often only a few principal components are necessary to describe most of the observed variability in a dataset. Thus, the effect of principal component analysis is to reduce the dimensionality of a dataset from many real variables (*i.e.*, sound speed versus depth) to only a few derived variables (the principal components). An in-depth exposition on the topic of principal component analysis may be found in the text by Jolliffe (1986); only a brief overview of the relevant mathematics is presented here.

In general, we wish to apply principal component analysis to a dataset consisting of many realizations (*i.e.*, samples) of N correlated random variables — in this case, profiles of sound speed at N depth points:

$$\mathbf{c} = (c_1, c_2 \ldots c_N) \tag{4.6}$$

where $\mathbf{c}$ is the data vector of sound speed samples at N depth points. To derive a set of empirical orthogonal functions describing the variability of this dataset, the first step is to construct the data covariance matrix, V:

$$\mathsf{V}_{ij} = \langle (c_i - \mu_i)(c_j - \mu_j) \rangle \qquad i, j = 1 \ldots N \tag{4.7}$$

where $\langle \ldots \rangle$ denotes the expectation value and μ_i is the mean sound speed at depth i. The set of EOF's, $\mathbf{x}_i$ and their associated N eigenvalues, λ_i, are obtained by performing eigenvalue decomposition on the covariance matrix, V, such that

$$\mathsf{V}\mathbf{x}_i - \lambda_i \mathbf{x}_i = 0 \qquad i = 1 \ldots N \tag{4.8}$$

The EOF's with the largest eigenvalues describe the primary modes of variability of the data. If the EOF's are normalized such that $\|\mathbf{x}_i\| = 1$ then it may be shown that the eigenvalues λ_i correspond to the variance of each principal component (Jolliffe, 1986, §1.1). If the eigenvalues are ordered such that $\lambda_1 > \lambda_2 > \ldots \lambda_N$ then the percent-variance, p_i, of the dataset accounted for by the i^{th} derived variable is given by the expression (Jolliffe, 1986, §6.1.1)

$$p_i = 100 \frac{\sum_{j=1}^{i} \lambda_j}{\sum_{j=1}^{N} \lambda_j} \tag{4.9}$$

Finally, the projection of the data vector onto the EOF's gives the decomposition of the data in terms of the derived variables (*i.e.*, the principal components):

$$\widetilde{\mathbf{c}} = (\mathbf{c} - \mu)\mathsf{X}^T \tag{4.10}$$

where the $\mathbf{c}$ is the vector of sound speed profile data, $\mu = (\mu_1 \ldots \mu_N)$ is the mean sound speed vector, X is the matrix of EOF's and $\widetilde{\mathbf{c}}$ is the decomposition of the data in terms of

the derived variables.

Given the principal value decomposition for a large dataset, synthetic data vectors may be constructed from a weighted sum of the M most significant EOF's:

$$\mathbf{c}' = \mu + \sum_{i=1}^{M} a_i \mathbf{x}_i \tag{4.11}$$

where the a_i are the weighting coefficients, which are nothing more than the principal components. Suitable values for the weighting coefficients may be selected from the observed distribution of the principal components (*e.g.*, from a histogram) as determined from the decomposition of the original data in terms of the EOF's.

In order to apply principal component analysis, all of the sound speed profiles were resampled at identical depth intervals. Regular subdivisions of standard oceanographic depths up to 500 metres were used, yielding 26 sound speed sample points versus depth for each profile. The 26×26 covariance matrix was constructed from the resampled sound speed profiles and the EOF's were found by performing eigenvalue decomposition on this matrix. Finally, the principal components were determined by projecting the data onto the EOF's. Figure 4.2(a) shows a plot of the percent data variance accounted for by each principal component; one can see that the first PC accounts for 88.5% percent of the total variability of the sound speed profile data. A month-by-month scatter plot of the first PC is presented in Figure 4.2(b) showing the the seasonal variability of the shape of the sound speed profile in Queen Charlotte Basin.

Two representative profile shapes, shown in Figure 4.3, were derived based on the 95% range of observed values of the first principal component. These two profiles, which have been denoted "A" and "B" respectively, represent the limiting sound speed profile shapes observed in Queen Charlotte Basin. Profile A conditions are predominant in summer when solar heating generates a sound speed maximum at the sea surface. Profile B conditions, on the other hand, are predominant in winter, when cooling at the sea surface causes the opposite effect. Under profile A conditions, acoustic energy is refracted towards the sound speed minimum at the sea bottom, where lossy reflections from the seabed will tend to to scatter and attenuate acoustic energy. Conversely, under profile B conditions, the sound speed minimum near the sea surface (called a surface duct) will trap acoustic energy and transmit it to longer ranges.

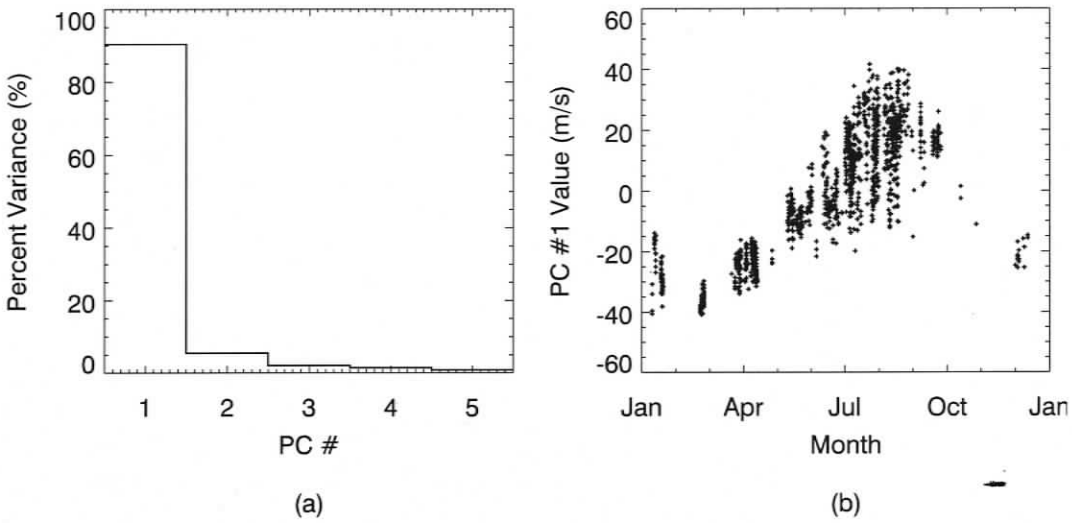

Figure 4.2: (a) Bar-plot of percent data variance versus principal component number. (b) Month-by-month scatter plot showing seasonal variability of first PC.

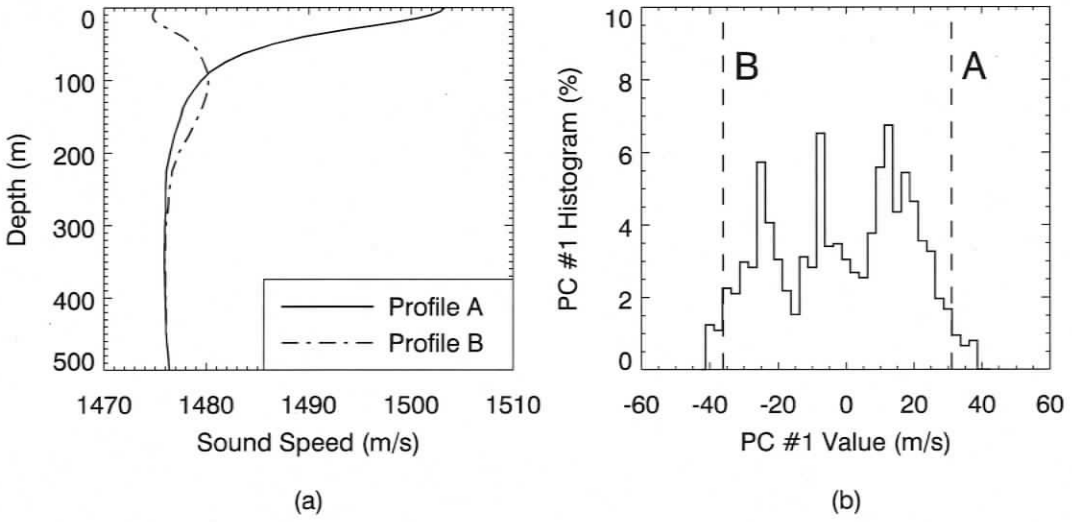

Figure 4.3: (a) Plot of limiting sound speed profiles, designated "A" and "B" respectively, employed for the transmission loss modelling. (b) Histogram showing the distribution of values of the first principal component. The dashed vertical lines, which bracket approximately 95% of the observed data, indicate the principal component values that were used to derive profile shapes A and B respectively.

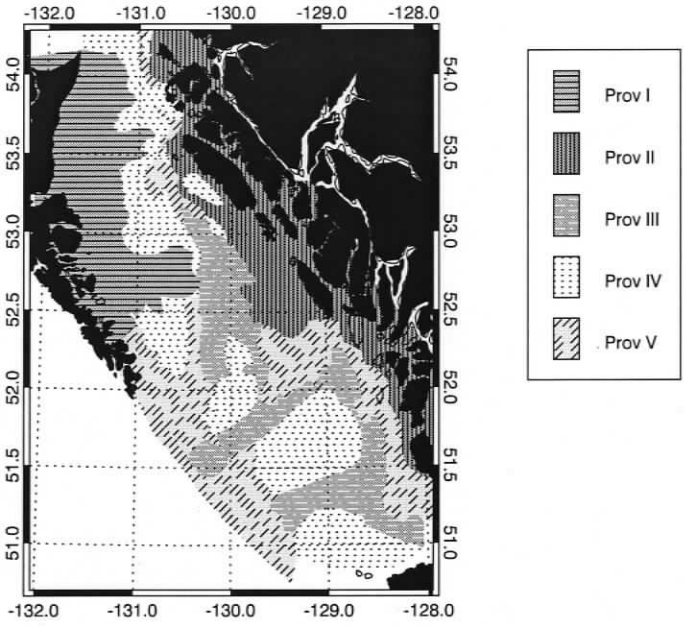

Figure 4.4: Map showing the surface coverage of the five geoacoustic provinces that were defined for Queen Charlotte Basin. Coverages were based on GSC surficial geology maps (Barrie et al., 1990).

4.3 Geoacoustic database

A geoacoustic map of the seabed for the entire Queen Charlotte Basin was required in order to carry out an acoustic propagation modelling study in this region. In the absence of direct geoacoustic measurements, it was necessary to estimate the acoustic properties of the seabed in Queen Charlotte Basin based on knowledge of the bottom geology. Extensive geological surveying and mapping work has been conducted in the Queen Charlotte Basin and the results of several surficial geology studies have been published. However, the Queen Charlotte Basin covers a vast area and the available geology and sediment thickness data are sparse. Thus, rather than seeking to replicate the detailed geological features of the seabed, a simplified geoacoustic database was created that divides the Queen Charlotte Basin into five unique geoacoustic provinces, shown in Figure 4.4. Each of the five geoacoustic provinces shares a common set of bottom parameters that were estimated based on knowledge of the bottom geology. The surface coverage of the five unique geoacoustic

provinces was based on surficial geology maps of the Queen Charlotte Basin published by the Geological Survey of Canada (Barrie et al., 1990).

The five geoacoustic provinces in Figure 4.4 roughly correspond to the surficial geology units of Barrie et al. (1990) as follows:

- Province I corresponds to the "Bedrock" unit from Barrie et al. (1990). This province, predominant on Dogfish Banks in Northwest Hecate Strait, is characterized by the surface expression of consolidated Tertiary sediments underlying the basin (*i.e.*, the Skonun and Masset Formations of (Barrie et al., 1991)).

- Province II corresponds to regions east of the basin where the bedrock is comprised of granite rock rather than consolidated sediments (Bornhold and Barrie, 1991). Strictly speaking, these regions are not part of the Queen Charlotte Basin proper, but they must be included to model acoustic propagation near the coast.

- Province III corresponds to the "Glaciomarine Muds" and "Queen Charlotte Muds" units of Barrie et al. (1990). The sediment layers in this province are characterized by thick silt and mud layers that have been deposited in the troughs of the basin.

- Province IV corresponds to the "Queen Charlotte Sands and Gravels" unit of Barrie et al. (1990). This province is characterized by sand and gravel surface deposits present in the shallow waters to the north of the basin, and on the banks to the south.

- Province V corresponds to the "Till" unit of Barrie et al. (1990). This province is characterized by a layer of glacial till deposited on top of the consolidated Tertiary sediments in the deeper waters of the basin.

The surface sediment layering in Queen Charlotte Basin is non-uniform in many places, and the thickness is variable. Furthermore, very little sediment thickness data are available and there have been no direct measurements of the acoustic properties of the surface materials. Thus, it was necessary to generalize the layering of bottom materials: each province was associated with a single representative stratified seabed model, comprised of horizontal layers of sediments and rock. Tables 4.1–4.5 show the seabed model associated with each geoacoustic province, along with the corresponding values for the five main geoacoustic parameters: c_p, c_s, ρ, α_p and α_s. The thicknesses of the material layers in each province

were based on interpreted Huntec cross-sections and sediment core data presented in Barrie and Bornhold (1989), Barrie et al. (1990) and Barrie et al. (1991).

For each geoacoustic province, vertical profiles of the acoustic properties of the material layers were estimated, based on representative values given in the extensive review article by Hamilton (1980). The literature sources for the acoustic properties of the material layers given in Tables 4.1–4.5 were as follows: "Sand" in provinces I and IV was taken to be "Fine sand" from Hamilton's article; "Mud" in province III was taken to be Hamilton's "Sand-silt-clay", based on the description of Glaciomarine Muds and Queen Charlotte Muds from Barrie et al. (1991, Fig. 2); "Till" in provinces II, III and V was taken to be Hamilton's "Sandy-silt", based on the description of Glacial Till from Barrie et al. (1991, Fig. 2); the acoustic properties of "Bedrock" (Skonun and Masset Formations) for provinces I, II, IV and V, were based on values suggested by N. R. Chapman (priv. comm.); and the acoustic properties of the "Granite" basement in province II were taken from Beebe and Holland (1986).

Table 4.1: Vertical geoacoustic parameter profiles for province I.

	PROV. I					
Material	z (m)	c_p (m/s)	ρ (g/cc)	α_p (dB/λ)	c_s (m/s)	α_s (dB/λ)
Sand	0	1715.1	1.941	0.429	52.8	0.697
	3	1743.6	1.941	0.436	62.4	0.824
	5	1757.1	1.941	0.439	71.0	0.938
Bedrock	5	2200.0	2.200	0.100	754.0	0.045
	100	2298.4	2.200	0.100	830.8	0.050
	200	2421.4	2.200	0.100	926.7	0.056

Table 4.2: Vertical geoacoustic parameter profiles for province II.

	PROV. II					
Material	z (m)	c_p (m/s)	ρ (g/cc)	α_p (dB/λ)	c_s (m/s)	α_s (dB/λ)
Till	0	1603.8	1.771	0.160	378.0	1.814
	3	1607.5	1.771	0.161	379.4	1.821
	5	1609.9	1.771	0.161	380.3	1.825
Granite	5	5500.0	2.600	0.050	2400.0	0.144
	500	6108.9	2.600	0.050	2665.7	0.160

Table 4.3: Vertical geoacoustic parameter profiles for province III.

	PROV. III					
Material	z (m)	c_p (m/s)	ρ (g/cc)	α_p (dB/λ)	c_s (m/s)	α_s (dB/λ)
Mud	0	1526.7	1.596	0.198	172.7	2.989
	2	1529.2	1.596	0.199	182.3	3.154
	5	1532.9	1.596	0.199	196.6	3.402
	8	1536.6	1.596	0.200	211.0	3.650
	10	1539.0	1.596	0.200	220.5	3.815
Till	10	1662.1	1.771	0.166	401.3	1.926
	25	1680.6	1.771	0.168	409.3	1.965
Bedrock	25	2200.0	2.200	0.100	754.0	0.045
	500	2784.3	2.200	0.100	1209.7	0.073

Table 4.4: Vertical geoacoustic parameter profiles for province IV.

	PROV. IV					
Material	z (m)	c_p (m/s)	ρ (g/cc)	α_p (dB/λ)	c_s (m/s)	α_s (dB/λ)
Sand	0	1700.3	1.941	0.425	52.4	0.692
	3	1728.6	1.941	0.432	55.9	0.738
	8	1754.2	1.941	0.439	69.0	0.910
	15	1770.8	1.941	0.443	82.5	1.089
	20	1778.5	1.941	0.445	90.1	1.190
Bedrock	20	2200.0	2.200	0.100	754.0	0.045
	100	2298.4	2.200	0.100	830.8	0.050

Table 4.5: Vertical geoacoustic parameter profiles for province V.

	PROV. V					
Material	z (m)	c_p (m/s)	ρ (g/cc)	α_p (dB/λ)	c_s (m/s)	α_s (dB/λ)
Till	0	1603.8	1.771	0.160	378.0	1.814
	5	1609.9	1.771	0.161	380.3	1.825
	10	1616.1	1.771	0.162	382.6	1.837
	12	1618.5	1.771	0.162	383.6	1.841
	15	1622.2	1.771	0.162	385.0	1.848
Bedrock	15	2200.0	2.200	0.100	754.0	0.045
	500	2796.6	2.200	0.100	1219.3	0.073

Chapter 5

Model setup and execution

This chapter describes the various steps that were involved in setting up and running the acoustic models for generating seismic survey noise level predictions in Queen Charlotte Basin. The first step was to design a realistic airgun survey scenario: simulated survey tracks were placed over regions of the basin with the highest potential for hydrocarbon deposits and several source locations along the track lines were selected for modelling. In addition, a representative airgun array design was selected, typical of array layouts employed by industry for oil and gas surveying. Once the seismic survey scenario was defined, noise level predictions were generated by carrying out the following five steps:

1. The far-field source signatures of the airgun array, modelled using AASM, were used to compute third-octave band source levels as a function of azimuth angle.

2. For each source location, bathymetry and geoacoustic data were extracted along densely spaced radial modelling transects covering the entire basin.

3. At each modelling frequency, convergence testing was used to determine the appropriate computation grid spacing (Δr and Δz) for CRAM.

4. The acoustic transmission loss model was run, in batch-fashion, for each source location to generate three-dimensional transmission loss grids.

5. The source level predictions of AASM were combined with transmission loss predictions from CRAM to generate three-dimensional received level grids.

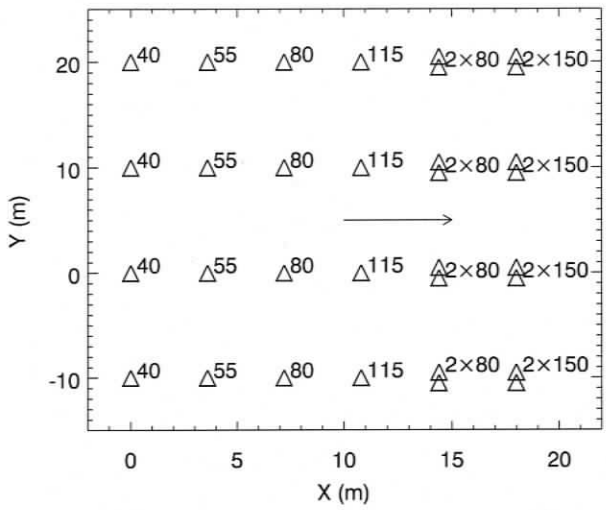

Figure 5.1: Plan view diagram of the airgun array employed for the current modelling study (total volume 3000 in^3). The volumes of individual guns are given in units of cubic inches. The arrow indicates the tow direction of the array.

5.1 Airgun array: layout and source signatures

A single airgun array design, representative of arrays employed by industry for oil and gas surveying, was chosen for modelling seismic survey noise in Queen Charlotte Basin. The airgun array was mid-sized and consisted of 32 airguns with a total volume of 3000 in^3. Airguns in the array ranged in volume from 40 in^3 to 150 in^3, and were arranged in four parallel, 20 metre long sub-arrays, spaced 10 metres apart. The firing pressure of the airguns was taken to be 2000 psi and the tow depth of the array was 6 metres. A plan-view diagram of the array layout is shown in Figure 5.1, indicating the positions and volumes of the individual airguns. Figure 5.2(a) shows the far-field signatures of the array in the vertical and broadside directions and Figure 5.2(b) shows the frequency spectrum of the far-field signatures.

A set of source signatures for the airgun array was computed with the `AASM` model, using the optimal model parameters given in Section 2.8. The set of airgun signatures were summed together with the appropriate phase delays, as described in Section 2.9, to

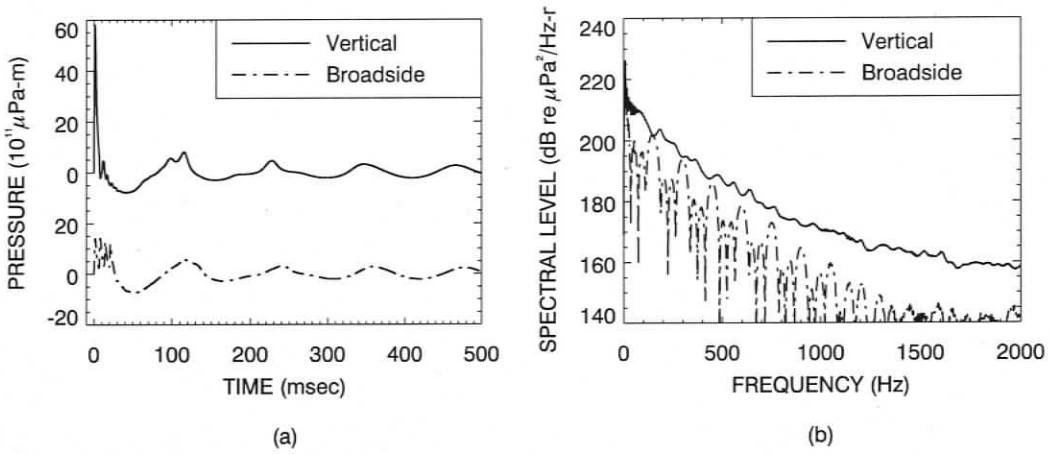

Figure 5.2: (a) Modelled far-field signature of the airgun array in both the vertical and horizontal (broadside) directions. (b) Spectra showing the frequency distribution of acoustic energy in the airgun array source signatures.

yield the far-field signature of the array. The acoustic energy of the far-field array signature was integrated inside third-octave pass bands, according to Equation 2.27, to compute the source level of the array as a function of frequency band, f_c, and propagation azimuth, θ:

$$SL = SL(f_c, \theta)$$

The horizontal directionality of the array was taken into account by using different source levels for different modelling azimuths; Figure 5.3 shows third-octave band plots of the source level of the array as a function of azimuth angle. The far-field source level of the array was combined with transmission loss computed using RAM to yield received level estimates.

Recall that the array signatures in Figure 5.3 are only applicable in the far-field, where the phase-difference due to the intergun spacing is taken to be small. Thus, we need to compute the distance to the far-field of the airgun array, according to Equation 2.28, to determine the minimum range of validity of the acoustic model predictions. The largest dimension of the airgun array in Figure 5.1 is the diagonal $L = 36$ m; therefore, the maximum near field range is 216 metres at the maximum modelling frequency of 1 kHz. It is clear from Equation 2.28 that the near-field range is smaller for lower frequencies. Beyond

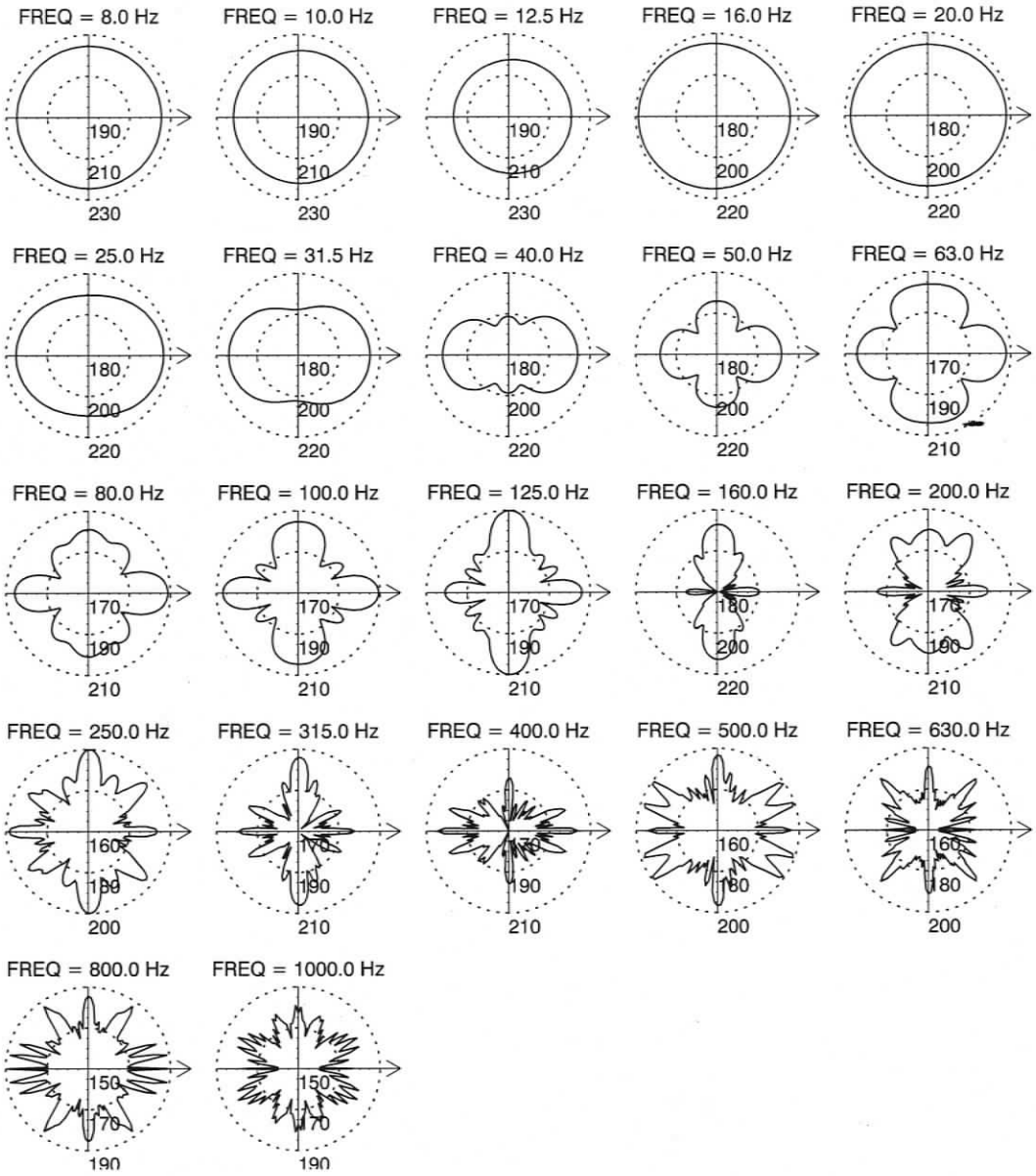

Figure 5.3: Airgun array source level horizontal directionality plots in third-octave bands. Arrows indicate the tow-direction of the array. Source levels are given in dB re μPa^2 · s@1m.

this range it may be assumed that the array radiates like a point source and can be treated as such for the purpose of propagation modelling.

The vertical directionality of the array was neglected in computing received level estimates because the acoustic propagation model RAM computes transmission loss for a point-like acoustic source (*i.e.*, a monopole), which has no intrinsic directionality. Instead, the horizontally propagating source level of the array was used, so that $\phi = 0$. Thus, it was implicitly assumed that acoustic energy propagates from the array primarily in the horizontal direction. This assumption is valid away from the source, where the acoustic field is dominated by trapped, propagating modes; these modes have low grazing angles that are less than the critical angle and close to the horizontal.

The acoustic propagation model RAM computes acoustic transmission loss for harmonic (*i.e.*, narrow-band) acoustic sources. However, airguns are broadband acoustic sources that emit energy over a wide frequency range from under 10 Hz to over 1 kHz. Thus, it was necessary to execute the propagation model over a range of frequencies, spanning the emission bandwidth of the airgun array source. True time-domain broadband modelling, using Fourier synthesis, requires acoustic field calculations at hundreds of discrete frequencies and is far too computationally intensive for a basin scale study. Instead, an energy-based approach was employed for the current study in which propagation loss was modelled in third-octave bands.

5.2 Source locations

For the transmission loss modelling, source locations were positioned along two simulated survey track lines, one running along the axis of the basin in the NNW–SSE direction and the other running across the basin in the NE–SW direction; these two track lines were designated "NS" and "EW" respectively. The two track lines traverse zones of the basin that have a high potential for oil and gas deposits (Whiticar et al., 2003, p. 102) and intersect at the location of the Sockeye B10 exploratory well. Cores from the Sockeye B10 well, drilled by Shell Canada Ltd. in 1968, showed oil stains, indicating the likely presence of hydrocarbon deposits at this location. Table 5.1 lists the coordinates and designations of the source locations, along with the array heading and water depth at each position. Each source position has been assigned a unique designation, except for the intersection

Table 5.1: List of geographic coordinates, array heading and water depth at each source location. Locations EWL03 and NSL03 are at the same position but have different array headings. Note that array headings are given in degrees counter clockwise from UTM easting (i.e., in the Cartesian sense) and are not north-referenced.

Location	Lon. (°)	Lat. (°)	Heading (°)	Depth (m)
EWL01	-130.579	53.073	42.8	115.9
EWL02	-130.796	52.946	42.8	48.8
EWL03	-131.012	52.819	42.8	32.9
NSL01	-131.339	53.315	108.5	27.3
NSL02	-131.178	53.067	108.5	37.8
NSL03	-131.012	52.819	108.5	32.9
NSL04	-130.903	52.615	108.5	96.0
NSL05	-130.794	52.411	108.5	108.4
NSL06	-130.645	52.174	108.5	192.0

of the track lines, which has two designations: NSL03 and EWL03. This is to distinguish between the two cases where the airgun array is aligned along the two different track lines. Figure 5.4 shows a map of the survey track lines, with the source positions superimposed.

5.3 Convergence testing

A series of convergence tests were performed in order to determine the appropriate range and depth resolution for CRAM's computation grid at each third-octave band frequency. Because RAM solves the acoustic field equation on a discrete range and depth grid, the range and depth intervals, Δr and Δz, must be sufficiently small to achieve a numerically convergent solution at each frequency. The size of Δr and Δz depends on both the wavelength of sound and on the environment being modelled. Smaller vertical step sizes are required when the stratification of the water and seabed are complex. Smaller horizontal step sizes are required when the environment is strongly range dependent. Thus, for a particular problem, appropriate values for Δr and Δz must be determined through rigorous convergence testing.

When using the parabolic equation method, an absorbing "sponge" layer must be included at the lower boundary of the modelling grid to prevent vertically travelling acoustic

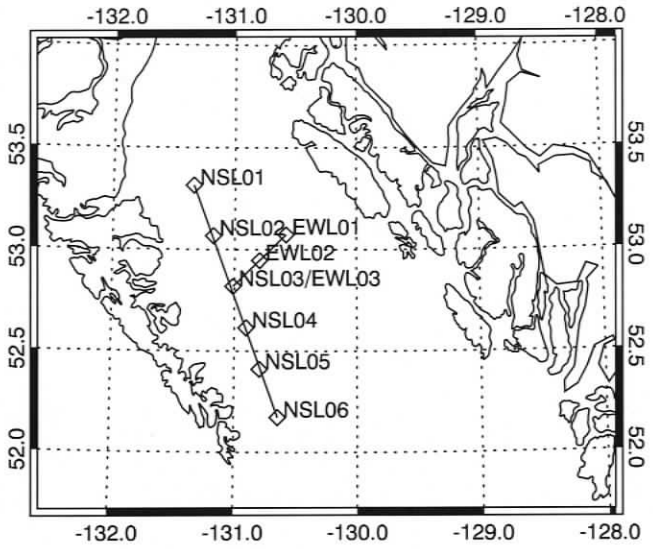

Figure 5.4: Map of simulated survey track lines and designated source locations.

energy from being artificially reflected back into the water column. Physically, acoustic energy travelling in the vertical direction is lost into the sub-bottom; however, when solving the acoustic field equation on a finite grid this energy must be artificially removed using an absorbing layer at the grid bottom. The size of this absorbing layer and the vertical extent of the grid both depend on the acoustic frequency. Thus, three more important modelling parameters that must be determined through convergence testing are the maximum grid depth, $z_{\max}$, the absorbing layer depth, z_α, and the vertical P-wave attenuation gradient in the absorbing layer, $d\alpha/dz$.

For the current study, convergence testing was performed along a single representative modelling transect, extending 300 km southeast from the NS03 source location. Bathymetry along this transect varied from approximately 30 metres depth to 500 metres depth. Model convergence was tested for each third-octave band frequency by varying Δr, Δz, $z_{\max}$ and z_α and comparing the resulting transmission loss for a fixed receiver depth of 10 metres. The final grid parameters for each third-octave band frequency, as determined from the battery of convergence tests, are shown in Table 5.2. The number of terms in the Padé series expansion of the PE operator was set to $n = 8$ for all frequencies.

Table 5.2: RAM solution grid parameters as determined by convergence testing along a single 300 km transect. Range and depth intervals are Δr and Δz, maximum vertical grid size is $z_{\max}$, absorbing layer depth is z_α and vertical gradient of attenuation in absorbing layer is $d\alpha/dz$.

Freq. (Hz)	Δr (m)	Δz (m)	$z_{\max}$ (m)	z_α (m)	$d\alpha/dz$ (dB/λ/m)
8	50	2.500	1000	200.0	0.020
10	50	2.500	1000	200.0	0.020
12.5	50	1.250	900	150.0	0.050
16	50	1.250	900	150.0	0.050
20	50	1.250	900	150.0	0.050
25	50	1.250	900	100.0	0.100
31.5	50	1.250	800	100.0	0.100
40	50	1.000	800	100.0	0.100
50	50	1.000	700	50.0	0.200
63	50	1.000	700	50.0	0.200
80	50	1.000	700	50.0	0.200
100	50	0.500	700	50.0	0.200
125	50	0.500	700	50.0	0.200
160	50	0.500	700	50.0	0.200
200	25	0.250	700	50.0	0.200
250	25	0.250	700	50.0	0.200
315	25	0.250	700	50.0	0.200
400	20	0.250	700	50.0	0.200
500	10	0.125	700	50.0	0.200
630	10	0.125	700	50.0	0.200
800	10	0.125	700	50.0	0.100
1000	10	0.125	700	50.0	0.100

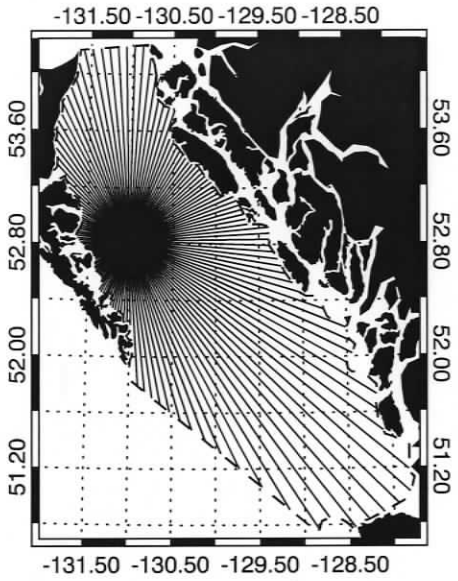

Figure 5.5: Map showing the coverage of the radial modelling transects for the EWL03 source location. The dashed lines indicate the boundary of the modelling area.

5.4 Transmission loss modelling

For each source location, acoustic transmission loss was computed along 144 evenly spaced radial transects. The modelling transects covered a full 360° of arc and extended from the source position to the limits of the Queen Charlotte Basin, as shown in Figure 5.5. Bathymetry points and geoacoustic profiles were extracted from the environmental databases at 50 metre intervals along the modelling transects. In addition, each source location was modelled twice, using each of the two sound limiting sound speed profiles shapes discussed in Section 4.2.

For each transect, acoustic transmission loss was modelled at 22 discrete third-octave band centre frequencies, from 8 Hz to 1 kHz. Since RAM does not directly account for sound attenuation in seawater, a range-dependent absorption factor (βr) was added to the transmission loss in each third-octave band according to Equation 4.5. Band pressure levels were then computed by combining transmission loss with third-octave band airgun array source levels, yielding received level as a function of range, depth, azimuth and frequency

band:

$$RL(f_c, r, z, \theta) = SL(f_c, \theta) - TL(f_c, r, z) - \beta(f_c)r \tag{5.1}$$

Broadband received levels were computed by summing together third-octave received band levels over frequency:

$$RL(r, z, \theta) = \sum_{f_c} 10^{RL(f_c, r, z, \theta)/10} \tag{5.2}$$

The sound level grids from the model were subsampled at a resolution of 5 metres in depth and 50 metres in range at all frequencies.

Four programs were written to execute each step of the acoustic propagation modelling: `JOBSETUP`, `SCRAMBLE`, `RLGRID` and `RLSUM`. The first program, `JOBSETUP`, was used to extract physical environmental data from the bathymetry and geoacoustic databases and to write a "job" file containing formatted input for `CRAM`. The second program, `SCRAMBLE` (Subroutine `CRAM` Batch Line Execution), was used to batch-execute `CRAM` at each source location, for all 22 frequencies and 144 transects, and to write the resulting three dimensional, frequency dependent transmission loss grids to a binary formatted output file. The third program, `RLGRID`, was used to combine the transmission loss grids with the airgun array source levels, in third-octave bands, to generate three-dimensional grids of frequency dependent received levels (*c.f.*, Equation 5.1). Finally, the fourth program, `RLSUM`, was used to sum the third-octave band received levels to generate three-dimensional grids of broadband received levels.

The transmission loss models were executed on a desktop workstation with a single 3.0 GHz Pentium 4 CPU running the Linux operating system. The Fortran code was compiled using the Absoft Fortran 77 compiler (version 8.1) with standard "level 1" optimizations. The transmission loss calcuation times for the different model scenarios (144 radials, 22 frequencies each) varied from 14.2 hours to 16.1 hours of CPU time. Real calcuation times were slightly longer than the CPU times since Linux is a time sharing (*i.e.*, multiuser) system.

Chapter 6

Model results

RAM was executed at eight unique source locations, for both the A and B sound speed profile shapes, yielding a total of 16 transmission loss grids and 18 different modelling scenarios (two different array orientations were used at the NSL03 source location). The transmission loss grids were combined with the directional source levels for the airgun array, as described in Section 5.4, to yield received sound levels as a function of receiver position:

$$RL = RL(f_c, r, z, \theta)$$

This chapter presents figures, maps and analysis showing the received noise levels predicted by the propagation modelling for each source location.

The received level grids presented in this chapter may be used for predicting the sound exposure of marine mammals and fish in the vicinity of the airgun survey. However, when considering the effects of sound exposure on marine mammals and fish, it is very important to be aware of how exactly quoted sound levels have been measured. As mentioned in Section 5.4, this study has employed an energy-based acoustic modelling approach, which is appropriate for impulsive noise sources such as airgun arrays; a more in-depth discussion of impulsive sound level metrics is provided in Appendix A. For interpreting the results presented in this chapter the reader should note that *received level values quoted here are given in terms of energy flux density (EFD)*[1] *or, equivalently, in terms of sound pressure*

[1] Energy flux density — which is the integral of square pressure — is also known as sound exposure level (SEL). See Appendix A for a more detailed discussion.

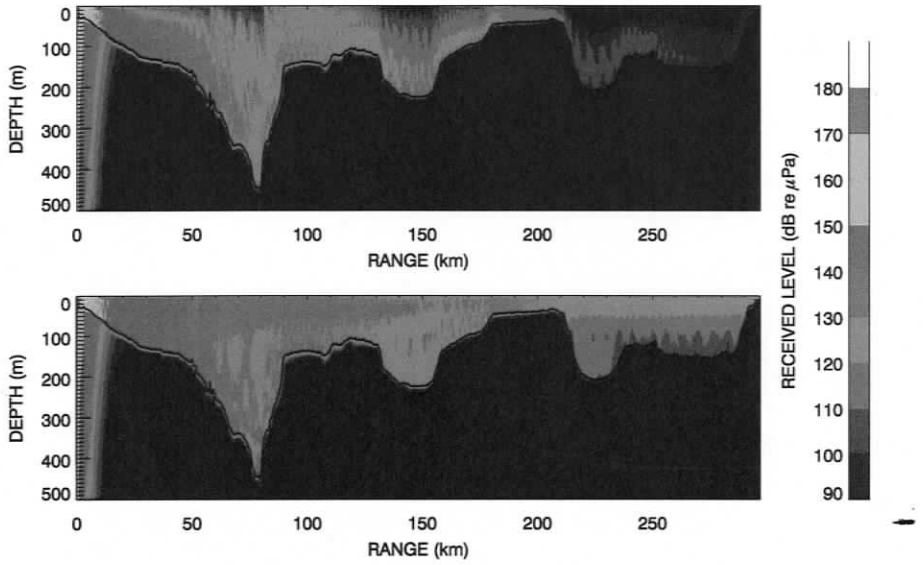

Figure 6.1: Broadband received level cross-sections, in range and depth, for the EWL03 source location. Received level plots are for the $\theta = 315°$ modelling azimuth. Both profile A (top) and profile B (bottom) conditions are shown.

level (SPL) over a 1 second time window.

6.1 Range/depth cross sections

Figure 6.1 shows an example of two range/depth received level cross-sections for the EWL03 source location, showing the difference in distribution of sound energy in the water column under profile A (down-refracting) and profile B (surface-duct) conditions. Both cross-sections are for the same SW-oriented modelling azimuth (315° clockwise from UTM Easting). From the figure, one can see that under profile A conditions the acoustic energy is refracted toward the seabed and the maximum sound levels are encountered near the sea-bottom. Furthermore, lossy reflections at the seabed result in much higher transmission loss at longer ranges, under profile A conditions. Conversely, under profile B conditions, the acoustic energy is trapped in the surface duct and the maximum sound levels are encountered near the sea-surface. As well, long-range transmission loss is lower under profile B conditions since sound trapped in the surface duct propagates to longer range.

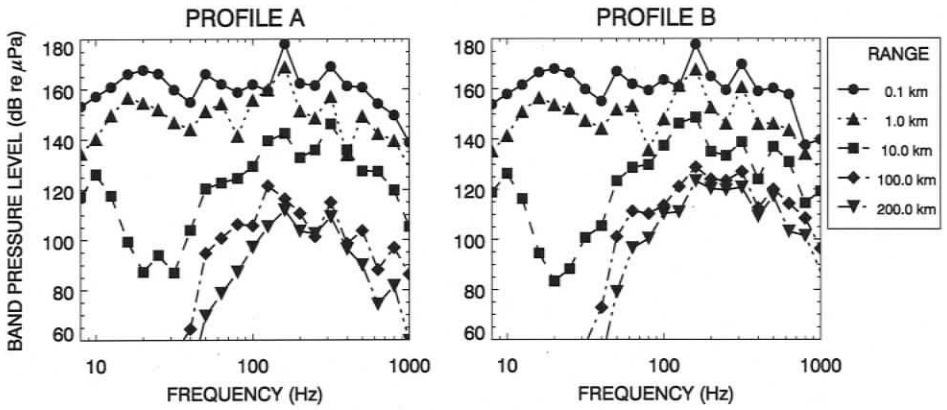

Figure 6.2: Frequency evolution of the seismic pulse versus range along the SE oriented track line of Figure 6.1. Two plots are shown, one for profile A (left) and one for profile B (right). The receiver depth is 25 metres.

Figure 6.2 shows the frequency evolution of the seismic pulse, at 25 metres depth, along the profile A and profile B cross-sections of Figure 6.1. One can see from the figure that maximum received levels occur between 100 Hz and 200 Hz, and that low frequencies, below 50 Hz, are rapidly attenuated with range. The differences in the band levels between the two profiles are most evident at long range, where the difference in received levels is greater than 20 dB at 200 km distance from the source.

6.2 Sound level contour maps

The fan of radials from each source position was combined to generate contours of the received sound level; geographic contour maps of the received sound levels, for all 18 modelling scenarios, are shown in Figures 6.3 through 6.11. The effect of the array directionality on the shape of the received level contours is immediately apparent — lobes of increased sound intensity clearly emanate from the broadsides of the array (*i.e.*, in the direction perpendicular to the survey tracks of Figure 5.4). As well, one can see that received levels are much lower in the shallow waters of Dogfish banks, to the north of the basin. This is because low frequency sounds, which contain most of the acoustic energy from the airgun array, propagate as highly attenuated leaky modes in shallow water and are rapidly

absorbed into the bottom. Note that, in order to represent the data in two dimensions, the received level at each geographic position (r, θ) was taken to be the maximum received level over depth, z. This approach is conservative, since it makes no assumption as to what depth a marine mammal or fish may be found in the water column.

6.3 Received level radii

A more succinct summary of the modelling results is presented in Figure 6.12, which shows a bar graph of the total ensonified area, from 180 dB to 90 dB in 10 dB increments, for all 18 modelling scenarios. Two bars are shown for each source location, one each for the down-refracting and surface-duct sound speed profile shapes (A and B, respectively). The length of each bar is proportional to the area enclosed by the corresponding received level isopleth. Note that the total area of the basin imposes an upper limit on the length of the bars in Figure 6.12. Areas are given in units of square kilometres, as shown on the left hand axis of the plot. Since areas can be difficult to visualize, the radius of a circle with the same area (*i.e.*, $r = \sqrt{A/\pi}$) is shown on the right hand axis in units of kilometres. This "equivalent radius" can be also thought of as a mean contour radius, averaged over azimuth angle.

Examining Figure 6.12, one can see that the area of the 180 dB and 170 dB received level isopleths is greater when the source is located where water depths are shallower (*c.f.* Table 5.1). This is because, in an ocean waveguide, the transition range between stronger spherical spreading loss ($TL \sim 20\log r$) and weaker cylindrical spreading loss ($TL \sim 10\log r$) is proportional to the water depth. In other words, in shallower water depths, critical angle reflection of sound from the seabed occurs at a shorter distance from the source and so more acoustic energy is concentrated in the water column. Thus, at ranges less than a few kilometres, received levels from the airgun array are more intense in shallower water.

At ranges beyond 10 km the shape of the sound speed profile dominates the trend in received levels. Under profile A conditions, sound is refracted down towards the seabed and since the seabed (which is elastic and sloping) is an imperfect reflector there is an increasing attenuation of the acoustic intensity with range. Under profile B conditions, on the other hand, sound is trapped in a surface duct and is free from bottom interactions — therefore it propagates to much greater distances. This effect is quite pronounced at ranges approaching 100 km, where the difference in received level is 20 dB or more between profile A and profile B conditions.

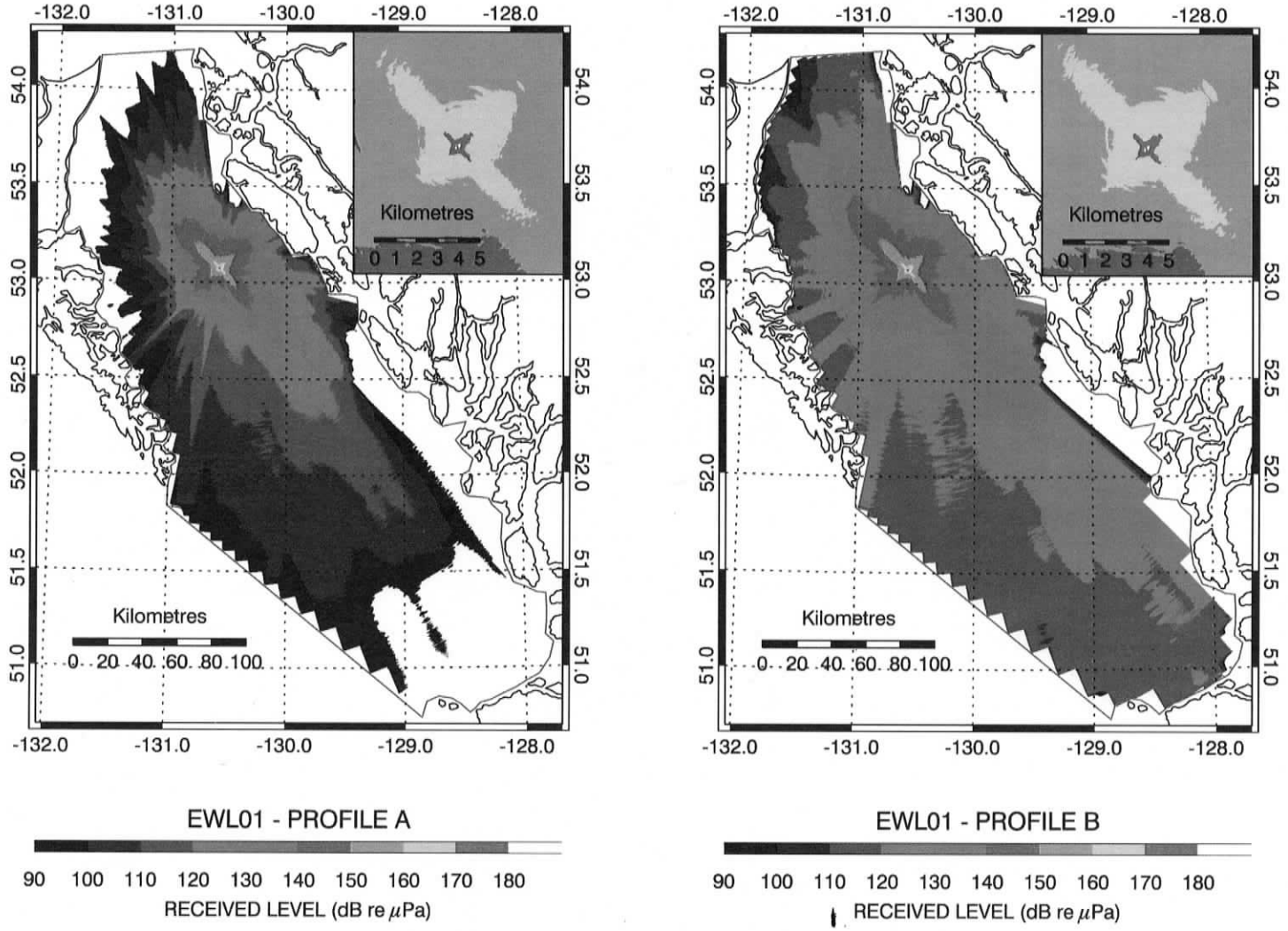

Figure 6.3: Noise level contour plots for the EWL01 source location. Inset shows magnified contours within 10 km range of the airgun array.

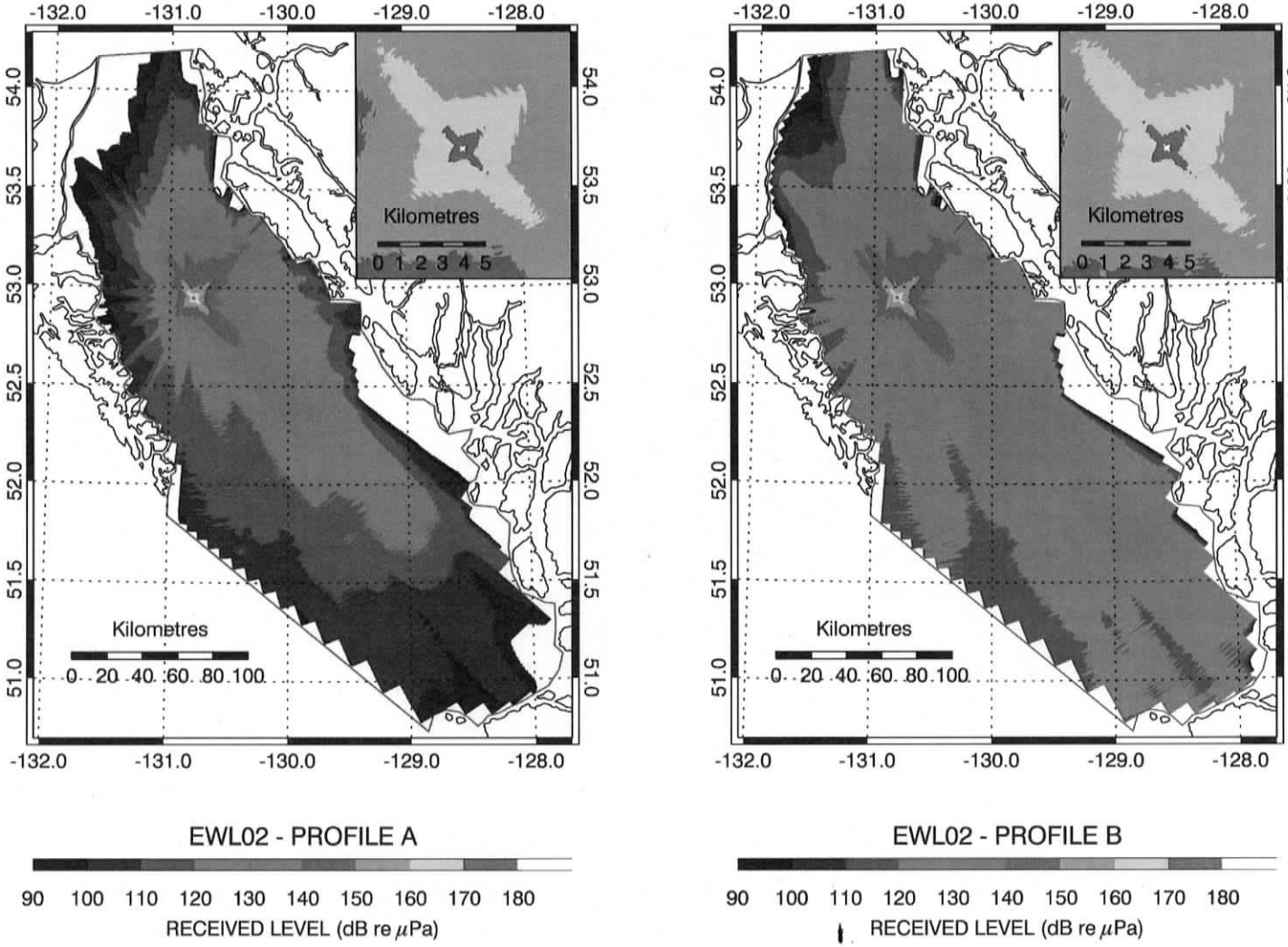

Figure 6.4: Noise level contour plots for the EWL02 source location. Inset shows magnified contours within 10 km range of the airgun array.

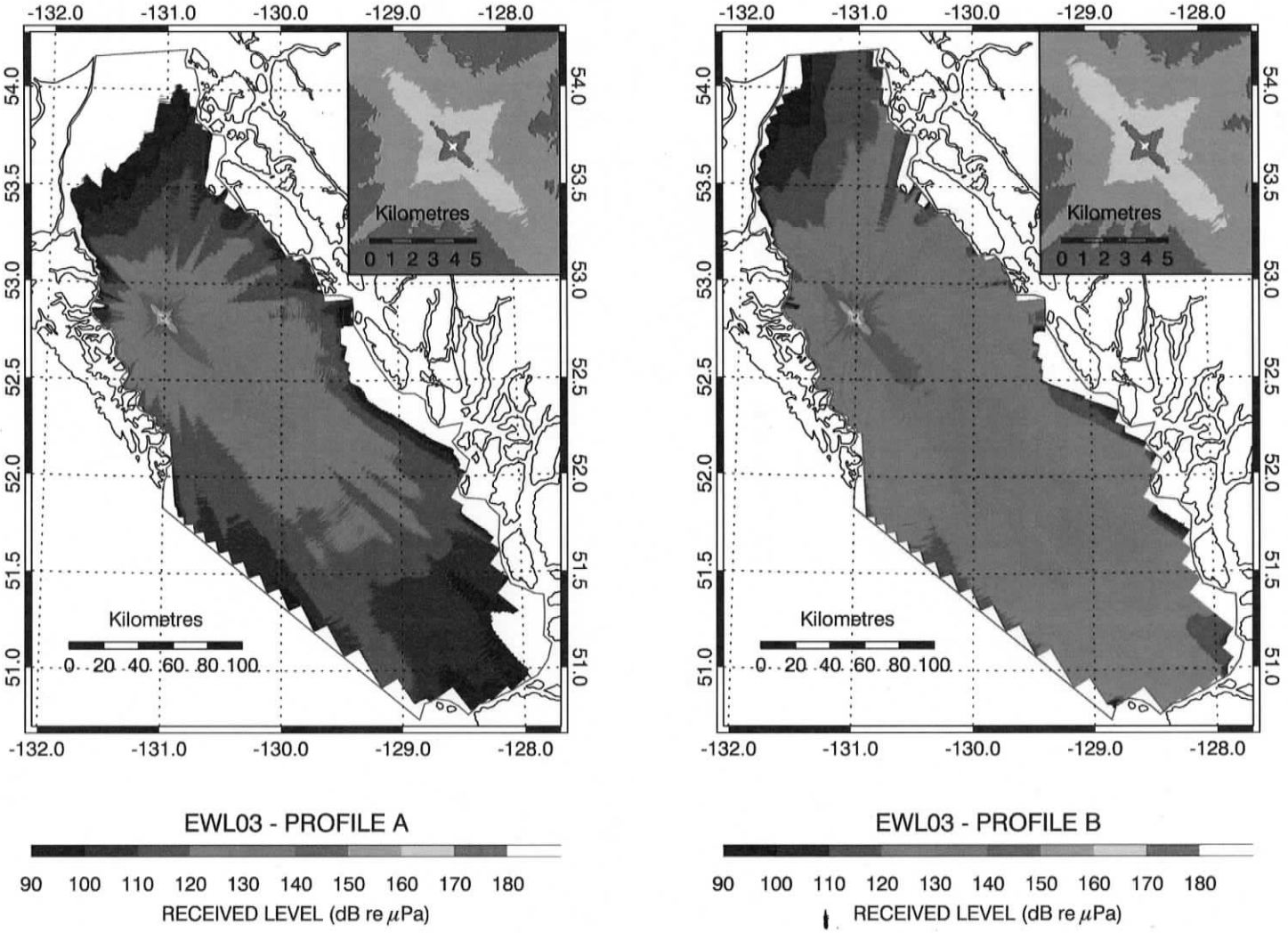

Figure 6.5: Noise level contour plots for the EWL03 source location. Inset shows magnified contours within 10 km range of the airgun array.

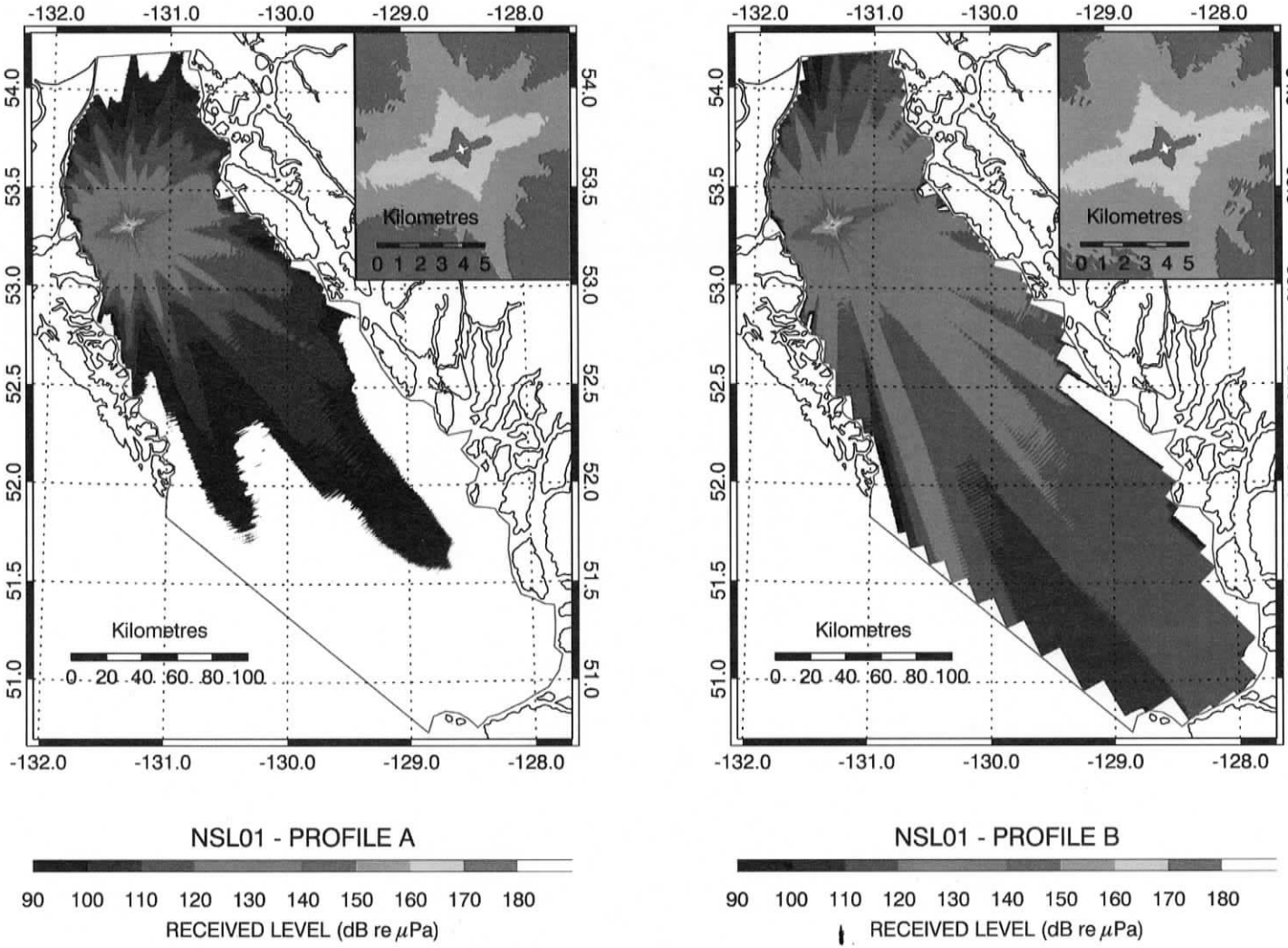

Figure 6.6: Noise level contour plots for the NSL01 source location. Inset shows magnified contours within 10 km range of the airgun array.

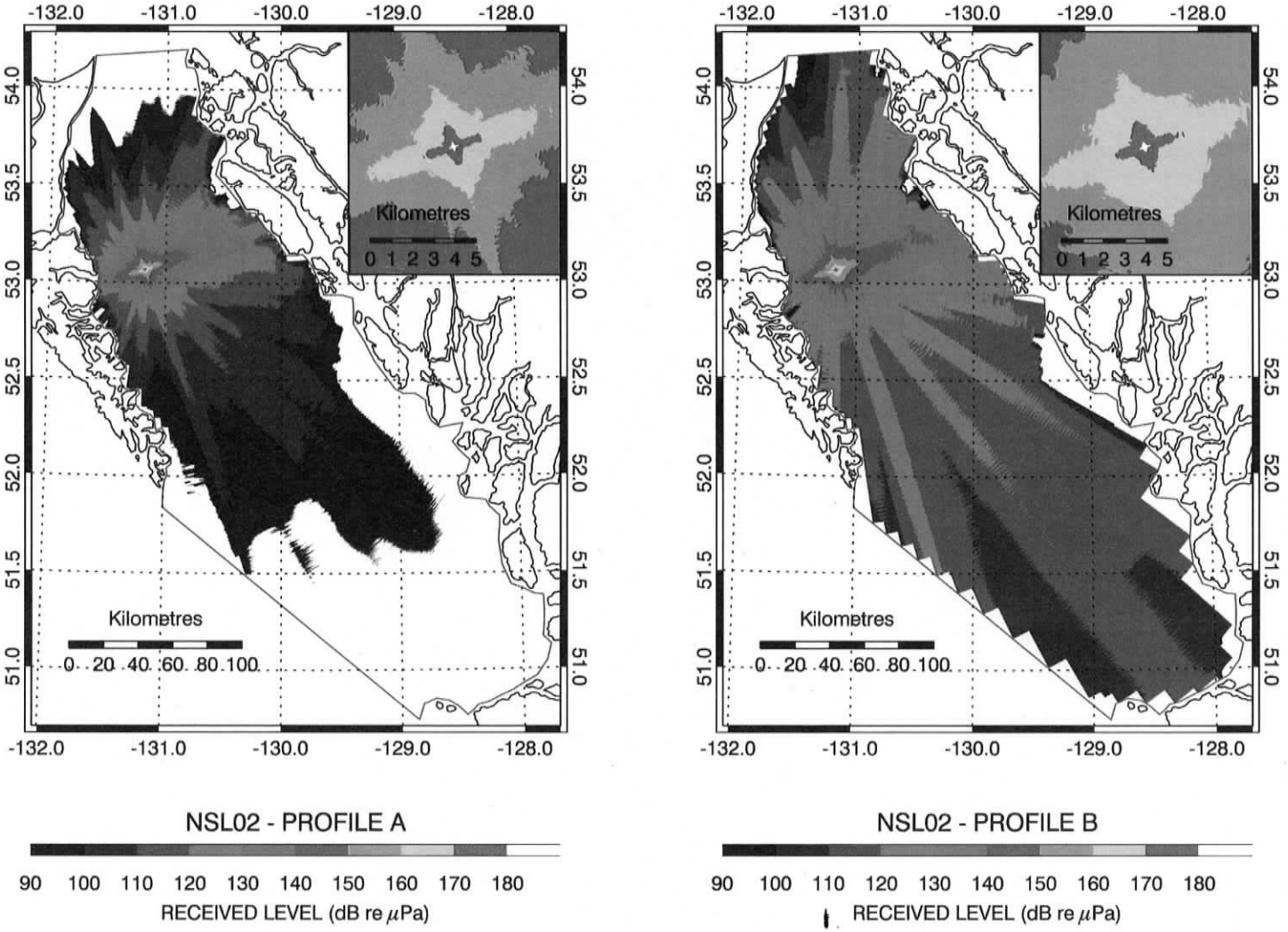

Figure 6.7: Noise level contour plots for the NSL02 source location. Inset shows magnified contours within 10 km range of the airgun array.

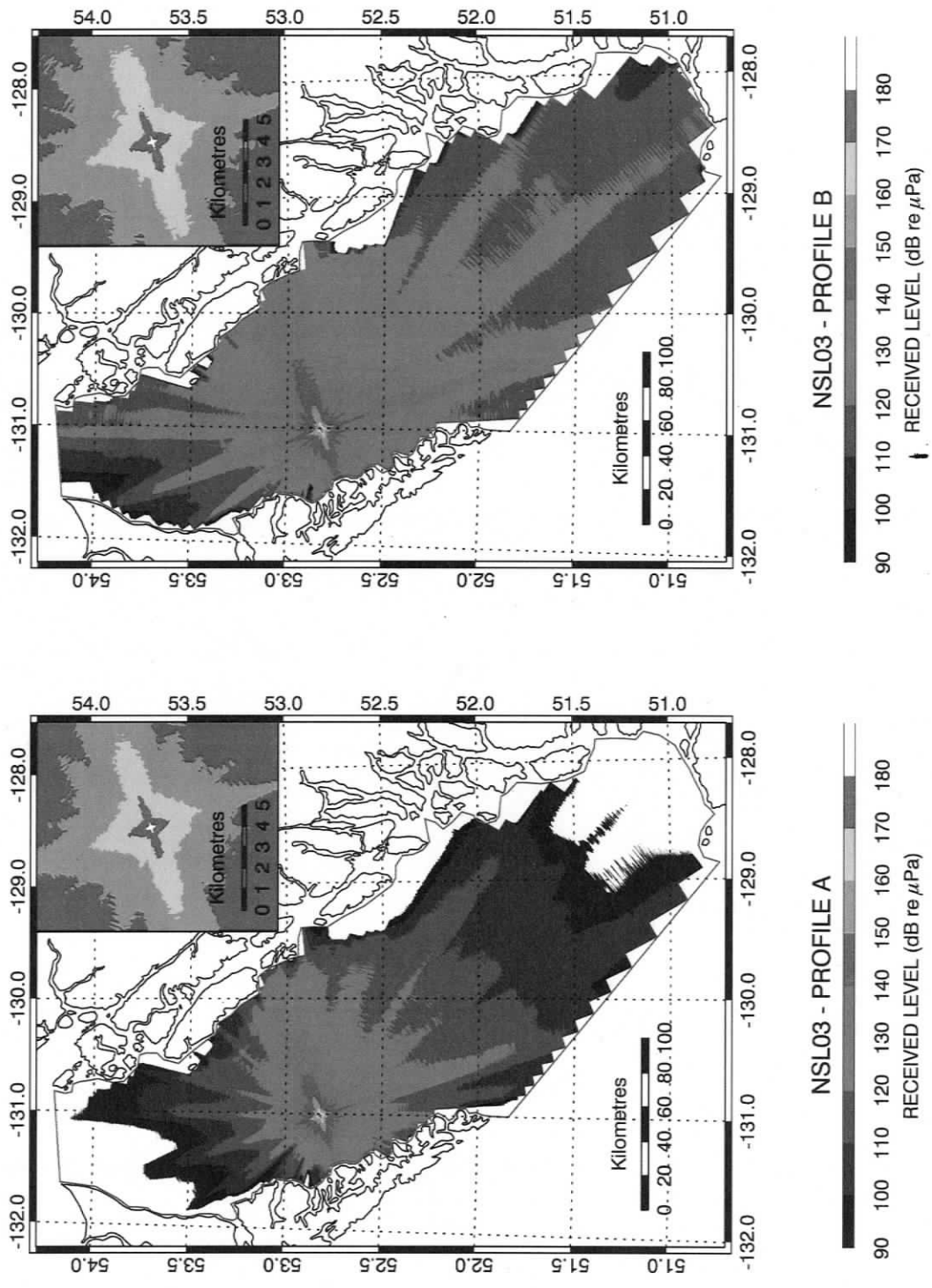

Figure 6.8: Noise level contour plots for the NSL03 source location. Inset shows magnified contours within 10 km range of the airgun array.

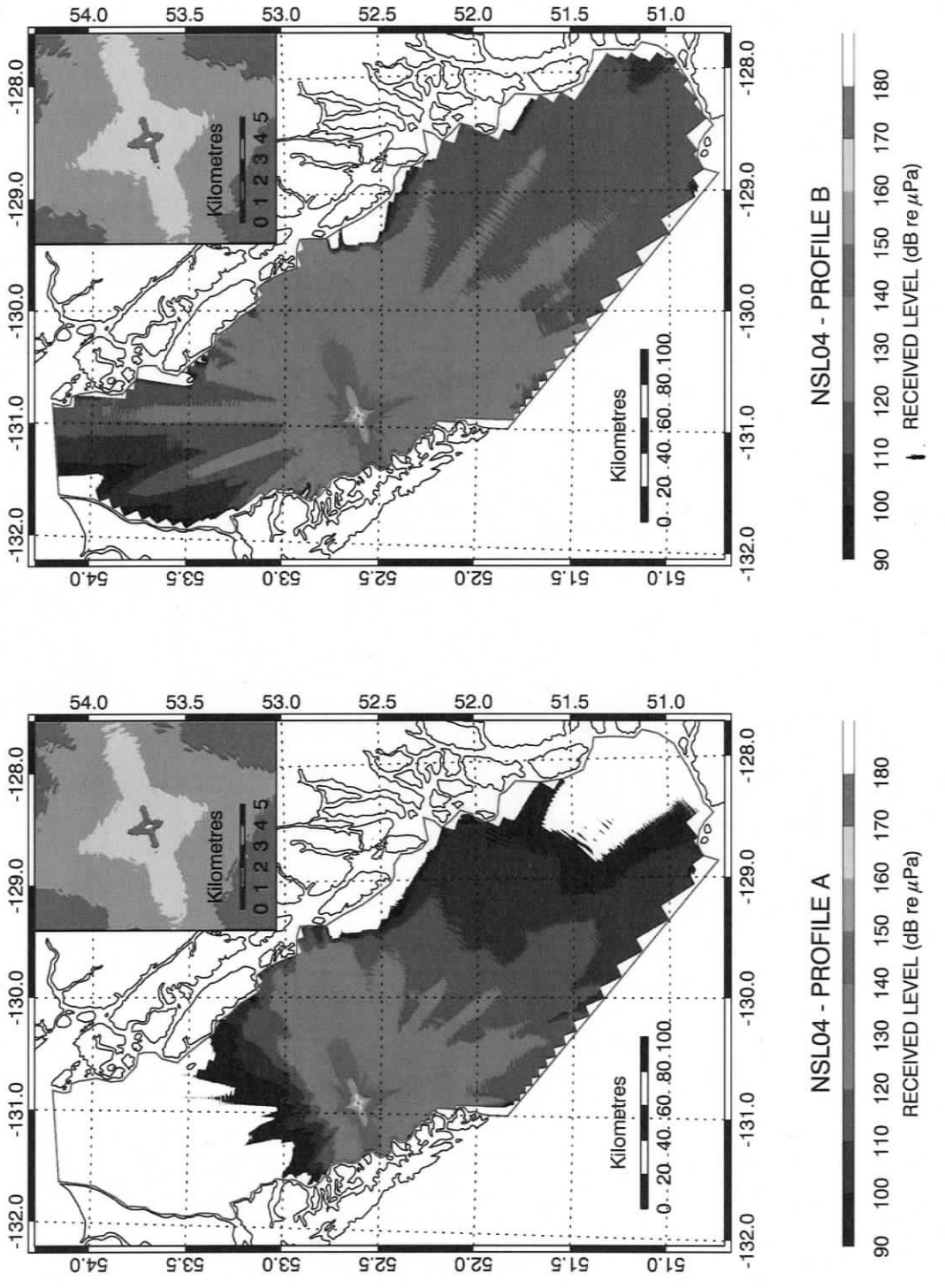

Figure 6.9: Noise level contour plots for the NSL04 source location. Inset shows magnified contours within 10 km range of the airgun array.

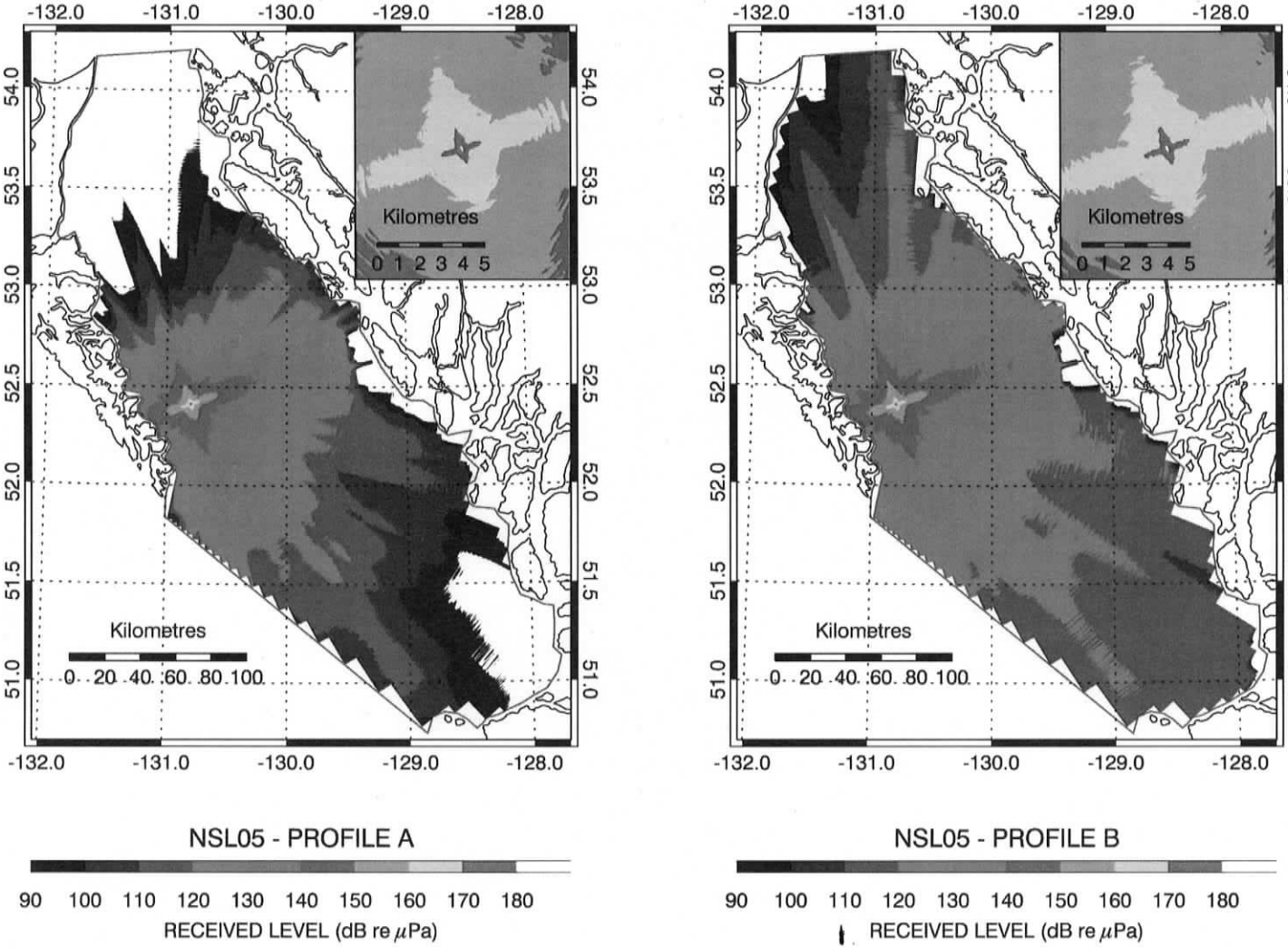

Figure 6.10: Noise level contour plots for the NSL05 source location. Inset shows magnified contours within 10 km range of the airgun array.

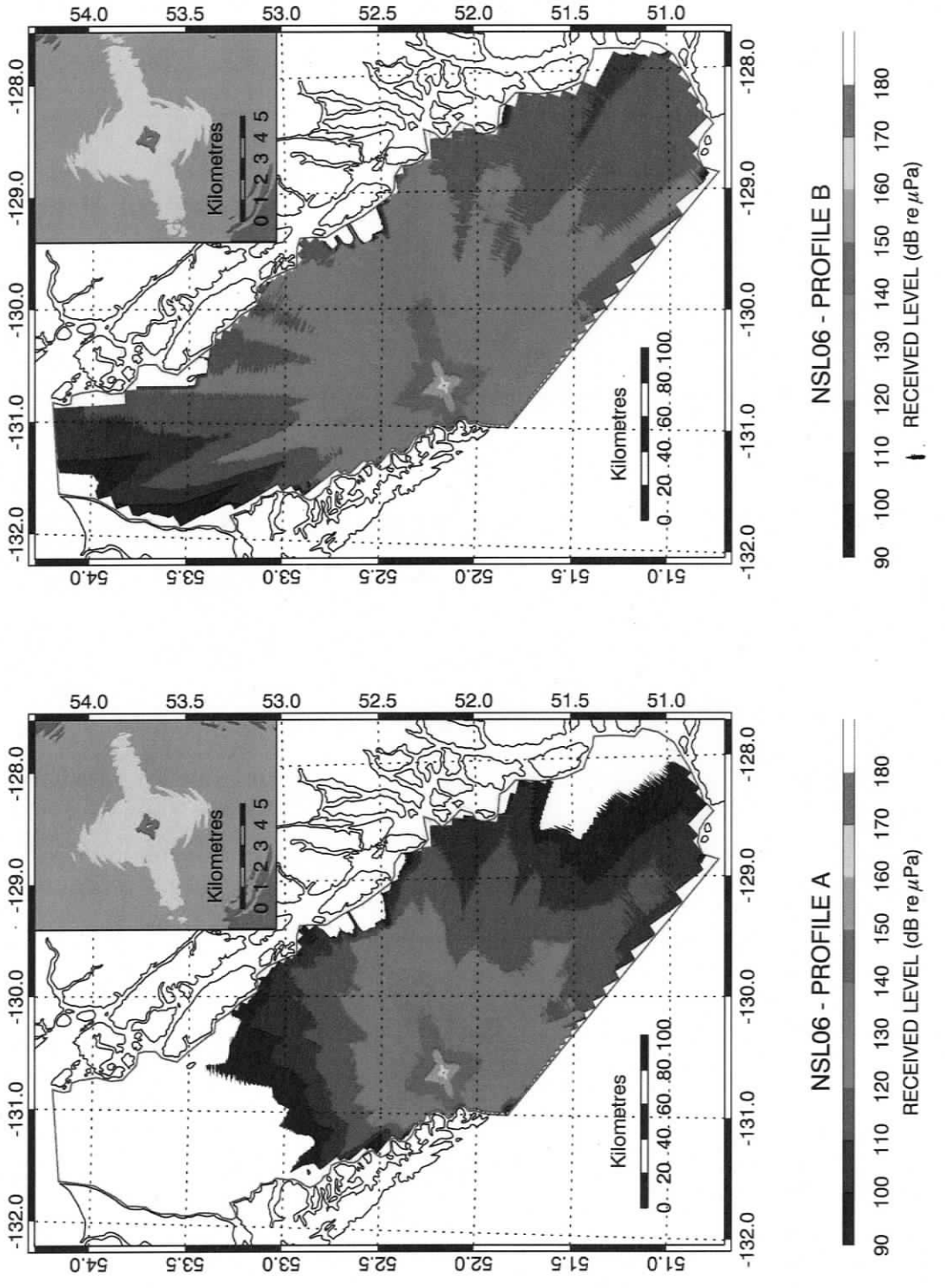

Figure 6.11: Noise level contour plots for the NSL06 source location. Inset shows magnified contours within 10 km range of the airgun array.

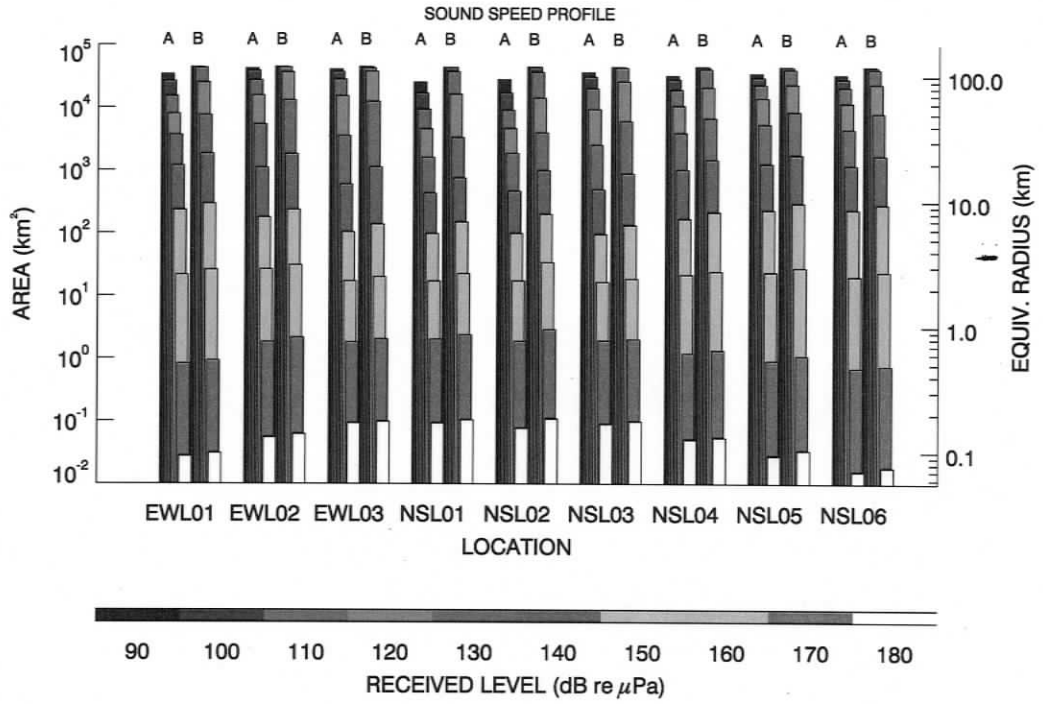

Figure 6.12: Bar plots of total area ensonified between 180 dB and 90 dB for all modelling scenarios considered in the current study. Two bars are presented for each source location, corresponding to the two sound speed profile shapes A and B. The total area of each sound level contour, in square kilometres is indicated on the left hand axis; the right-hand axis shows the "equivalent radius", in kilometres, of a circle with the same total area.

Chapter 7

Discussion and conclusions

This chapter discusses the modelling results from the previous chapter, both with regards to the effects of airgun survey noise on marine mammals and also with regards to possible sources of error (and possible improvements) in the modelling methodology. While it is not a goal of this dissertation to provide an assessment of the potential effects of airgun survey noise on marine mammals in the Queen Charlotte Basin, received level predictions are compared with regulatory "safety-ranges" as well as threshold levels from the literature that have been observed to cause behavioural reactions and shifts in hearing thresholds in marine mammals. In addition, this chapter discusses limitations in the accuracy of the model predictions, which are caused by uncertainty in the available environmental data and also by limitations in the propagation model itself. Finally, the chapter's conclusion summarizes the methodologies developed in this thesis dissertation and presents the key findings of the modelling study.

7.1 Discussion: airgun noise and marine mammals

The potential impact of seismic airgun noise on a marine mammal depends on the level of noise exposure. At high exposure levels, airgun noise may induce a shift in hearing threshold, whereas levels near ambient may not even be audible to marine mammals. Richardson et al. (1995, p. 325) divided the area surrounding an anthropogenic (*i.e.*, man-made) noise source into four "zones of influence", each characterized by a particular acoustic effect, as follows:

1. *The zone of hearing loss, discomfort, or injury* where high intensity noise exposure causes either temporary or permanent hearing loss (*i.e.*, TTS[1] or PTS[2]) or, at more extreme received levels, tissue damage.

2. *The zone of responsiveness* where noise exposure causes an overt change in marine mammal behaviour (*e.g.*, fleeing) or more subtle changes in breathing rate, dive patterns etc.

3. *The zone of masking* where anthropogenic noise prevent a marine mammal from hearing useful sounds, such as calls from conspecifics, echolocation signals or sounds from prey animals.

4. *The zone of audibility* where the noise is audible to a marine mammal.

In general, the noise levels that correspond to these different zones of influence depend on the species and context of the particular marine mammal under consideration (NRC, 2004, p. 26). Different kinds of marine mammals have different audiograms[3] and it has been suggested that marine mammals can be divided into groups with broadly similar hearing characteristics, *e.g.*, whales may be divided into mysticetes[4], mid-frequency odontocetes[5] and high-frequency odontocetes (Ketten, 1994). However, additional factors such as the age and sex of the individual, its behaviour at the time of exposure and whether it has been habituated or sensitized to noise also influence behavioural reactions (Wartzok et al., 2004). Thus the reader should bear in mind that threshold levels derived from observations of one species, at a particular location and time, may have limited applicability to other species or situations.

7.1.1 Zones of hearing loss, discomfort or injury

Unlike explosives, airguns do not generate a shock front and therefore it is believed that exposure to airgun noise is unlikely to inflict physical injury (*i.e.*, tissue damage) on marine

[1]TTS is short for "temporary threshold shift", a temporary loss of hearing sensitivity.

[2]PTS is short for "permanent threshold shift", a permanent loss of hearing sensitivity.

[3]An audiogram is a curve of hearing threshold versus frequency.

[4]Mysticetes are baleen whales.

[5]Odontocetes are toothed whales.

mammals (Gordon et al., 2004). However, exposure to airgun noise at very short ranges, especially beneath an array, may potentially induce either TTS or PTS in marine mammals ears (Richardson et al., 1995, p. 375).

Only very recently have experimental measurements of TTS in marine mammals, from exposure to low-frequency impulsive noise sources, been reported in the literature. The most relevant finding with regards to the effects of seismic survey noise on marine mammals was by Finneran et al. (2002), who exposed a captive beluga whale (*Delphinapterus leucas*) and a bottlenose dolphin (*Tursiops truncatus*) to single impulses from a seismic watergun and measured the resulting shift in hearing threshold. The investigators observed temporary threshold shifts of 6–7 dB in the beluga whale after exposure to single watergun shots with peak-peak pressures of 226 dB and energy flux densities of 186 dB; no threshold shift was observed in the dolphin's hearing at similar exposure levels.

Watergun pulses are similar to airgun pulses in spectral content, duration and amplitude (Parkes and Hatton, 1986, Appendix), so the findings of Finneran et al. may be reasonably extrapolated to airgun noise exposure — though, for multiple exposures, onset levels should be ajusted downward according to the equal energy hypothesis, which states that shift in hearing threshold is roughly proportional to the cumulative exposure level (Gordon et al., 2004). For example, exposure to three pulses from an airgun array may be expected to induce TTS at $\sim$ 181 dB EFD level. From Figure 6.12, one can see that EFD levels greater than 180 dB are encountered at ranges less than 200 metres from the airgun array.

The potential for TTS/PTS in marine mammals is generally assumed to be highest when noise overlaps frequencies of greatest hearing sensitivity (Hildebrand, 2004, p. 17). Measured beluga whale audiograms span over 3 decades (or 10 octaves) in frequency, from under 100 Hz to over 100 kHz, though their most sensitive hearing is above 10 kHz (Richardson et al., 1995, Fig. 8.1a). Thus the measurements of Finneran et al. may be used to estimate TTS onset levels in mid-to-high frequency specialist odontocetes; however, mysticetes, which are believed to be low frequency hearing specialists (Richardson et al., 1995, §8), may be more vulnerable than odontocetes to TTS/PTS from exposure to low-frequency airgun noise.

7.1.2 Regulatory safety ranges

Various industry regulators, such as the US National Marine Fisheries Service (NMFS), have established maximum acceptable airgun noise exposure levels ("safety ranges") for marine mammals. These threshold levels are based on estimates of marine mammal hearing damage thresholds extrapolated from known Damage Risk Criteria for humans, as discussed in Richardson et al. (1995, §10.6). For example, NMFS recommends that cetaceans (*i.e.*, whales and porpoises) not be exposed to RMS sound pressure levels in excess of 180 dB and that pinnipeds (*i.e.*, seals and sea-lions) not be exposed to RMS sound pressure levels in excess of 190 dB (US Federal Register 60:53753-60). The NMFS thresholds are cast in terms of sound pressure levels over the 90% pulse duration (see Appendix A), which are not equivalent to the EFD values given in this study. However, one can use equation A.4 to convert these thresholds to EFD levels if an appropriate value for the duration of the airgun pulse is assumed. Here, we choose a heuristic value of ~ 0.1 s for the pulse duration, T_{90}, yielding a conversion factor of ~ 10 dB between 90% RMS SPL and EFD. This value must be considered approximate — for example, the investigator C. R. Greene measured pulse durations between 0.5 s and 0.1 s, at ranges between 0.5 km and 2 km, for pulses from an airgun array operating in 400 m of water off Southern California (Greene, 1998, Fig. 5). Though shorter pulse durations (*i.e.*, greater conversion factors) are likely in the vicinity of an airgun array, this particular choice is justified because "for pulses greater than about 0.1 s ... the SPL measure is accepted as the important pulse measure to relate to influences on animal behaviour and even injury to animals" (Greene, 1998, p. 9). Thus the EFD thresholds corresponding to the NMFS guidelines are roughly 180 dB for pinnipeds and 170 dB for cetaceans.

Table 7.1 shows the mean radii (from Figure 6.12) at which the 180 dB and 170 dB EFD threshold levels are encountered for each source location. The mean radius to the 180 dB EFD isopleth varies from 76 metres at NSL06 to 185 metres at NSL02 and the mean radius to the 170 dB EFD isopleth varies from 471 metres at NSL06 to 957 metres at NSL02. Interestingly, the highest EFD levels (with the largest corresponding radii) occur at the shallowest locations, with levels diminishing as the source moves into deeper water. These results are consistent with recent measurements, made during the calibration of the R/V Maurice Ewings 20-gun research array, showing that received levels from an airgun array are greater in shallow water than in deep water (Tolstoy et al., 2004).

Table 7.1: Mean radii for 180 dB, 170 dB and 150 dB EFD level isopleths for each source location (from Figure 6.12).

	180 dB Equiv. Rad (m)		170 dB Equiv. Rad (m)		150 dB Equiv. Rad (m)	
Source Location	*Profile A*	*Profile B*	*Profile A*	*Profile B*	*Profile A*	*Profile B*
EWL01	94	99	510	540	8,587	9,633
EWL02	132	140	761	824	7,488	8,620
EWL03	171	176	757	800	5,702	6,561
NSL01	171	181	798	865	5,539	6,848
NSL02	156	185	770	957	5,588	7,923
NSL03	168	176	776	797	5,489	6,475
NSL04	127	131	616	652	7,291	8,244
NSL05	94	104	539	586	8,573	9,717
NSL06	71	76	471	487	8,596	9,469

7.1.3 Zones of responsiveness, masking and audibility

Behavioural responses of marine mammals to seismic airgun noise are highly variable, even between individuals of the same species (Richardson et al., 1995, §11.3), although most investigators have observed a general pattern of avoidance, especially among baleen whales (Gordon et al., 2004). For example, observations of migrating Grey Whales exposed to airgun noise off California (Malme et al., 1984) and in the Bering Sea (Malme et al., 1986) indicate that avoidance reactions occur with 10% probability at received levels of 163 dB RMS ($\sim$ 153 dB EFD level). According to Table 7.1 EFD levels $>$ 150 dB are encountered at ranges less than 10 km from the array. However, such precise data on avoidance response thresholds are by far the exception, rather than the norm, for most species of marine mammals. Thus, given the current state of knowledge, it is impossible to provide *a priori* estimates of reaction thresholds for most species of marine mammals for seismic airgun surveys.

Masking of communication calls from conspecifics depends primarily on the signal-to-noise (SNR) ratio within a limited bandwidth, called the *critical band*[6], surrounding the vocalizations (Richardson et al., 1995, §10.5):

$$SNR = SIL - NL \tag{7.1}$$

[6]The critical band is often assumed to be one third octave wide at low frequencies.

where, in this case, the signal level *SIL* is the level of the marine mammal call and the noise level *NL* is the level of the seismic airgun pulse. The region where $SNR < 0$ approximately corresponds to the zone where background noise will mask a communication call — though the *SNR* at which masking actually occurs depends on the hearing ability of the particular species of marine mammal in question. Baleen whales, which employ low-frequency communication calls, are believed to be most susceptible to masking from airgun noise (Gordon et al., 2004). Masking ranges for particular marine mammal species could be calculated from the results of this study, given estimates of the source level and frequency range of their vocalizations; however, such calculations are beyond the scope of this thesis dissertation.

Outside the zone of audibility, anthropogenic noise cannot be expected to affect a marine mammal (Richardson et al., 1995, §10.2). Ultimately, whether or not seismic survey noise is audible depends on the loudness of that noise relative to the ambient background noise (*i.e.*, sound due to both natural and anthropogenic sources). If the third-octave band loudness of a seismic pulse falls below the corresponding third-octave band ambient noise level then it is not likely to be audible to a marine animal (Richardson et al., 1995, p. 326). According to the passive sonar equation, which applies to any acoustic detector system, including marine mammal hearing, the signal excess at the receiver, *SE*, for an underwater signal is (Urick, 1967, p. 21):

$$SE = RL - NL - DT \tag{7.2}$$

This equation states that if the received level of a signal, *RL*, minus the noise level, *NL*, is less than the detection threshold *DT*, then it is not audible (*i.e.*, detectable). For marine mammals, behavioural experiments indicate that detection thresholds are limited to about 0 dB, especially at lower frequencies (Richardson et al., 1995, p. 327). The region where $SE > 0$ defines the zone of audibility, outside of which anthropogenic noise from the seismic survey cannot be heard.

In order to determine the extent of the zone of audibility, prior knowledge of the background ambient noise is required. Unfortunately, to date there have been no measurements of baseline ambient noise levels in the Queen Charlotte Basin. However, in lieu of actual background measurements, modelled airgun levels can be compared to typical oceanic ambient noise levels; deep water ambient noise levels, adapted from Bradley (1996), for sea-state 0 conditions and remote shipping are presented in Figure 7.1. Note that the ambient

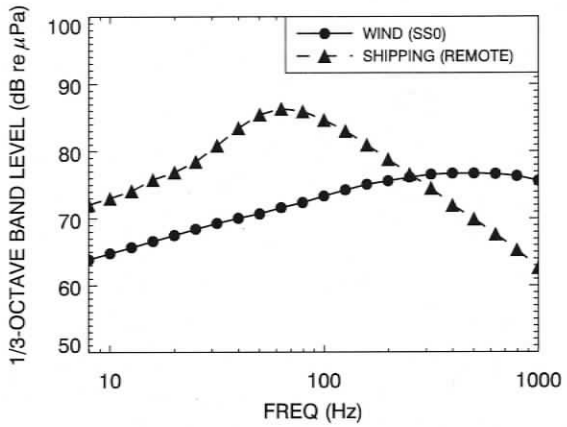

Figure 7.1: Plots of third-octave band, deep water ambient noise levels for wind (sea-state 0) and remote shipping (Bradley, 1996). Note that levels presented in this plot have been converted to third-octave band levels from spectral levels in 1 Hz bands.

noise curves presented in Figure 7.1 have been converted to third-octave band levels from spectral levels in 1 Hz bands. These ambient noise levels may be subtracted from received airgun levels, according to Equation 7.2, to obtain third-octave band levels above ambient background. Figure 7.2 shows the result of this sort of calculation for the third-octave band airgun levels presented in the previous chapter, for ranges from 100 m to 200 km along a single SE oriented modelling transect. One can see that, under these ambient noise conditions, airgun noise is 30–40 dB above the ambient background in the 315 Hz band out to 200 km range. However, the deep water ambient noise curves used in this calculation are quite conservative and may be too low for a shallow coastal region such as the Queen Charlotte Basin, where ambient noise from shipping may be more prominent than is portrayed in Figure 7.1.

7.2 Discussion: sources of uncertainty in model predictions

Though acoustic models are capable of reproducing transmission loss observed in real ocean environments, the accuracy of a propagation model is often limited by knowledge of the environmental parameters. Thus, uncertainty is introduced into acoustic propagation

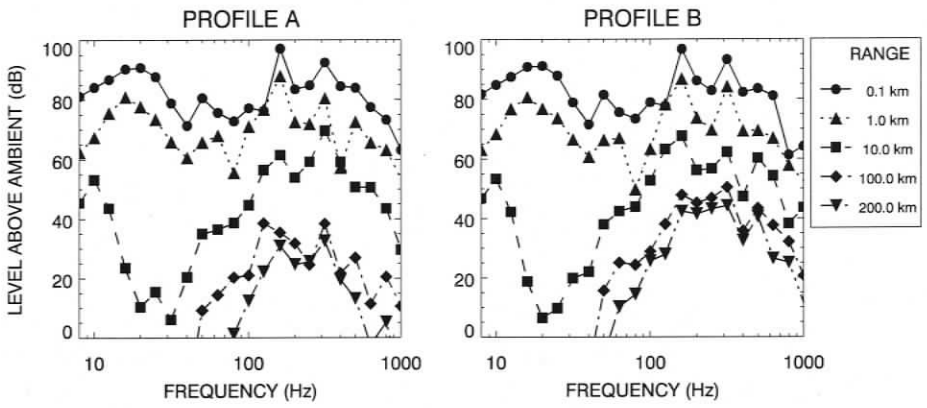

Figure 7.2: Third-octave band levels above ambient for a single airgun pulse at 25-metres depth along a SE oriented modelling transect (from Figure 6.1). Wind and shipping noise levels from Figure 7.1 have been subtracted from third-octave band airgun levels from Figure 6.2 to yield received levels above the ambient background.

modelling in two ways:

1. When the environmental parameters are variable in time — *e.g.*, the sound speed profile or sea surface roughness.

2. When the environmental parameters are poorly constrained — *e.g.*, the geoacoustic parameters.

For time-varying parameters, if the limits of the variation are known, then it is possible to estimate the influence of the variation on the received levels via sensitivity analysis. For example, in this study the variability in received level due to changes in the sound speed profile was bracketed by modelling the two limiting profile shapes, A and B. Figure 7.3 shows the difference in equivalent isopleth radius (*c.f.*, Figure 6.12) between profile A and profile B conditions, for each modelling location. It is apparent from this figure that the influence of the sound speed profile on received level, due to ducted propagation, increases considerably with distance from the source.

In shallow water, strong winds increase acoustic transmission loss because induced surface-waves scatter sound incident on the sea-surface (Weston and Ching, 1989). The effects of sea-surface roughness were not considered in the present study, as RAM does

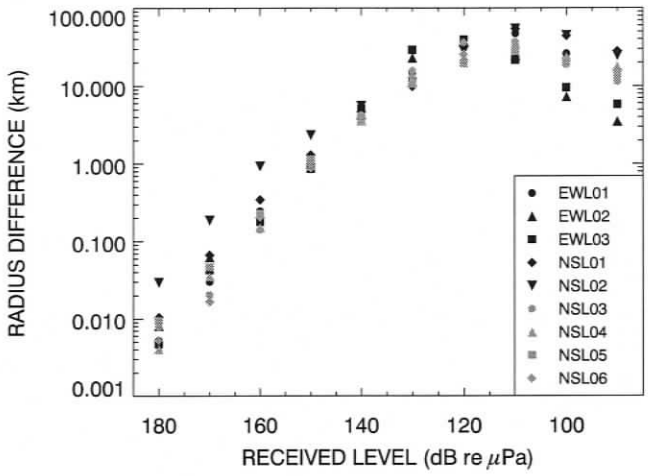

Figure 7.3: Difference in equivalent isopleth radius, between profile A and profile B conditions, for each modelling location (*c.f.*, Figure 6.12). Note that the levelling off of the differences below 120 dB is a truncation artefact caused when the received level contours intersect the boundary of the modelling area.

not currently have the ability to model this phenomenon. However, scattering at the sea-surface would have the greatest affect on ducted propagation (*i.e.*, profile B conditions) by releasing trapped acoustic energy from the surface duct. Therefore, rough seas are expected to reduce received sound levels in the presence of profile B conditions, especially at higher frequencies, though the true magnitude of this effect has not been modelled.

The environmental data of greatest uncertainty in the Queen Charlotte Basin are the geoacoustic parameters of the seabed. Though geoacoustic profiles were estimated for the current study, based on published descriptions of the bottom geology, it would be far better to have actual measurements of these data. Geoacoustic parameters may be measured directly, from sediment core data, or remotely using shallow seismic profiling or geophysical inversion techniques. In addition, the accuracy of of a geoacoustic model in predicting sound propagation may be evaluated by comparing predicted transmission loss to *in situ* measurements of acoustic propagation. By using geoacoustic data obtained from a field study in Queen Charlotte Basin, it would be possible to refine the transmission loss predictions of this study and remove a significant source of uncertainty in the model predictions.

However, no such data are known to exist at this time.

7.3 Summary and conclusions

The current thesis project was undertaken to model the generation and propagation of underwater noise from a seismic airgun survey in the Queen Charlotte Basin. The ultimate goals of this thesis project were as follows:

1. To develop a general methodology for modelling airgun survey noise in the ocean environment.

2. To apply this modelling methodology to the Queen Charlotte Basin to help address the issue of potential impacts of a seismic airgun survey on marine mammals in this region.

Noise level predictions from this study were based on an integrated modelling approach incorporating an airgun array source model, a broadband acoustic propagation model and databases describing the properties of the acoustic environment in Queen Charlotte Basin.

A numerical model was developed for the source level of a seismic airgun array, which was based based on a physical description of the oscillation and radiation of a collection of airgun bubbles. In addition to the basic bubble physics, several other important physical effects were included in model, such as heat-transfer across the bubble wall, pressure interactions between bubbles and airflow into the bubble from the airgun chamber. The physics of the airgun model were based on previous contributions by investigators such as Ziolkowski (1970), Ziolkowski et al. (1982), Dragoset (1984), Landrø (1992) and Laws et al. (1990). The final model contained four free parameters controlling the heat transfer across the bubble wall, the rate of airflow from the airgun chamber and the efficiency of the airgun chamber. Optimal values for these parameters were found by fitting the model to a collection of 38 measured airgun signatures using simulated annealing optimization. The optimized source signature model showed very good agreement between modelled and measured airgun signatures.

Transmission loss was modelled using the RAM acoustic propagation code, which is based on a wide-angle parabolic-equation approximation to the acoustic wave equation

(Collins, 1993). Broadband, 3-D transmission loss calculations over basin-scales were computed by running RAM at third-octave band centre frequencies along centrolineal radial transects — *i.e.*, using the so-called $N\times$2-D technique. The basic RAM model was modified to use the complex-density fluid approximation in the sub-bottom to simulate lossy reflections from an elastic seabed (Zhang and Tindle, 1995). The modified complex density RAM code (CRAM) was validated against benchmark analytic transmission loss curves for a Pekeris waveguide (computed using a Fast-field program) to ensure the modified model produced consistent results.

Considerable effort went into compiling bathymetric, oceanographic and geoacoustic databases for the Queen Charlotte Basin. High resolution bathymetry data for the entire Queen Charlotte Basin were obtained from the Canadian Hydrographic Service. These data were gridded onto a UTM x/y grid to facilitate extraction of range-depth profiles for input into the propagation model. Historical sound speed profile data for the Queen Charlotte Basin were analyzed using principal component analysis (PCA); the dominant mode of variability (*i.e.*, the first principal component) was found to account for nearly 90% of the variability in the data. Limiting sound speed profiles for winter and summer were generated based on the range of observed values of the first principal component. Seasonal cooling and heating in the top 100 metres of the water column were found to dominate the variability in the shape of the sound speed profile: winter profiles were characterized by a prominent surface-duct, whereas summer profiles were strongly down-refracting. A geoacoustic map for the Queen Charlotte Basin was created based on seabed classification data for this area from Barrie et al. (1990). Five different geoacoustic provinces were postulated, each with a unique bottom layering that was based on published accounts of the bottom geology by Barrie and Bornhold (1989), Bornhold and Barrie (1991) and Barrie et al. (1991). Geoacoustic profiles for the sub-bottom were estimated based on the typical geoacoustic properties of common sediment types published by Hamilton (1980).

In order to realistically model noise from seismic exploration activity in Queen Charlotte Basin, a hypothetical airgun survey scenario was created, as follows:

1. Two survey track lines were positioned over regions of the basin believed to have the greatest potential for hydrocarbon deposits.

2. The survey source was selected to be a 3000 in^3 airgun array, consisting of 32 guns

towed in four parallel subarrays.

3. Nine modelling locations were chosen along the two survey tracks.

Transmission loss grids for the entire basin were generated for each source location by executing the acoustic propagation model at 22 third-octave band frequencies along 144 radial transects for both winter and summer sound speed profiles. Environmental parameters along the modelling transects were extracted from the bathymetry and geoacoustic databases. Third-octave band source levels for the airgun array were summed together with the transmission loss grids to generate received level contour maps for the entire Queen Charlotte Basin. For each source location, received level isopleths were analyzed to determine the total ensonified area for sound level contours from 180 dB re μPa to 90 dB re μPa.

Key findings of the acoustic propagation modelling may be summarized as follows:

1. Received noise levels in the water were strongly influenced by the source location, array orientation and the shape of the sound speed profile.

2. Short range sound levels (less than $\sim$ 1 km range) were most strongly influenced by water depth; received levels were found to be greater in shallow water than in deep water. The effect of the sound speed profile was small at short range.

3. At long range, the influence of the sound speed profile on received levels increased significantly, with differences greater than 20 dB observed beyond 100 km between down-refacting (summer) and surface-duct (winter) propagation conditions.

4. At long ranges, received levels decreased most rapidly with range in those areas of the basin with shallow bathymetry (*e.g.*, Dogfish Banks) due to scattering and absorption of sound at the seabed.

5. Mean ranges to the 170 dB SEL isopleth (approximately equivalent to NMFS 180 dB 90% RMS threshold level) varied from 510 m to 957 m. The isopleth area was found to be greater in shallower water than in deeper water.

6. The azimuthal directionality of the airgun array was found to have a strong influence on received levels in the water. The highest levels from the airgun array were found to be in the broadside direction, which is typically the (horizontal) direction of maximum energy transmission from an airgun array.

In summary, this thesis has developed a flexible methodology for predicting underwater sound levels generated by a seismic airgun survey survey. The transmission loss model and airgun array source model may be applied to an arbitrary airgun survey in any location for which the appropriate environmental data are available. Thus, the methods employed in this thesis will facilitate future seismic airgun survey noise level predictions, since they are in no way limited to the source geometry and survey locations considered in this study.

Bibliography

J. Barrie and B. Bornhold. Surficial geology of Hecate Strait, British Columbia contintental shelf. *Canadian Journal of Earth Sciences*, 26:1241–1254, 1989.

J. Barrie, B. Bornhold, K. Conway, and J. Luternauer. Surficial geology of the Northwestern Canadian continental shelf. *Continental Shelf Research*, 11:701–715, 1991.

J. V. Barrie, J. L. Luternauer, K. W. Conway, and A. Caltagirone. Surficial geology of the Queen Charlotte Basin. GSC Open Files 2193, 2195, 2196, 2197, Geological Survey of Canada, 1990.

J. H. Beebe and C. W. Holland. Shallow water propagation over a complex, high-velocity bottom. *Journal of the Acoustical Society of America*, 80(1):244–250, 1986.

B. Bornhold and J. Barrie. Surficial sediments on the Western Canadian continental shelf. *Continental Shelf Research*, 11:685–699, 1991.

M. Bradley. Environmental acoustics pocket handbook. Planning Systems Inc., Slidell Louisiana, 1996.

G. H. Brooke, D. J. Thomson, and G. R. Ebbeson. A Canadian parabolic equation model for underwater sound propagation. *Journal of Computational Acoustics*, 9:69–100, 2001.

M. D. Collins. A split-step Padé solution for the parabolic equation method. *Journal of the Acoustical Society of America*, 93(4):1736–1742, 1993.

M. D. Collins. The stabilized self-starter. *Journal of the Acoustical Society of America*, 104(4):1724–1726, 1999.

M. D. Collins. *User's guide for RAM versions 1.0 and 1.0p*. Naval Research Lab, Washington, DC 20375, 1995. Available via ftp at `ram.nrl.navy.mil`.

M. D. Collins and E. K. Westwood. A higher-order energy-conserving parabolic equation for range-dependent ocean depth, sound speed and density. *Journal of the Acoustical Society of America*, 89:1068–1075, 1991.

A. B. Coppens. Simple equations for the speed of sound in Neptunian waters. *Journal of the Acoustical Society of America*, 69(3):862–863, 1981.

W. R. Crawford. Oceans of the Queen Charlotte Islands. Canadian Technical Report of Fisheries and Aquatic Sciences No. 2383, Institute of Ocean Sciences, Department of Fisheries and Oceans, 2001.

W. H. Dragoset. A comprehensive method for evaluating the design of airguns and airgun arrays. In *Proceedings – 16th annual Offshore Technology Conference*, pages 75–84, 1984.

J. J. Finneran, C. E. Schlundt, R. Dear, D. A. Carder, and S. H. Ridgway. Temporary shift in masked hearing thresholds in odontocetes after exposure to single underwater impulses from a seismic watergun. *Journal of the Acoustical Society of America*, 111 (6):2929–2940, 2002.

P. Fontana. Airgun arrays and marine mammals. Document electronically published by International Association of Geophysical Contractors, 2002. Available at `http://www.iagc.org`.

G. Frisk. *Ocean and seabed acoustics: A theory of wave propagation*. Prentice Hall, Englewood Cliffs, NJ, 1994.

B. F. Giles and R. C. Johnston. System approach to air-gun array design. *Geophysical Prospecting*, 21:77–101, 1973.

F. R. Gilmore. Collapse of a spherical bubble. Technical Report No. 26–4, Hydrodynamics Laboratory, California Institute of Technology, Pasadena, CA, 1952.

J. Gordon, D. Gillespie, J. Potter, A. Frantzis, M. P. Simmonds, R. Swift, and D. Thompson. A review of the effects of seismic surveys on marine mammals. *Marine Technology Society Journal*, 37(4):16–34, 2004.

C. R. Greene, Jr. Sound levels of an airgun array operating at platform Harmony on 17 March 1998. In *High Energy Seismic Survey Review Process and Interim Operational Guidelines for Marine Surveys Offshore Southern California*, 1998.

E. Hamilton. Geoacoustic modeling of the sea floor. *Journal of the Acoustical Society of America*, 68:1313–1340, 1980.

P. Hannigan, J. Dietrich, P. Lee, and K. Osadetz. Petroleum resource potential of sedimentary basins on the Pacific margin of Canada. GSC Bulletin 564, Geological Survey of Canda, Calgary, AB, 2001.

C. Herring. Theory of the pulsations of the gas bubble produced by an underwater explosion. OSRD Report No. 236, US National Defense Research Committee, Columbia University, 1941.

R. Hickling and M. S. Plesset. Collapse and rebound of a spherical bubble in water. *Physics of Fluids*, 7(1):7–14, 1964.

J. A. Hildebrand. Impacts of anthropogenic sound on cetaceans. Technical Report IWC/SC/E/13, International Whaling Commission, 2004.

F. B. Jensen, W. A. Kuperman, M. B. Porter, and H. Schmidt. *Computational Ocean Acoustics*. AIP Press, Woodbury, NY, 1994. ISBN 1563962098.

I. T. Jolliffe. *Principal Component Analysis*. Springer, 1986. ISBN 0387962697.

D. Ketten. Functional analysis of whale ears: adaptations for underwater hearing. *IEEE Proceedings in Underwater Acoustics*, 1:264–270, 1994.

S. Kirkpatrick, C. D. Gelatt, Jr., and M. P. Vecchi. Optimization by simulated annealing. *Science*, 220:671–680, 1983.

M. Landrø. Modelling of GI gun signatures. *Geophysical Prospecting*, 40:721–747, 1992.

M. Laws, L. Hatton, and M. Haartsen. Computer modelling of clustered airguns. *First Break*, 8(9):331–338, 1990.

X. Lurton. *An introduction to underwater acoustics: principles and applications.* Springer, Chichester, U.K., 2002.

C. Malme, P. Miles, P. Tyack, C. Clark, and J. Bird. Investigations of the potential effects of underwater noise from petroleum industry activities on migrating gray whale behavior/Phase II: January 1984 migration. BBN Report No. 5586, 1984.

C. Malme, B. Wursig, J. Bird, and P. Tyack. Behavioural responses of gray whales to industrial noise: feeding observations and predictive modelling. BBN Report No. 6265, 1986.

National Research Council (NRC). *Ocean noise and marine mammals*. National Academies Press, Washington, D.C., 2003a. ISBN 0-309-08536-5.

National Research Council (NRC). *Marine mammals populations and ocean noise: determining when noise causes biologically significant effects*. National Academies Press, Washington, D.C., 2004b. ISBN 0-309-09449-6.

G. Parkes and L. Hatton. *The marine seismic source*. D. Reidel Publishing Company, 1986. ISBN 90-277-2228-5.

M. B. Porter, F. B. Jensen, and C. M. Ferla. The problem of energy conservation in one-way models. *Journal of the Acoustical Society of America*, 89:1058–1067, 1991.

W. H. Press, S. A. Teukolsky, B. P. Flannery, and W. T. Vetterling. *Numerical Recipes: FORTRAN*. Cambridge University Press, New York, NY, USA, 1990. ISBN 0521383307.

R. G. Racca and J. A. Scrimger. Underwater acoustic source characterization of air and water guns. Technical Report No. 06SB 97708-5-7055, Defense Research Establishment Pacific, 1986.

W. J. Richardson, C. R. Greene, Jr., C. I. Malme, and D. H. Thomson. *Marine Mammals and Noise*. Academic Press, San Diego, CA, 1995. ISBN 0-12-588441-9.

Royal Society of Canada (RSC). The Royal Society of Canada report of the expert panel on science issues related to oil and gas activities, offshore British Columbia. RSC EPR 04-1, 2004.

J. P. Snyder. *Map projections — a working manual*. U.S. Government Printing Office, Washington, D.C., 1984. ISBN 9998605067.

W. H. Thorp. Analytic description of the low-frequency attenuation coefficient. *Journal of the Acoustical Society of America*, 42:270, 1967.

M. Tolstoy, J. Diebold, S. Webb, D. Bohnenstiehl, E. Chapp, R. Holmes, and M. Rawson. Broadband calibration of R/V ewing seismic sources. *Geophysical Research Letters*, 31: L14310, 2004.

R. J. Urick. *Principles of Underwater Sound for Engineers*. McGraw-Hill, New York, 1967.

D. Wartzok, A. Popper, J. Gordon, and J. Merrill. Factors affecting the responses of marine mammals to acoustic disturbance. *Marine Technology Society Journal*, 37(4):6–15, 2004.

D. E. Weston and P. A. Ching. Wind effects in shallow-water acoustic transmission. *Journal of the Acoustical Society of America*, 86(4):1530–1545, 1989.

M. J. Whiticar, T. Schuemann, M. Niemann, K. Rohr, and M. Johns. Analysis of petroleum potential in Queen Charlotte Basin phase 1 report: Broad-scale basin characterization. Technical report, Biogeochemistry Facility, School of Earth and Ocean Sciences, University of Victoria, 2003.

Y. Zhang and C. Tindle. Improved equivalent fluid approximations for a low shear speed ocean bottom. *Journal of the Acoustical Society of America*, 98(6):3391–3396, 1995.

A. Ziolkowski. A method for calculating the output pressure waveform from an air gun. *Geophysical Journal of the Royal Astronomical Society*, 21:137–161, 1970.

A. Ziolkowski, G. Parkes, L. Hatton, and T. Haugland. The signature of an air gun array: Computation from near-field measurements including interactions. *Geophysics*, 47: 1413–1421, 1982.

Appendix A

Sound level metrics

Sound pressure underwater is measured in decibels relative to a fixed reference pressure of 1 μPa. With regards to the impact of anthropogenic noise on marine mammals, however, there are several different sound level metrics that are commonly used for measuring broadband noise underwater. It is important to note that measuring impulsive noise (*e.g.*, from airgun arrays) is different than measuring continuous noise (*e.g.*, from shipping): impulsive sources emit short bursts of acoustic energy interspersed by periods of silence, whereas continuous sources emit nearly constant noise levels that vary slowly with time. These differences require that continous noise and impulsive noise be quantified using different sound level metrics. The three most common metrics for impulsive sounds are peak pressure level, RMS level and energy flux density (also called sound exposure level). It is very important to be aware which metric has been quoted when comparing measurements from different studies, since the difference between the various metrics may be as large as 20 dB.

The peak sound pressure level is the maximum instantaneous sound pressure level attained by a signal, $p(t)$ [ANSI S1.1 1984 3.52, 4.13]:

$$L_{\mathrm{pk}} = 20\log_{10}\left(\max|p(t)|\right) \tag{A.1}$$

This metric is very commonly quoted for impulsive sounds but does not take into account the pulse duration or bandwidth of a signal. Furthermore the broadband modelling techniques required to model peak pressure, such as Fourier synthesis, are far too computation-

ally intensive to be applied to a basin-scale study.

The sound pressure level or SPL is the decibel level of the mean square pressure over some fixed time window, T [ANSI S1.1 1984 3.53, 4.08]:

$$L_p = 10\log_{10}\left(\frac{1}{T}\int_T p^2(t)dt\right) \tag{A.2}$$

This metric is often used in noise exposure studies, for both continuous and impulsive noise. However, a subtle point involved in applying this metric to impulsive sounds is the selection of a standard averaging window over which to compute the mean square pressure. Thus, when quoting sound pressure level, it is very important to be aware of the length of integration time window that has been used. For the current study, sound pressure levels have been computed using an equivalent one-second averaging time window.

In studies of impulsive noise, the sound pressure level is often computed over the pulse duration, rather than over a fixed time window. In this case, the SPL is usually defined so that the time window, T_{90}, is taken to be the interval containing 90% of the pulse energy — commonly referred to at the 90% RMS SPL (L_{p90}). The calculation of the 90% RMS level from an airgun pressure trace is illustrated in Figure A.1. Unfortunately, this metric is only suitable for *in situ* measurement, since the variable time window implicit in the definition of the 90% RMS SPL is nearly impossible to model accurately.

The energy flux density (EFD) is the time-integral of the square pressure over a fixed time window; this is numerically equal to the sound exposure level (SEL) from a single impulse and so we use the same formula [ANSI S1.1 1984 3.54, 4.21]:

$$L_E = 10\log_{10}\left(\int_T p^2(t)dt\right) \tag{A.3}$$

For impulsive events, the time window is usually taken to be 1 second in length from the onset of the pulse. The calculation of EFD from an airgun pressure trace is also illustrated in Figure A.1. This metric has units of $\mu\text{Pa}^2 \cdot s$ rather than μPa and is not actually a measure of sound pressure but of sound energy[1]. Nonetheless, this metric is closely related to the sound pressure level since the two are computed in a very similar fashion. In fact, EFD

[1] Strictly speaking, the integral of squared sound pressure is only equal to the energy flux density for plane waves.

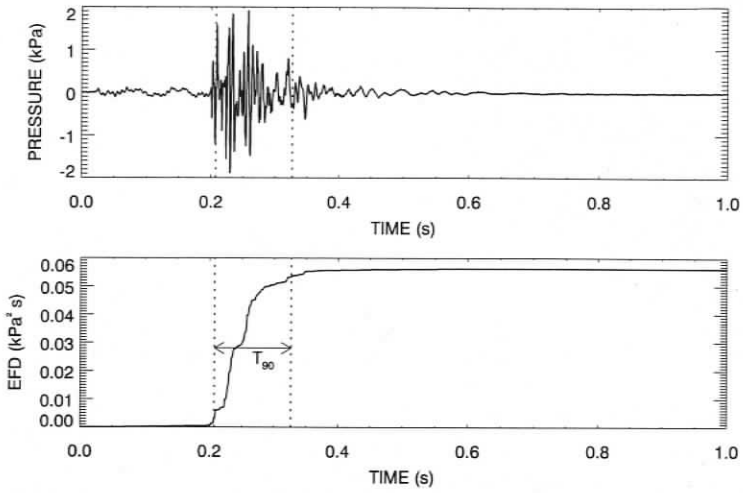

Figure A.1: Time series plot illustrating the calculation of RMS level and energy flux density (EFD) from an airgun pressure trace. The top plot is sound pressure versus time for a single airgun pulse, measured at approximately 1 km range. The bottom plot is the time integral of squared pressure, which is equal to the EFD. The dashed lines bracket the 90% energy time window (T_{90}) for this particular airgun pulse.

and SPL are equivalent if the integration time window, T, for both metrics is chosen to be 1 second. In addition, energy flux density may be modelled quite accurately, under most conditions, using standard acoustic models.

It is well known that the 90% RMS level metric for impulsive noise suffers from problems due to variations in the averaging interval caused by pulse spreading and that the 90% RMS metric itself has no special biological significance with regards to the hearing of marine mammals or fish[2]. Thus peak and energy level metrics are increasingly being used by the acoustics community in favor of the 90% RMS level for reporting impulsive noise. However, one difficulty with using energy level metrics is that much of the existing literature regarding the impact of anthropogenic noise on marine mammals and fish gives measured sound levels in terms of the 90% RMS SPL. Fortunately, if the pulse duration, T_{90}, is known (or may be estimated) then the EFD may be computed from the 90% RMS

[2]P. T. Madsen. Marine mammals and noise: Problems with root mean square sound pressure levels for transients. J. Acoust. Soc. Am. 117:3952–3956, 2005.

level via a simple relation:

$$L_E = L_{p90} + 10\log_{10} T_{90} + 0.458 \tag{A.4}$$

where the last term accounts for the fact that only 90% of the acoustic pulse energy is delivered over the standard integration period.